# Thermal Interface Materials (TIM) for Applications in Microelectronics

by

Shahla Ali Akbari

A thesis
presented to the University of Waterloo
in fulfillment of the
thesis requirement for the degree of
Doctor of Philosophy
in
Chemistry

Waterloo, Ontario, Canada, 2012

© Shahla Ali Akbari 2012

## AUTHOR'S DECLARATION

I hereby declare that I am the sole author of this thesis. This is a true copy of the thesis, including any required final revisions, as accepted by my examiners.

I understand that my thesis may be made electronically available to the public.

## Abstract

A major challenge in the formulation of thermal interface materials (TIM), used in the microelectronics industry to facilitate heat transfer from an electronic package to a heat sink, is to ensure that the material is electrically insulating while achieving a high thermal conductivity. Several parameters influence thermal conductivity, but it will be shown that proper selection of the polymers serving as binders and additives in the formulation is important. The incorporation of electrically insulated metallic particles as fillers can also help to increase the thermal conductivity of a TIM. This Dissertation is concerned with exploring different strategies for the preparation of thermally conducting, but electrically insulating TIM compositions. Among these, the synthesis and the application of functionalized (telechelic) poly(ethylene oxide), PEO, in the preparation of TIM will be explored in more details. To achieve this goal, we conducted the synthesis of telechelic oligomers containing a primary amine functional group at one end, and investigated their influence on the properties of metallic surfaces such as copper. The results obtained indicate that the PEO-$NH_2$ oligomers can bind to copper metal and/or the oxide layer at its surface, leading to much lowered electrical conductivity for the particles.

The composition of TIM formulations was optimized in a systematic fashion using these materials and effective thermal conductivities reaching up to 9.4 W/mK were attained, much higher than for two commercial TIM used as benchmarks (1.5 W/mK for Arctic Silver 5, and 3.5 W/mK for ShinEtsu X23-7783D). Moreover, thinner layers (down to 0.004 mm) were achieved for the materials developed as compared to commercial TIM (0.07 mm). Additionally, we used a computational approach based on the method of random resistor networks to predict the effective thermal conductivity of the TIM. We studied the effects of mono- and polydispersed filler

particle size distributions, as well as geometry (spherical particles and flakes). The influence of the PEO-$NH_2$ oligomers acting as surfactants on the effective thermal conductivity was also investigated by defining surfactant concentration-dependent thermal conductivities. We finally compared the results of the numerical simulations with our experimental data and obtained excellent agreement for most compositions.

## Acknowledgements

I would like to express my sincere gratitude to my advisors, Professor Mario Gauthier and Professor Matt Scott, for their guidance and support throughout my graduate school years. I would also like to extend my gratitude to my Supervisory Committee Members, Professors Richard Culham, Jean Duhamel, and Tong Leung for their interest, advice, and helpful suggestions. I would likewise like to thank Professor Mehran Kardar (Department of Physics, Massachusetts Institute of Technology), Professor Muhammad Sahimi (Department of Chemical Engineering and Materials Science, University of Southern California), and Professor Siv Sivaloganathan (Department of Applied Mathematics, University of Waterloo) for their help, and their very useful suggestions and discussions.

I would like to thank all my co-workers in the Gauthier and Duhamel groups for their support and useful discussions through the years but particularly Dr. Jason Dockendorff, Dr. Gabriel Ngole Njikang, and Dr. Firmin Moingeon. I would especially like to thank Professor Richard Culham, Dr. Peter Teertstra, and the other members of the Microelectronics Heat Transfer Laboratory (MHTL), University of Waterloo for their help and assistance to learn and work with the instruments in their Lab. I would also like to thank Colin Phipps, Gibin Powathil, and Hadi Zarkoob, from the Department of Applied Mathematics (University of Waterloo) for their help and discussions on the modeling and computational part of the project.

I would like to acknowledge the Ontario Centre for Microelectronics Assembly and Packaging (CMAP) and the University of Waterloo for their financial support.

## Dedication

I dedicate this work to my family.

# Table of Contents

AUTHOR'S DECLARATION ..... ii

Abstract ..... iii

Acknowledgements ..... v

Dedication ..... vi

Table of Contents ..... vii

List of Figures ..... xi

List of Tables ..... xvii

List of Abbreviations and Symbols ..... xix

**Chapter 1 Thesis Overview ..... 1**

1.1 Thesis Outline ..... 2

**Chapter 2 Background Material ..... 4**

2.1 Living Anionic Polymerization ..... 5

2.1.1 Mechanism ..... 6
2.1.2 Initiation ..... 6
2.1.3 Propagation ..... 6
2.1.4 Termination ..... 7

2.2 Techniques for Oligomer Characterization ..... 8

2.2.1 Size Exclusion Chromatography (SEC) ..... 8
2.2.2 Nuclear Magnetic Resonance (NMR) Spectroscopy ..... 8
2.2.3 Infrared (IR) Spectroscopy ..... 9

2.3 X-ray Photoelectron Spectroscopy (XPS) ..... 9

2.4 Contact Angle Measurements ..... 11

2.5 Thermal Interface Materials ..... 11

2.5.1 Different Types of TIM ..... 13
2.5.2 Steady-State Measurement Method ..... 14
2.5.3 Heat Transfer Phenomena ..... 15

2.6 Characterization of Filler Particles ..... 19

2.6.1 Scanning Electron Microscopy ........ 19
2.6.2 Coulter Counter Multisizer II ........ 20
2.6.3 Thermal Interface Material Preparation ........ 21

2.7 Mathematical Modeling ........ 21

2.7.1 Previous Models ........ 23

**Chapter 3 Synthesis of α-Amino Oligo(ethylene oxide) and Binding on Copper Surfaces.. 28**

3.1 Overview ........ 29

3.2 Introduction ........ 29

3.3 Experimental Procedures ........ 31

3.3.1 Ethylene Oxide Purification ........ 31
3.3.2 Purification of 2-Ethanolamine ........ 32
3.3.3 Diphenylmethylpotassium ........ 32
3.3.4 Polymerization of Ethylene Oxide (EO) ........ 33
3.3.5 Alternate Method for MPEG-$NH_2$ Synthesis ........ 35
3.3.6 Polymer Characterization ........ 35
3.3.7 X-ray Photoelectron Spectroscopy (XPS) ........ 37
3.3.8 Contact Angle (CA) Measurements ........ 38
3.3.9 Resistivity Measurements ........ 38

3.4 Results and Discussion ........ 40

3.4.1 Synthesis ........ 40
3.4.2 XPS Analysis ........ 42
3.4.3 Contact angle (CA) measurements ........ 48
3.4.4 Insulation Resistance Measurements ........ 50

3.5 Conclusions ........ 51

**Chapter 4 Improved Thermal Interface Materials (TIM) for Applications in Microelectronics ........ 53**

4.1 Overview ........ 54

4.2 Introduction ........ 54

4.3 Background and Method ........ 57

4.3.1 Thermal Resistance Measurement Method ........ 57

4.4 Experimental Procedure for TIM Preparations ........ 60

4.4.1 Metallic Fillers Analysis ........ 60

4.4.2 Electrically Insulating Methods ..... 64
4.4.3 Polymeric Matrix ..... 67

4.5 Experimental Procedures for Measuring the Effective Thermal Conductivity ..... 68

4.6 Results and Discussion ..... 70

4.6.1 Commercial TIM ..... 71
4.6.2 Particle Encapsulation with Silanes and PEO-$NH_2$ ..... 72
4.6.3 Mixtures of Particles Versus Single Components ..... 75

4.7 Conclusions ..... 86

4.8 Appendix: Bulk Thermal Conductivity versus Load ..... 88

**Chapter 5 Mathematical Modeling of Thermal Interface Materials (TIM) ..... 90**

5.1 Overview ..... 91

5.2 Introduction ..... 91

5.3 Random Resistor Network Method ..... 92

5.4 Numerical Algorithm ..... 95

5.4.1 Generation of the Random Resistor Network ..... 95
5.4.2 Generating Simultaneous Equations (Calculating Effective Thermal Conductivity) 99
5.4.3 Effect of Boundaries ..... 100

5.5 Validation of the Matlab Code ..... 101

5.5.1 One-dimensional Simulations ..... 105
5.5.2 Three-dimensional Simulations ..... 107

5.6 Polydispersity and Geometry of Fillers ..... 109

5.6.1 Monodispersed Al Particles ..... 109
5.6.2 Polydispersed Al Particles ..... 110
5.6.3 Copper Flake Filler ..... 110
5.6.4 Mixture of Al Particles and Cu Flakes ..... 112

5.7 Simulation vs. Experimental Results ..... 113

5.7.1 Effective Thermal Conductivity of Fillers ..... 113
5.7.2 The Effect of Surfactant ..... 116

5.8 Conclusion ..... 124

5.9 Appendix: Simulation Time and Uncertainlies ........ 126

**Chapter 6 Concluding Remarks ........ 129**

6.1 Summary and Contributions to Knowledge ........ 130

6.2 Suggestions for Future Work ........ 132

**Appendix Matlab Codes ........ 134**

A.1 Network Description ........ 135

A.2 Functions ........ 136

A.3 Main Matlab Code ........ 136

A.4 Functions for Finding Neighbors ........ 145

**References ........ 149**

Chapter 2 ........ 149

Chapter 3 ........ 152

Chapter 4 ........ 153

Chapter 5 ........ 154

Appendix ........ 155

## List of Figures

Figure 2.1 Anionic synthesis of amino-PEO.[2] .................... 7

Figure 2.2 Schematic representation of contact angle measurement. .................... 11

Figure 2.3 Application of a heat sink and uneven surface mating. .................... 12

Figure 2.4 Microscopic view of two surfaces: (A) without TIM, $Qc$ is heat flow through contact area and $Qg$ is heat flow through air gap, (B) without TIM, and (C) with an ideal TIM. .................... 13

Figure 2.5 Apparatus to measure the resistance of TIM, adapted from Reference (24). .................... 15

Figure 2.6 Schematic representation of a real TIM as a simple thermal resistance circuit. .................... 17

Figure 2.7 Schematic representation of the thermal resistance versus TIM thickness. .................... 18

Figure 2.8 Schematic representation of a Coulter Counter. .................... 20

Figure 2.9 Two phases ordered parallel (A) and perpendicularly (B) to the direction of heat flow (red: matrix, blue: metal). .................... 26

Figure 3.1 Setup for EO purification on a vacuum line (A: purified monomer storage ampoule, B: round-bottomed flask, C: monomer ampoule). Adapted from Reference (11). . 32

Figure 3.2 Polymerization manifold (A: thick wall reaction ampoule, B: purified monomer ampoule). Adapted from Reference (11). .................... 34

Figure 3.3 Schematic view of the testing cell designed for the insulation resistance measurements, (A) with two electrodes and (B) view of the cell from the top....... 39

Figure 3.4 $^{1}$H NMR spectrum for PEO5-$NH_2$ in deuterated chloroform. .................... 41

Figure 3.5 XPS survey spectra for copper substrates treated with PEO-$NH_2$ (A, bottom, violet) and MPEG (B, top, red) samples. .................... 44

Figure 3.6 XPS spectra for Cu2p peak of PEO-$NH_2$ (A) and MPEG (B) on copper substrate for different sputtering times (red = 0 s, dark blue = 20 s, green = 40 s, dark red = 80 s, light blue = 2 m, blue-green = 5 m, and purple = 10 m ). ...................................... 45

Figure 3.7 XPS spectra for the O1s peaks of PEO-$NH_2$ (A) and MPEG (B) on copper for different sputtering times (same scale used for both samples)................................ 46

Figure 3.8 XPS spectra for C1s peaks of PEO-$NH_2$ (A) and MPEG (B) on copper for different sputtering times. .......................................................................................... 47

Figure 3.9 XPS spectra for the N1s peak for copper substrate treated with MPEG (black line) and PEO-$NH_2$ for different sputtering times. ................................................................ 48

Figure 4.1 Pictures of the system used.......................................................................... 57

Figure 4.2 Schematic representation of the system used. ............................................ 58

Figure 4.3 Photograph of the flux meter with the pins used for the thickness measurements using a laser micrometer. ........................................................................................ 59

Figure 4.4 (Left) A photograph of the flux meter with a shim. (Right) Schematic representation of the flux meter spacing with a shim. ................................................................... 59

Figure 4.5 Size distributions of aluminum powders determined by sieving................................ 61

Figure 4.6 Coulter counter result for the smallest Al powder fraction of the testing sieves. ....... 62

Figure 4.7 SEM pictures of metallic fillers (scale 10 μm)........................................................... 63

Figure 4.8 SEM pictures for aluminum powders......................................................................... 63

Figure 4.9 Schematic representation of the insulation of copper flakes with silane coupling agents.............................................................................................................................. 66

Figure 4.10 Plots of thermal joint resistance (left) and effective thermal conductivity (right) as a function of thickness for commercial TIM compositions. ...................................... 72

Figure 4.11 Thermal joint resistance versus TIM thickness for the samples in Table 4.6 (100 PSI load)........ 75

Figure 4.12 Thermal joint resistance of TIM formulations measured without shims: blue for 4(86) + $D_3$(5.6) + $E_1$(8.4), pink for 5(86) + $D_3$(5.6) + $E_1$(8.4), green for 6(86) + $D_3$(5.6) + $E_1$(8.4), and red for 7(86) + $D_3$(5.6) + $E_1$(8.4). ........ 76

Figure 4.13 Thermal joint resistance versus TIM thickness, pink for 4(85) + A(15), blue for 2(80) + A(20), and green for 2(44) + 4(44) + A(12). ........ 78

Figure 4.14 Thermal joint resistance of TIM compositions: blue for 4(86) + A(14), pink for 4(86) + E2(14), green for 4(86) + E1(14). ........ 80

Figure 4.15 Thermal joint resistance versus TIM thickness, pink for 2(43) + 4(43) + $D_3$(5.6) + $E_2$(8.4), blue for 2(43) + 4(43) + $D_3$(5.6) + $E_1$(8.4). ........ 81

Figure 4.16 Thermal joint resistance versus TIM thickness, pink for 4(82) + $D_3$(7.2) + $E_2$(10.8), blue for 4(84) + $D_3$(6.4) + $E_2$(9.6), and green for 4(86) + $D_3$(5.6) + $E_2$(8.4). ........ 83

Figure 4.17 Thermal joint resistance variation with TIM layer thickness: Purple for Shin Etsu X23-7783D, pink for Arctic Silver5, blue for 4(82) + $E_1$(18), and green for 4(84) + $E_1$(16). ........ 85

Figure 4.18 The effective thermal conductivity of TIM vs. surfactant percentage for different applied loads 5-100 PSI........ 89

Figure 5.1 The center of the matrix or filler is replaced by a node (site) in the lattice. The electrical resistance between neighbouring nodes is represented by a resistor........ 93

Figure 5.2 Possible adjacent nodes in the lattice: (A) particle-particle, (B) matrix-matrix, and (C) particle-matrix (red: matrix, blue: metal). ........ 95

Figure 5.3 A sample structure for a random resistor network. (A) Monodispersed Al particles (volume fraction $\varphi_{Al} = 0.2$), lattice size $N_1 = N_2 = N_3 = 20$, $h_{\mathrm{TIM}} = 150$ μm and $r \approx 8$ μm (red: polymeric matrix, blue: Al particles). (B) As in panel A, but the polymeric matrix was removed for clarity. ........................................................ 96

Figure 5.4 A sample structure for a random resistor network: (A) Polydispersed Al particles (input $\varphi_{Al} = 0.08$ and output $\varphi_{Al} = 0.21$), $N_1 = N_2 = N_3 = 20$ (red: matrix, blue: Al particles). The large particles occupy $3 \times 3 \times 3$ lattice sites, while smaller particles are $1 \times 1 \times 1$. (B) As in panel A, but with the background matrix removed for clarity. ........................................................................................... 97

Figure 5.5 A sample structure for a random resistor network: (A) Copper flakes (input $\varphi_{Cu} = 0.05$ and output $\varphi_{Cu} = 0.21$), $N_1 = N_2 = N_3 = 20$ (red: matrix, green: copper flakes). (B) As in panel A, but with the background matrix removed for clarity. .. 98

Figure 5.6 A sample structure for a random resistor network: (A) Copper flakes (input $\varphi_{Cu} = 0.024$ and output $\varphi_{Cu} = 0.081$), and monodispersed Al particles ($\varphi Al = 0.116$), $N_1 = N_2 = N_3 = 20$ (red: matrix, blue: Al particles, and green: copper flakes). (B) As in panel A, but with the background matrix removed for clarity...................... 99

Figure 5.7 One dimensional representation of the network (red: matrix, blue: metallic fillers). 101

Figure 5.8 Possible cases for the random network $1 \times 1 \times N_3$, if top and bottom layers are fixed to be particles (red: matrix, blue: metal). .......................................................... 102

Figure 5.9 Possible cases for the random network$1 \times 1 \times 4$, if the top and bottom layers are fixed to be particles (red: matrix, blue: metal). .................................................. 103

Figure 5.10 Results of one-dimensional simulations for the effective thermal conductivity ($k_{\mathrm{eff}}$) as a function of the filler volume fraction ($\varphi$)................................................... 106

Figure 5.11 Results of one-dimensional simulations for the effective thermal conductivity ($k_{\mathrm{eff}}$) as a function of the lattice size $N_3$ (filler volume fraction $\varphi = 0.5$).................... 107

Figure 5.12 Three-dimensional simulation results for the effective thermal conductivity as a function of $N_1 = N_2$, for the filler volume fraction (A) $\varphi = 0.1$ and (B) $\varphi = 0.5$. ........................................................................................................................ 108

Figure 5.13 Effective thermal conductivity as a function of particle volume fraction $\varphi$ for monodispersed Al particles and polymeric matrix for red line (diamonds), blue line (squares) for lower bound and green line (triangles) for upper bound (the network size $20 \times 20 \times 20$ using 500 realizations)......................................................... 109

Figure 5.14 Effective thermal conductivity as a function of the filler volume fraction $\varphi$, for mono- and polydispersed Al particles and a polymeric matrix (red diamonds and blue triangles data points, respectively) for a network of $20 \times 20 \times 20$ using 500 realizations. ......................................................................................................... 111

Figure 5.15 Effective thermal conductivity as a function of the filler volume fraction $\varphi$ for copper flakes (purple squares), and Al particles (red diamonds for mono- and blue triangles for polydispersed particles) with polymeric matrix, for a network size of $20 \times 20 \times 20$ using 500 realizations. ................................................................. 111

Figure 5.16 Thermal conductivity as a function of the filler volume fraction $\varphi$ for copper flakes mixed with monodispersed (red, bottom) and polydispersed (blue, top) Al particles with a polymeric matrix, a network size of $20 \times 20 \times 20$ with 500 realizations. 112

Figure 5.17 (A) Experimental (blue triangles) and numerical (red diamonds) results for the effective thermal conductivity of composites containing polydispersed Al particles (sizes $1 \times 1 \times 1$ and $3 \times 3 \times 3$) and a polymeric matrix as a function of the filler

volume fraction $\varphi$. (B) Schematic view of the porous oxide layer of Al particles and the air gaps. ........................................................................................ 115

Figure 5.18 (A) Experimental (blue triangles) and numerical (red diamonds) results for the effective thermal conductivity of Cu flakes and polymeric matrix as a function of the volume fraction of Cu flakes, $\varphi$. (B) Schematic view of the copper oxide layer and the air gaps. ........................................................................................ 116

Figure 5.19 Experimental (filled diamond) and numerical (unfilled diamond) results for the effective thermal conductivity of composites (polydispersed Al particles, polymeric binder, and surfactant) vs. surfactant content. (A), (B), and (C) are for filler volume fractions of 48%, 52%, and 55%, respectively. .................................................. 118

Figure 5.20 Experimental (filled diamonds) and numerical (unfilled diamonds) results for the thermal conductivity of samples containing Cu flakes, polymeric matrix, and surfactant vs. surfactant content. (A), (B), and (C) are for filler volume fractions of 35%, 39%, and 45%, respectively. ........................................................................ 119

Figure 5.21 Estimated values of surfactant concentration-dependent effective thermal conductivity for polydispersed Al particles (triangle) and Cu flakes (diamond). . 120

Figure 5.22 Results of the effective thermal conductivity for composites containing polydispersed Al particles (sizes $1 \times 1 \times 1$ and $3 \times 3 \times 3$), Cu flakes, a polymeric matrix, and surfactant vs. surfactant content for experiments (filled diamonds) and predicted numerical simulations (unfilled diamonds) using estimated surfactant concentration-dependent effective thermal conductivity of fillers....................... 122

## List of Tables

Table 2.1 Mathematically equivalent transport problems.[39] ........ 22

Table 2.2 Models to predict the thermal conductivity of TIM with filler particles.[13] ........ 25

Table 3.1 Samples for insulation resistance measurements. ........ 40

Table 3.2 Molecular weight characterization of PEG-$NH_2$ oligomers by $^1$H NMR and SEC analysis. ........ 42

Table 3.3 Contact angle of liquids on different surfaces. ........ 49

Table 3.4 Surface energy components and $\Delta G_{SL}^{IF}$ (mJ/m$^2$) for copper. ........ 50

Table 3.5 The resistivity results for different samples. ........ 51

Table 4.1 Characteristics of the metallic particles used in the TIM formulations. ........ 60

Table 4.2 Testing sieves series for particles size analysis. ........ 61

Table 4.3 Characteristics of matrix materials used in TIM formulations. The letters A, $B_i$, $C_i$, $D_i$, $E_i$, F, and $G_i$ identify the matrix type used. ........ 67

Table 4.4 Electrical characteristics of mixtures on non-conducting Al particles with conducting Cu flakes. ........ 70

Table 4.5 Characteristics of TIM compositions for silane encapsulation of filler particles. ........ 73

Table 4.6 Characteristics of TIM compositions with PEO-$NH_2$ encapsulation of the filler particles (100 PSI load). ........ 74

Table 4.7 Characteristics of TIM compositions for different sizes of Cu flakes. ........ 77

Table 4.8 The effective thermal conductivity of TIM containing copper flakes with different oligomeric binders. ........ 78

Table 4.9 The effective thermal conductivity of TIM containing copper flakes with different liquid binders. ........ 82

Table 4.10 The effective thermal conductivity of TIM containing Cu flakes, TriEGDME, and PEO15-$NH_2$ for thin layers. ........ 83

Table 4.11 The effective thermal conductivity of TIM containing MPEG-$NH_2$. ........ 84

Table 4.12 The effective thermal conductivity of TIM for thin layers. ........ 86

Table 4.13 The effective thermal conductivity of TIM for different applied loads. ........ 88

Table 5.1 Estimated value of surfactant concentration-dependent effective thermal conductivity of Al particles and Cu flakes. ........ 120

Table 5.2: Simulation times for new versions of code. ........ 126

Table 5.3: Simulated effective thermal conductivities for different $N$. ........ 127

Table 5.4: Simulation uncertainties for $N_1 = N_2 = N_3 = 20$. ........ 128

## List of Abbreviations and Symbols

| | |
|---|---|
| $A$ | Area ($m^2$) |
| Al | Aluminum |
| b. p. | Boiling Point |
| BHT | 2,6-Di-*tert*-butyl-4-methylphenol |
| BLT | Bond-line Thickness |
| CA | Contact Angle |
| $CDCl_3$ | Deuterated Chloroform |
| Cu | Copper |
| $d$ | Particle Diameter (m) |
| $d_{50}$ | Median Value of Particle Diameter |
| DPMK | Diphenylmethylpotassium |
| EO | Ethylene Oxide |
| $g$ | Electrical Conductivity |
| GPC | Gel Permeation Chromatography |
| $h$ | TIM Thickness (m) |
| HCl | Hydrochloric Acid |
| HV | High Vacuum |
| $I$ | Electrical Current (ampere) |
| IR | Infrared |
| $k$ | Thermal Conductivity (W/mK) |
| $K_2CO_3$ | Potassium Carbonate |
| $k_{\mathrm{eff}}$ | Effective Thermal Conductivity (W/mK) |

| | |
|---|---|
| $k_{\mathrm{eff}}^{\mathrm{Al}}$ | Estimated Surfactant-Concentration Dependent Effective Thermal Conductivity of Al Particles (W/mK) |
| $k_{\mathrm{eff}}^{\mathrm{Cu}}$ | Estimated Surfactant-Concentration Dependent Effective Thermal Conductivity of Cu Flakes (W/mK) |
| $k_{\mathrm{eff}}^{\mathrm{Matrix}}$ | Estimated Surfactant-Concentration Dependent Effective Thermal Conductivity of Polymeric Matrix (W/mK) |
| $k_e^{(S)}$ | Effective Thermal Conductivity for Realization S (W/mK) |
| $k_m$ | Thermal Conductivity of Liquid (W/mK) |
| $k_p$ | Thermal Conductivity of Particle (W/mK) |
| LW | Lifshitz-van der Waals Interactions |
| $M_w$ | Weight-average Molecular Weight (g/mol) |
| $M_n$ | Number-average Molecular Weight (g/mol) |
| MPEG | Methoxy Poly(ethylene glycol) |
| MWD | Molecular Weight Distribution |
| $NH_4OH$ | Ammonium Hydroxide |
| NMR | Nuclear Magnetic Resonance |
| PDI | Polydispersity Index |
| PDMS | Polydimethylsiloxane |
| PEO | Poly(ethylene oxide) |
| PEO-$NH_2$ | $\alpha$-Amino Poly(ethylene oxide) |
| PhMgCl | Phenyliumagnesium Chloride |
| $Q$ | Heat Flow Rate (W) |
| $q$ | Heat Flux (W/m$^2$) |

| | |
|---|---|
| $R$ | Thermal Resistance (K/W) |
| $r$ | Lattice Space |
| $R_b$ | Boundary Thermal Resistance ($K/Wm^2$) |
| $R_c$ | Thermal Contact Resistance (K/W) |
| $R_j$ | Thermal Joint Resistance (K/W) |
| RBF | Round-bottomed Flask |
| RRN | Random Resistor Network |
| RTD | Resistive Temperature Device |
| SEC | Size Exclusion Chromatography |
| SEM | Scanning Electron Microscopy |
| $T$ | Temperature (K) |
| THF | Tetrahydrofuran |
| TIM | Thermal Interface Material |
| TriEGDME | Triethylene Oxide Dimethyl Ether |
| $V$ | Electric Voltage (volt) |
| XPS | X-ray Photoelectron Spectroscopy |
| $\alpha$ | Dimensionless Parameter $\equiv 2R_b k_m/\mathrm{d}$ |
| $\gamma^-$ | Lewis Base (Electron Donor) Component of Surface Energy |
| $\gamma^+$ | Lewis Acid (Electron Acceptor) Component of Surface Energy |
| $\gamma^{AB}$ | Polar Component of Surface Energy (Acid-Base Interactions) |
| $\gamma_S^-$ | Lewis Base Component of Surface Energy of Solid |
| $\gamma_S^+$ | Lewis Acid Component of Surface Energy of Solid |
| $\gamma_S^{LW}$ | Apolar Component of Surface Energy |

| | |
|---|---|
| $\theta$ | Contact Angle |
| $\rho$ | Resistivity (Ωm) |
| $\sigma$ | Thermal Conductance (W/K) |
| $\sigma_m$ | Thermal Matrix- Matrix Conductance (W/K) |
| $\sigma_p$ | Thermal Particle-Particle Conductance (W/K) |
| $\sigma_{pm}$ | Thermal Particle- Matrix Conductance (W/K) |
| $\varphi$ | Particle Volume Fraction |
| $\Delta G_{SL}^{IF}$ | Free Energy of Interfacial Interaction (mJ/m$^2$) |

# Chapter 1

## Thesis Overview

## 1.1 Thesis Outline

This Thesis focuses on the synthesis and the characterization of tailored poly(ethylene oxide) (PEO) oligomers bearing a primary amine group (PEO-$NH_2$) at one end, their application as components in thermal interface materials (TIM) to improve the thermal conductivity, as well as the mathematical modeling of these systems. Chapter two provides an overview of living anionic polymerization and the physical characterization of polymers, as well as the literature on TIM composites leading to the use of PEO telechelic oligomers. In the last portion of Chapter 2, the mathematical models reported in the literature for thermal conductivity will be briefly reviewed, before concluding with a discussion of the model selected for this study.

Chapter three focuses on the synthesis of PEO-$NH_2$ using 2-ethanolamine as an anionic polymerization initiator, after deprotonation with diphenylmethylpotassium (DPMK). The characterization of the functionalized oligomers by different methods is then discussed, in addition to their ability to bind on copper surfaces.

Chapter four is an investigation of the use of PEO-$NH_2$ as a surfactant in TIM formulations, and reporting their thermal conductivity compares with commercial materials. Other strategies for the preparation of non-conducting TIM formulations are also considered.

Chapter five focuses on mathematical modeling of the TIM composites using the random resistor network method. The role of the surfactants in increasing the thermal conductivity of TIM composites is also considered in this chapter.

Chapter six summarizes the conclusions drawn from this research and some recommendations for future work.

In agreement with the University of Waterloo Thesis Guidelines, Chapters 3-5 are written in the format of individual papers to be submitted for publication in scientific journals. Thus each chapter includes an abstract, an introduction on relevant background material, a description of the experimental procedures used, the presentation and discussion of the results obtained, concluding remarks, and a list of references.

# Chapter 2

## Background Material

## 2.1 Living Anionic Polymerization

Living anionic polymerization has been studied for a long time, starting with Szwarc in 1956.[1] For about 46 years, living anionic polymerization has been the leading technique for the synthesis of polymers with controlled molecular weights and narrow molecular weight distributions (MWD). Anionic polymerization is also the most reliable method for the synthesis of polymers with tailored chain end functionality.[2] It is a powerful technique to synthesize homopolymers and block copolymers, in which the active sites allow propagation with insignificant depropagation, and ideally no termination or transfer reactions. The polydispersity index (PDI) of a polymer is defined in Equation (2.1), where $M_w$ is the weight-average molecular weight and $M_n$ is the number-average molecular weight, and it remains low (typically less than 1.1-1.2) for living systems.

$$\mathrm{PDI} = \frac{M_w}{M_n} \qquad (2.1)$$

In this section we provide a brief overview of the mechanism of living anionic polymerization (in particular oligomerization) leading to functionalized ($-NH_2$) chain ends, and of some techniques used to characterize the resulting oligomers. The discussion continues with the application of these functionalized oligomers in thermal interface materials (TIM) and the apparatus used to measure thermal conductivity. This is followed by a discussion of mathematical models employed to describe and predict the thermal conductivity of TIM.

A living anionic polymerization reaction is a chain polymerization in which the living center remains active even after all of the monomer has been consumed, so that if more monomer were added, the chain would continue to grow and increase in molecular weight.[1-3]

### 2.1.1 Mechanism

Chain polymerization occurs in three steps: initiation, propagation, and termination. In the initiation step, an activated species, such as a strong nucleophile acting as the initiator, attacks the monomer (e.g. ethylene oxide, EO, or a vinyl monomer) and opens the ring or the double bond, producing a new activated species. In the propagating step, this activated species adds further monomer units, regenerating an active propagating center each time. Termination is induced as the last step by reaction of the activated site with a proton source, for example through the addition of a solution of HCl.

### 2.1.2 Initiation

In anionic polymerization, the initiator is usually a strong nucleophile such as an organometallic compound or an alcoholate. The nucleophile initiates the chain reaction by breaking one of the bonds in the monomer. For instance, the EO monomer can be polymerized by anionic ring-opening polymerization using an alkoxide initiator. The reaction starts with a nucleophilic attack to open the ring and form the propagating species. To synthesize heterobifunctional PEO with the structure X-PEO-Y, where X and Y are different functional groups such as $–NH_2$ and –OH, the initiation can be carried out with a suitable initiator such as an amino alcohol. The initiation reaction is shown as the first step in Figure 2.1.

### 2.1.3 Propagation

In this step further monomer units are added to the reactive propagating center, as shown in the second reaction of Figure 2.1, through successive nucleophile attacks to open EO rings. This addition occurs again and again until all the monomer present in the reaction is consumed ($n$ represents the number of monomers added to the chains, and is defined as the degree of polymerization).

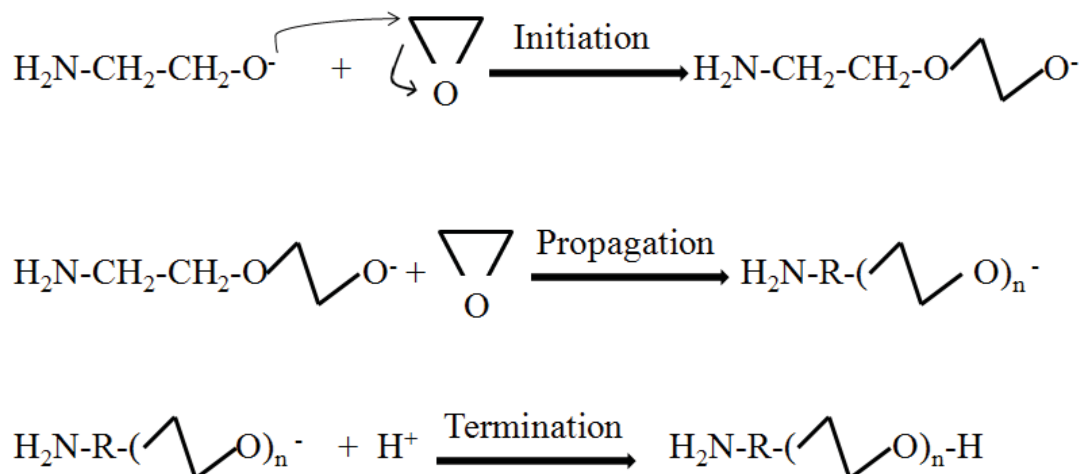


**Figure 2.1 Anionic synthesis of amino-PEO.**[2]

### 2.1.4 Termination

In this step the reactive propagating center is deactivated, which ends chain growth. Termination can occur due to proton transfer from impurities or other species present in the polymerization reaction, such as the solvent or the monomer, or can be intentionally induced by adding a proton source such as water or hydrochloric acid (the third reaction in Figure 2.1). When the polymerization is completed and terminated, the polymer can be recovered and purified.

The functionalized PEO-$NH_2$ oligomer may then be characterized by different techniques to determine its molecular weight, and to confirm the presence of the desired functional group(s) in the chains. The ability of the primary amine functional group of the PEO-$NH_2$ oligomers to bind copper was also studied by different methods. The following section introduces some of the methods and instruments used in the characterization of the PEO-$NH_2$ oligomers. The results of these measurements are reported in Chapter 3.

## 2.2 Techniques for Oligomer Characterization

### 2.2.1 Size Exclusion Chromatography (SEC)

Size exclusion chromatography (SEC),[4] also called gel permeation chromatography (GPC), uses porous particles in a column to separate polymer molecules of different sizes, and ultimately determine their MWD. The apparatus used for that purpose usually consists of a chromatographic column (which can vary in length and diameter) packed with the separation material, having pore sizes corresponding to the range of molecular weights of interest for the polymer in solution. A pump is connected to the column to maintain a constant flow of an eluting solvent, and a suitable detector is connected after the column to monitor the relative concentration of the separated components.

The molecules which are smaller than the size of the pores in the packing can diffuse in and out of them, and therefore take a longer time to exit the column than larger molecules that cannot penetrate into as many pores. This means that the largest molecules exit the column first and the smallest molecules last, and thus molecules are sorted by size. Before starting the measurements, one must ensure that the SEC instrument is calibrated with suitable standards of known molecular weights in the range of interest.

### 2.2.2 Nuclear Magnetic Resonance (NMR) Spectroscopy

One of the most widely used methods to determine the chemical structure of organic compounds nowadays is nuclear magnetic resonance (NMR) spectroscopy, and in particular proton NMR ($^{1}$H NMR) spectroscopy.[5] This technique involves exposing a compound in solution to a magnetic field and measuring the absorption of radio waves by the hydrogen atom nuclei (protons). Each nucleus in a different chemical environment absorbs radio waves of different

energies. The NMR spectrum thus gives information about the nature of the chemical environment of each magnetically active nucleus in the molecule.[6]

The composition and the number-average molecular weight of the PEO-$NH_2$ oligomers were determined by $^1H$ NMR spectroscopy analysis. The details of the methods used will be discussed in Chapter 3.

### 2.2.3 Infrared (IR) Spectroscopy

Infrared spectroscopy[5] can be used to confirm the presence of functional groups such as $-NH_2$ in a polymer. Infrared spectroscopy analysis is based on the absorption of light in the IR region of the electromagnetic spectrum, covering a range from about 400 to 4000 $cm^{-1}$. In IR spectroscopy, the radiation is partly absorbed as it passes through a sample when its energy corresponds to different vibration modes for bonds or fragments of the molecules. The recorded spectrum can be expressed either in terms of the absorbance (A) of the sample, or the percent transmittance of the sample as a function of wavelength.

IR measurements were used to characterize the PEO-$NH_2$ oligomers synthesized, to confirm the presence of the desired amino groups.

## 2.3 X-ray Photoelectron Spectroscopy (XPS)

The X-ray photoelectron spectroscopy (XPS) technique,[7] also known as electron spectroscopy for chemical analysis (ESCA), is used to identify the chemical composition of the surface and near-surface regions of materials. This technique provides useful information on the chemical state of the elements (atomic composition of a sample or oxidation level of a certain element) present at the surface of a sample. XPS uses an X-ray beam to cause photo-ionization. The

energy dispersion of the reflected beam can be analyzed to study the chemical composition of the surface using the Einstein equation[8]

$$BE = h\upsilon - KE - F_{spec} \tag{2.2}$$

where KE is the kinetic energy of the photoelectron, $h\upsilon$ is the energy of the X-ray photons, BE is the binding energy of the photoelectrons, and $F_{spec}$ is the work function of the spectrometer. The XPS instrument counts the electrons ejected from the sample surface when it is irradiated with X-rays. The XPS spectra are quantified in terms of peak intensities and binding energies (BE). The peak intensity characterizes the concentration of a compound at the surface, while the BE indicates its chemical state. The study of the surface composition of a material is not always sufficient, and it may also become necessary to know the chemical composition of the inner layers of the material. A complementary technique to XPS analysis, depth profiling, allows reaching these layers by using an ion gun to etch the sample surface over a period of time, to profile the concentration of the species making up the material as a function of etching depth. Each ion gun etching cycle exposes a new surface, and the XPS spectra provide the means to analyze the composition of that surface.

The XPS instrument consists of an X-ray source, a sample holder in a high-vacuum chamber, an energy analyzer (for the detection of photoelectrons), a monochromator (to select the X-ray energy), and an electron detector (a photomultiplier tube or a multichannel detector).

The XPS technique was used in this project to characterize the bonding interactions between the primary amine functional group of the PEO-$NH_2$ oligomers and the metal or metal oxide components of copper surfaces.

## 2.4 Contact Angle Measurements

The optical contact angle (or sessile drop) method can be used to estimate the wetting of a substrate (e.g. a copper plate) by a liquid. The contact angle (CA) is defined as the angle between the baseline of the drop and the tangent to the drop boundary, corresponding to point P in Figure 2.2. When a hydrophilic liquid is placed on a metal surface, the surface tension of the liquid leads to the formation of a spherical droplet. The CA measurements provide information on the bonding energy of the substrate and the surface tension of the droplet, which can be related to the wetting, adhesion, and adsorption properties. The CA apparatus has a sample stage to hold the substrate, calibrated micropipettes to apply a liquid, a light source to illuminate the droplet, a camera used to take pictures at short time intervals, and image processing software to calculate the angle for the tangent to the droplet.[9]

The next section provides a discussion of thermal interface materials (TIM) and the method (apparatus) used to measure their thermal conductivity.

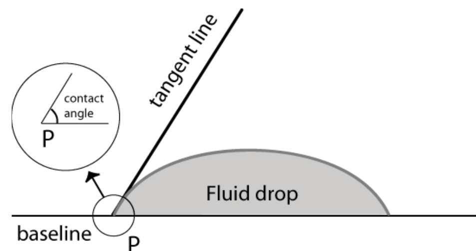


**Figure 2.2 Schematic representation of contact angle measurement.**

## 2.5 Thermal Interface Materials

The influence of the electronic packaging in limiting heat dissipation is important in electronic components due to increased power levels in many operating devices, which are also

associated with an increase in device temperature. As the size of electronic components shrinks, controlling their operating temperature becomes more challenging. Effective heat transfer from an electronic device (for example an integrated circuit, IC) to a heat sink is thus very important to lower its operating temperature.[10] When solid surfaces such as an IC package and a heat sink are brought into contact, there is a temperature difference between the two components. This is due to the thermal contact resistance ($R_c$), originating from surface roughness and uneven mating, which limits the effective contact area between the two surfaces to a very small fraction of the overall area (typically less than 3%). The air gap and the constriction resistance at the points of solid contacts therefore causes the thermal joint resistance,[11] as shown in Figure 2.3 and Figure 2.4.

Thermal interface materials (TIM) are widely used in the electronics industry, and especially in microelectronic devices, to reduce the thermal resistance and facilitate heat transfer to the heat sink, by filling the air gap between the two surfaces and increasing their overall heat transfer capability. For that reason, improving the performance of TIM has been the focus of much attention. A wide range of materials such as adhesives, greases, and metal particle-filled pastes have been investigated recently.[12]

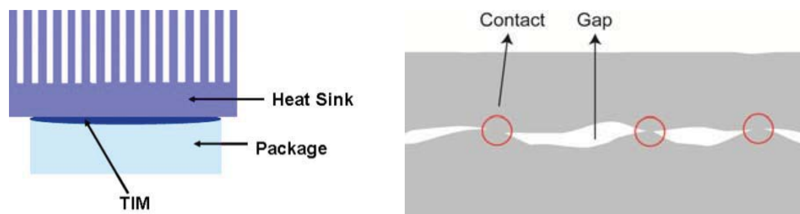


**Figure 2.3 Application of a heat sink and uneven surface mating.**

In our project, TIM were prepared from metallic particle fillers such as aluminum (Al) and copper (Cu), triethylene glycol dimethyl ether (TriEGDME) as an oligomeric binder, and the synthesized PEO-$NH_2$ oligomers as surfactants. It will be shown that the surfactant increases the performance of the TIM by increasing its thermal conductivity and spreadability. The thermal conductivity of these materials was measured using the steady-state test method ASTM D5470 described in Section 2.5.2.

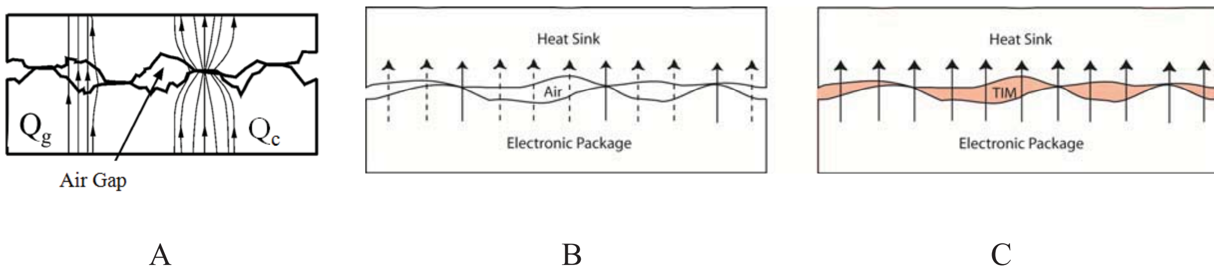


**Figure 2.4 Microscopic view of two surfaces: (A) without TIM, $Q_c$ is heat flow through contact area and $Q_g$ is heat flow through air gap, (B) without TIM, and (C) with an ideal TIM.**

### 2.5.1 Different Types of TIM

In polymeric composite TIM, metallic particles can serve as fillers to promote heat transfer due to their high intrinsic thermal conductivity, typically k=200-400 W/mK. Over the past decades, different polymer families have been examined to improve heat transfer.[13] One of the first experiments on the thermal conductance of metal-polymer joints was done by Fletcher and Miller in the 1970s.[14,15] Different types of elastomers with and without metallic or oxide fillers were investigated, indicating decreases in joint resistance with these fillers. Fletcher *et al.*[16] also studied the effect of additives in TIM formulation using polyethylene. Later, Ochterbeck *et al.*[17]

investigated the decrease in thermal joint resistance using polyamide films combined with paraffin, diamond, and metallic foils. They concluded that the hardness of the fillers was the most important parameter determining the efficiency of the interface materials. The thermal conductivity of most of these materials was found to be independent of the testing temperature used (10-100 $^{o}$C). Parihar and Wright[18] conducted an experimental investigation on the contact resistance of stainless steel and silicone rubber. Since the thermal conductivity of the rubber was largely temperature-dependent, the contact joint resistance was also a function of temperature in this case. Many polymers such as polyethylene, polypropylene, poly(vinyl chloride), Teflon, Delrin, and Nylon were also tested by Marmira *el al.*[19] Marotta *el al.*[20] reported that some commercial elastomeric gaskets and graphite-based materials displayed less dependence of the thermal contact resistance on contact pressure. Recently, Kim *et al.*[21] studied the thermal joint conductance of low density polyethylene and polyester. There has been a wide range of investigations on TIM and the improvement of heat transfer, and further details on this topic can be found in reviews by Yovanovich[22] and Prasher.[13]

### 2.5.2 Steady-State Measurement Method

An ASTM test method for thermal conductivity measurements was developed starting in 1984, to be published in 1993 as the D5470 standard (thermal transmission properties of thin, thermally conductive solid electrical insulation materials).[23] The apparatus used for the test consists of four basic units including a test column, loading, cooling, and measurement systems. Schematic and pictorial representations of the testing apparatus used are provided in Figure 2.5 A and B, respectively.

The test column consists of heating and cooling blocks, lower and upper heat flux meters, and a loading cell. The pressure is applied to minimize the interface resistance present between

the TIM and the heat flux meters. Moreover, five ceramic resistive temperature devices (RTD) are installed in each flux meter with 10 mm separation from each other. A linear actuator provides an axial force and a stable contact load for the test column. A water-glycol cooling system with controlled temperature cools the upper copper plate, thereby acting as a heat sink.

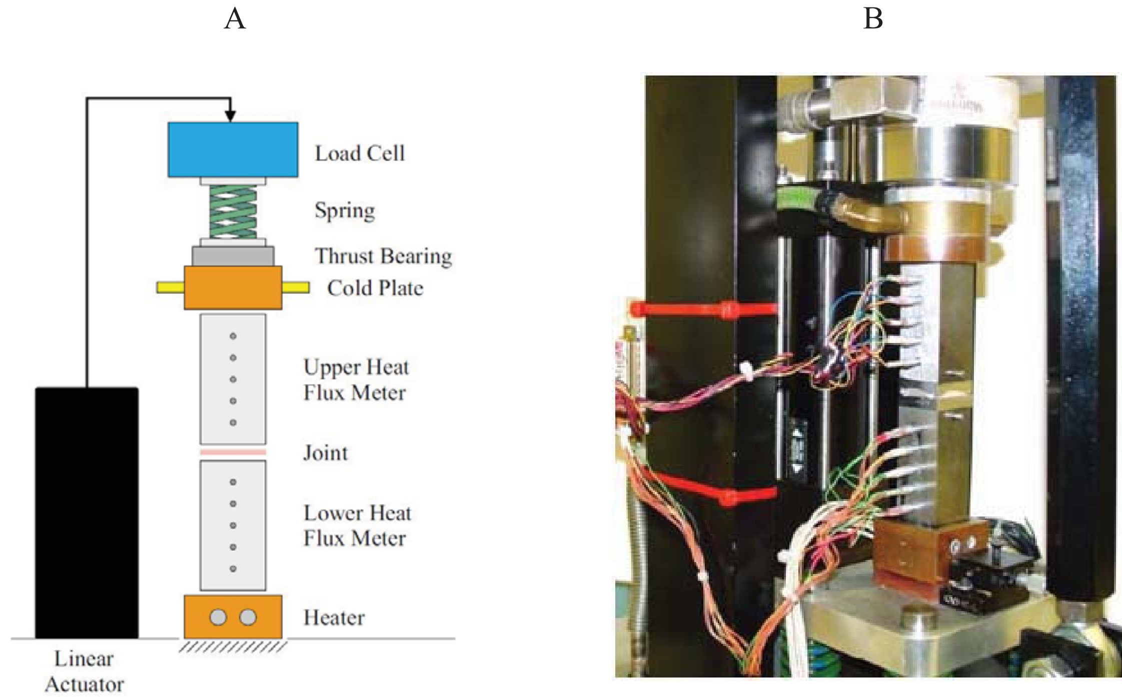


**Figure 2.5 Apparatus to measure the resistance of TIM, adapted from Reference (24).**

### 2.5.3 Heat Transfer Phenomena

To measure the thermal joint resistance using the testing apparatus, ideal heat conduction (perfect contact between the flux meters and the TIM) is assumed between the upper and lower heat flux meters which are separated by a TIM layer of uniform thickness. The thermal joint resistance ($R_j$) is determined from the heat flow rate $Q$ and a measured temperature difference ($\Delta T$) across the TIM layer.

$$R_j = \frac{\Delta T}{Q} \tag{2.3}$$

The heat flow rate is usually proportional to the applied pressure, the area $A$ ($m^2$) normal to the heat flow, and the temperature drop $\Delta T$ (K) across the TIM layer. Since it is difficult to measure the temperature at the surface of the TIM, the temperature drop across the sample is determined by extrapolation from the least squares fit of the temperatures measured at regular intervals by the RTDs to the contacting surfaces of the flux meters. The thermal conductivity of the TIM, $k$ (W/mK), is then calculated according to Fourier's equation $Q = kA(\Delta T/h)$, or

$$k = \frac{Q}{A}\frac{h}{\Delta T} = \frac{h}{AR_j} \tag{2.4}$$

where $Q/A$ is the heat flux (W/$m^2$), $h$ is the TIM thickness (m), $A = 6.25 \times 10^{-4}\ m^2$, and $\Delta T$ (K) is the temperature drop across the TIM layer. The TIM thickness can be determined accurately by several methods, for example using shims to achieve predefined thicknesses. Another possibility to measure the thickness during the test is to determine the distance between two pins installed on the top and bottom heat flux meters as the TIM is compressed (as the load is applied), using a laser micrometer.[25]

The thermal conductivity of the TIM quantifies its ability to conduct heat, and the thermal resistance is a measure of how easily heat is transferred across the interface between the two solid surfaces (representing the electronic package and the heat sink). Using the ASTM D5470 test method, the thermal conductivity and the thermal resistance are measured directly. This method can also be used to estimate the contact resistance between the TIM and a metal surface as a function of pressure.[26] In practice the TIM does not completely fill all the air gaps (see Figure 2.6), and some voids persist at the interface, which increases the thermal joint resistance (although the figure exaggerates the real situation).

To determine the thermal joint resistance, the system is considered as a thermal resistance circuit where the resistance is $R = (T_1 - T_2)/Q)$, where $T_1$ and $T_2$ are the temperatures of the electronic package and the heat sink, respectively and $Q$ is the heat flow rate.

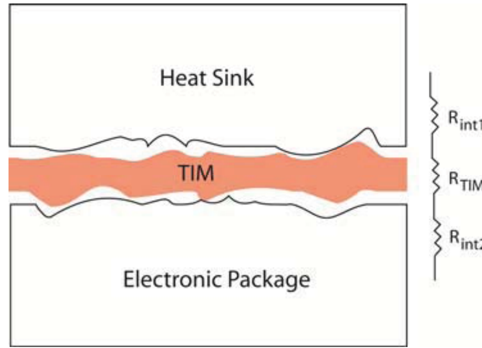


**Figure 2.6 Schematic representation of a real TIM as a simple thermal resistance circuit.**

It is generally assumed that the interface resistance is a combination of three resistances, $R_{\mathrm{j}} = R_{\mathrm{int1}} + R_{\mathrm{TIM}} + R_{\mathrm{int2}}$, where $R_{\mathrm{int1}}$ is the resistance between electronic package and the TIM (interface 1), $R_{TIM} = h/Ak$ is the resistance across the TIM layer, and $R_{\mathrm{int2}}$ is the resistance between the TIM and the heat sink (interface 2). The interface resistance of each region, consisting of contact and gap resistances, is given by

$$R_{\mathrm{int1,2}} = \left(\frac{1}{R_{\mathrm{contact1,2}}} + \frac{1}{R_{\mathrm{gap1,2}}}\right)^{-1} \tag{2.5}$$

In a plot of $R_{\mathrm{j}}$ as a function of TIM thickness ($h$), the extrapolation to zero thickness gives the value of the contact resistance $R_{\mathrm{c}} = R_{\mathrm{int1}} + R_{\mathrm{int2}}$. In this case the thermal joint resistance can be written as Equation (2.6), where the bulk thermal resistance refers to the thermal resistance of the TIM.

$$R = R_{bulk} + R_c = \frac{h}{Ak} + R_c \quad (2.6)$$

Since the test method ASTM D5470 is normally carried out under ideal surface flatness and parallelism conditions to measure thermal conductivity (making the test as reproducible as possible), the contact resistance can be considered to be very small and ignored. However it is known that any changes in roughness and flatness of the heat flux meter surfaces will affect the measured thermal resistance.[27] The contact resistance can be minimized by applying a higher pressure (as long as it is tolerated by the TIM) and decreasing the roughness of the surfaces by lapping them to less than 0.4 μm.[26] The surface roughness can be measured with a contact profilometer, whereby a diamond stylus on the instrument is moved across the surface to measure the vertical displacement of the stylus as a function of position.[28]

A plot of the thermal resistance $R$ versus thickness $h$ should yield a straight line with a slope proportional to the reciprocal of the thermal conductivity (Figure 2.7), and an intercept at zero thickness corresponding to the contact resistance.

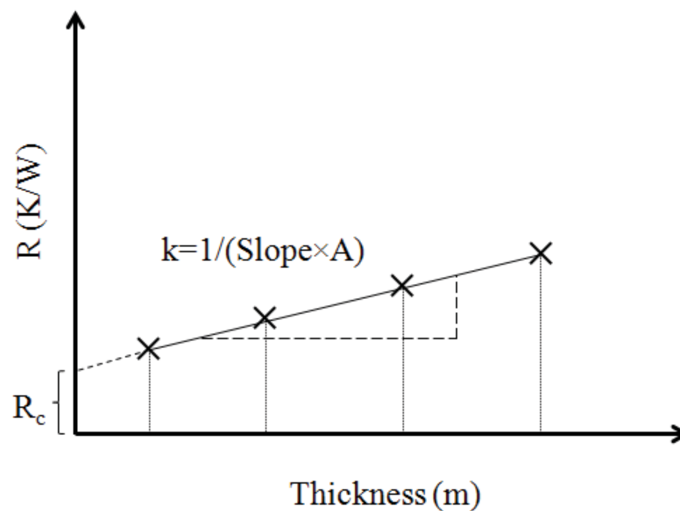


**Figure 2.7 Schematic representation of the thermal resistance versus TIM thickness.**

The reciprocal of the slope multiplied by the area $A$ corresponds to the thermal conductivity of the TIM ($k = (\text{Slope} \times A)^{-1}$). This calculation method was selected for the experiments described in Chapter 4.

## 2.6 Characterization of Filler Particles

Two types of metallic fillers (aluminum particles, Al, and copper flakes, Cu) were used in most of the TIM formulations tested. The size and shape of the fillers were investigated by scanning electron microscopy (SEM). A series of testing sieves was used to determine the size distribution of the Al particles, in combination with a Coulter Counter Multisizer II instrument for the particles passing through the smallest sieve. The following sections give a general introduction to the operation of these instruments used to characterize the filler particles. The results obtained will be discussed in Chapter 4.

### 2.6.1 Scanning Electron Microscopy

The scanning electron microscope (SEM) uses electrons instead of light to form two-dimensional images of objects.[29] The main advantage of SEM over optical microscopy is its large field depth, which allows different portions of large samples to stay in focus while maintaining a high resolution. This means that closely spaced features can be examined at high magnifications (from typically 15 to 200,000 times in about 25 steps, depending on the SEM model used). The instrument uses electromagnets rather than lenses to focus the electron beam, which gives much more control over the degree of magnification. The insulating sample must be coated with a thin layer of a metal, such as gold, by sputter coating under vacuum, to prevent charging of the sample due to the accumulation of electric charges during the imaging process.

Since the shape and size of the filler particles can play an important role in the thermal conductivity of a TIM,[30] the SEM was used to characterize the fillers in terms of porosity, shape, and size distribution. The results and images obtained by SEM analysis will be discussed in Chapter 4.

### 2.6.2 Coulter Counter Multisizer II

A Coulter Counter determines the size distribution of particles suspended in a conducting liquid.[31] It relies on the fact that particles moving in an electric field cause measurable disturbances in that field, and the magnitude of the disturbances is proportional to the size of the particles.

As shown in Figure 2.8, the Coulter Counter is set up with an orifice (or an aperture tube) of defined size placed in a conducting electrolyte liquid such that the sensing zone is completely submerged and the tube can fill with the liquid.

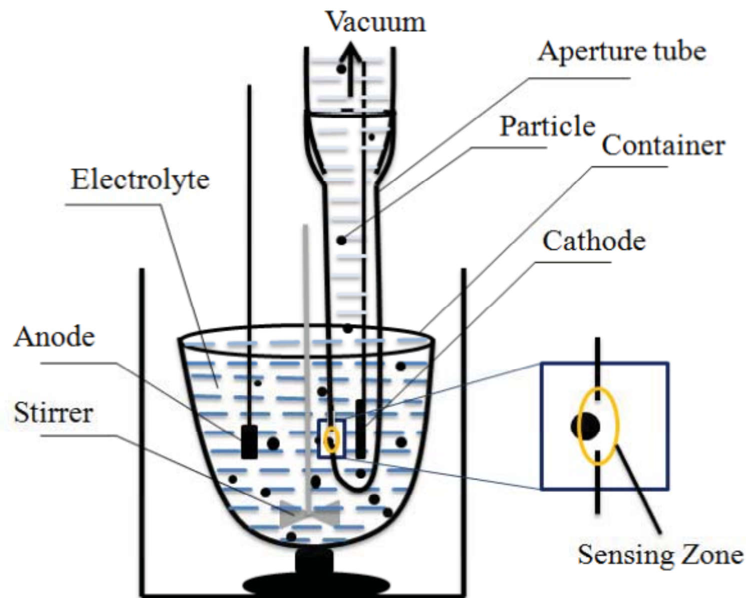


**Figure 2.8 Schematic representation of a Coulter Counter.**

Electrodes are positioned both inside and outside the aperture tube, which allows a current to flow through the aperture. A pump is used to create a vacuum at the top of the tube, which sucks the particles into the orifice situated between the two electrodes. Each particle passing through the opening changes its electrical impedance and produces a pulse that can be directly converted to the volume of the particle. The resulting data are collected by recording the electrical pulses generated as the particles traverse the aperture.

### 2.6.3 Thermal Interface Material Preparation

As mentioned above, the size distribution of filler particles is an important factor determining the performance of a TIM. After solid particles analysis, TIM were prepared by mixing the solid fillers (Al particles and/or Cu flakes), an oligomeric matrix (TriEGDME), and PEO-$NH_2$ as surfactant, at different volume fractions of the solid components. The thermal conductivity of these samples was measured using the technique mentioned earlier in Section 2.5.1. The results of these tests will be reported in Chapter 4.

## 2.7 Mathematical Modeling

Mathematical modeling was utilized to explain and predict the thermal conductivity of TIM formulations with different components. This section is a brief review of some of the modeling techniques available in the literature, and the model selected for our purpose.

Different models have been developed to represent the macroscopic properties of heterogeneous materials such as the thermal conductivity.[32-38] To define effective macroscopic properties in general, *local* transport equations must be considered at the microscopic level. If the microscopic length scale is much smaller than the macroscopic dimensions of the sample, then the effective (or average) properties of the material become independent of the sample size. For

instance, suppose that a material consists of two different components with distinct thermal (or alternately electrical) conductivities $k_1$ and $k_2$. The governing (steady-state) equations at a point $x$ are given for both phases by

$$q = -k\nabla T \quad (\text{Fourier's law}) \tag{2.7}$$
$$\nabla . q = 0$$

where $q$, $T$, and $k$ are the *local* heat flux (W/m$^2$), the temperature (K), and the thermal conductivity (W/mK) at a specific point $x$, respectively. Taking an ensemble average, i.e. the average over a number of samples that are macroscopically identical (having the same thickness and constant $\nabla T$) but microscopically different (having different thicknesses and $\nabla T$ varying locally), we define $< q >= -k_e < \nabla T >$, where $k_e$ is the effective thermal conductivity. Note that this effective conductivity exists in the limit where the ratio of the microscopic to macroscopic length scales approaches zero.[39] Equation (2.7) is the basic governing equation for a wide range of problems in physics and engineering for equivalent transport phenomena including heat and electrical conduction, and diffusion processes (see Table 2.1).

**Table 2.1 Mathematically equivalent transport problems.[39]**

| **Phenomenon** | **Potential** | **Driving force** | **Flux** | **Transport coefficient** |
|---|---|---|---|---|
| Heat conduction | Temperature | Temperature gradient | Heat flux | $k$ |
| Electrical conduction | Electrical potential | Electric field | Current density | $g$ |
| Diffusion | Density | Density gradient | Diffusant | $D$ |

Hence, similar theoretical frameworks have been used to study the effective properties of different heterogeneous materials.

### 2.7.1 Previous Models

In general, the different approaches to study the effective properties of heterogeneous materials are divided into two classes: continuum and discrete methods. Continuum models are based on the physical laws that govern transport processes at the microscopic level, resulting in a set of differential equations and their associated initial and boundary conditions. Unfortunately, the morphology of composite materials is very complex, and in many cases unknown. Thus, taking the average over appropriate volumes and estimating the effective properties is very difficult in general – even using numerical calculations. Hence various approximations such as the effective medium theory (the replacement of the heterogeneous material by an effective homogenous medium with a conductivity similar to the effective conductivity $k_e$, and solving a Laplace equation with appropriate boundary conditions) have been developed to estimate the effective properties of composite materials.

A number of theoretical approaches have been suggested to calculate the effective thermal conductivity of composites. Early analytical (continuum) models include the Maxwell equation,[40] the Bruggeman equation,[41] and modified versions thereof[33,42] (see Table 2.2). Several numerical approaches (based on discrete models) have been also suggested such as the Nielsen model,[43] the percolation model,[44] and random resistor networks.[45,13] One of the main drawbacks of most commonly used methods is that they do not show good agreement with the experimental data when the volume fraction of filler particles is high. For instance, the Maxwell-Garnett effective medium model was shown to be a good approximation only for low volume fractions (below 40%).[13] The results obtained from Nielsen's model are only reasonable for filler volume

fraction below 50%, whereas commercial TIM are typically loaded in excess of 60% by volume with conductive particles.[44] Bruggeman's symmetric/asymmetric model has been used to estimate the effective thermal conductivity of composites for high volume fractions, resulting in reasonable predictions for spherical particles.[13] For large differences in thermal conductivity between the filler particles and the polymer matrix, Devpura *et al.*[44] used the percolation theory and an applied transfer matrix technique (originally developed for electrical networks) to calculate the effective conductivity of composites. Their approach agreed well with experimental data over a broad range of filler particle volume fractions. However the predicted conductivity displayed a sudden increase when the filler fraction reached the percolation threshold. Moreover, this method cannot be easily generalized to include different filler geometries and size polydispersity.

Since most thermal interface materials use solid fillers to increase their thermal conductivity ($k_{\mathrm{TIM}}$), these systems can be treated as composites. In general, the thermal conductivity of any composite can be written as[39]

$$k = f(k_m, k_p, R_b, \varphi) \quad (2.8)$$

where $k_m$ and $k_p$ are the thermal conductivity of the polymer matrix and the solid particles ($W/mK$), respectively, $R_b$ is the interface resistance between the particle and the matrix ($Km^2/W$), and $\varphi$ is the volume fraction of particles. These parameters are also used in the equations listed in Table 2.2, where $\alpha$ is dimensionless and defined as $\alpha = 2R_b k_m/d$, where $d$ is the particle diameter.

In addition, different approaches have been developed to determine the upper and lower bounds of the effective properties and narrow them down to a range of possible values. As a simple example, using only the volume fractions and thermal conductivities of the matrix and the

particles, one can obtain the upper bound if the two phases are arranged parallel to the direction of heat flow (Figure 2.9 A), and the lower bound if the two components are ordered perpendicularly to the direction of heat flow (Figure 2.9 B).

**Table 2.2 Models to predict the thermal conductivity of TIM with filler particles.[13]**

| Name of the Model | Formula | Remarks |
|---|---|---|
| Maxwell-Garnett with $R_b$ | $\frac{k}{k_m} = \frac{[k_p(1+2\alpha)+2k_m]+2\varphi[k_p(1-\alpha)-k_m]}{[k_p(1+2\alpha)+2k_m]-\varphi[k_p(1-\alpha)-k_m]}$ <br> $\alpha = \frac{2R_b k_m}{d}$ <br> $\frac{k}{k_m} = \frac{(1+2\alpha)+2\varphi(1-\alpha)}{(1+2\alpha)-\varphi(1-\alpha)}\ for\ k_p \gg k_m$ | Spherical particles. Typically valid for $\varphi < 0.4$. |
| Bruggeman symmetric model | $(1-\varphi)\frac{k_m-k}{k_m+2k} + \varphi\frac{k_p-k}{k_p+2k} = 0$ <br> ($R_b$ not included) | Spherical particles. Typically good at higher $\varphi$. |
| Bruggeman asymmetric model | $(1-\varphi)^3 = \left(\frac{k_m}{k}\right)^{(1+2\alpha)/(1-\alpha)} \times \left\{\frac{k-k_p(1-\alpha)}{k_m-k_p(1-\alpha)}\right\}^{3/(1-\alpha)}$ <br> $\frac{k}{k_m} = \frac{1}{(1-\varphi)^{3(1-\alpha)/(1+2\alpha)}}\ for k_p \gg k_m$ | Spherical particles. |

We have

$$\frac{1}{k_{\mathrm{eff}}^{\parallel}} = \frac{\varphi}{k_{\mathrm{p}}} + \frac{(1-\varphi)}{k_m} \tag{2.9}$$

$$k_{\mathrm{eff}}^{\perp} = \varphi k_{\mathrm{p}} + (1-\varphi) k_{\mathrm{m}}$$

where $\varphi$ is the volume fraction of the filler particles, while $k_{\mathrm{p}}$ and $k_m$ are the thermal conductivity of the particles and the matrix, respectively. Several methods have been developed to extend these approximations and provide more accurate upper and lower bounds for the effective thermal conductivity of heterogeneous materials.[46]

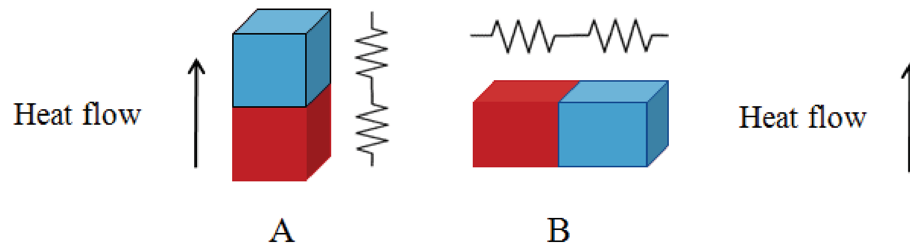


**Figure 2.9 Two phases ordered parallel (A) and perpendicularly (B) to the direction of heat flow (red: matrix, blue: metal).**

Furthermore, in discrete models the composite material is considered as a lattice. The lattice elements represent microscopic units (for example, either thermally conducting elements in the TIM or interstitial matrix elements). These models have been successfully applied to estimate the effective electrical and thermal conductivity of heterogeneous materials, but their main limitation is the requirement of extensive computational efforts.

Random resistor networks (RRN) have been introduced in recent years because they provide the simplest type of model for an inhomogeneous conductor.[47] The RRN method is a useful numerical technique to estimate the effective conductivity of composite materials. This

model was selected to predict the thermal conductivity of the TIM investigated herein, due to its ability to include high volume fractions of particles as well as to consider particle geometry and size polydispersity. The details of this model will be reported in Chapter 5.

This model uses the analogy between thermal and electrical conductivity.[39] In an electrical network, the current conservation equation at each node (i) from Kirchhoff's law is given by Equation (2.10)

$$\sum_j I_{ij} = \sum_j g_{ij}\left(V_i - V_j\right) = 0 \tag{2.10}$$

where $I_{ij}$ is the current in a bond $ij$, $g_{ij}$ is the bond conductance, while $V_i$ and $V_j$ are the voltages at sites $i$ and $j$. The above equation can be solved for given conductance distribution to obtain the voltage distribution in the network, and the effective thermal conductivity of the network can be calculated by applying Ohm's law ($I = V/R$) across the material. The details of this model will be reported in Chapter 5.

# Chapter 3

## Synthesis of α-Amino Oligo(ethylene oxide) and Binding on Copper Surfaces

## 3.1 Overview

We report two methods for the preparation of amino-functionalized monotelechelic oligomers of ethylene oxide, PEO-$NH_2$, firstly the anionic polymerization of ethylene oxide initiated by the potassium salt of 2-ethanolamine, and secondly the chemical modification of a commercial oligo(ethylene glycol) monomethyl ether sample. These oligomers were used to bind on copper surfaces, with the goal of making them electrically insulating. Infrared spectroscopy (IR) confirmed the presence of primary amino groups in the oligomer chains, while X-ray photoelectron spectroscopy (XPS) and contact angle measurements provided evidence for interactions (binding) of the amine groups with the metallic surfaces and/or their oxide layer. The XPS results indicated the presence of bonds between PEO-$NH_2$ and the copper surfaces. Resistivity measurements showed that copper flakes became essentially electrically insulating after being encapsulated by the oligomers, the resistivity being higher for PEO-$NH_2$ oligomer samples where residual salt contaminants had been removed more thoroughly.

## 3.2 Introduction

Anionic polymerization is a type of chain addition reaction in which the propagating center bears a negative charge. This method of polymer synthesis typically yields chains with controlled molecular weight and a narrow molecular weight distribution, and has been widely used (among others) for the preparation of telechelic polymers,[1] which are characterized by the presence of specific functional groups at one or both chain ends. Examples of such functional groups include hydroxyl (–OH), carboxyl (–COOH), or primary amine (–$NH_2$) functionalities.[2] Living polymerization techniques, for which the propagating center remains active throughout the whole

process, and in particular anionic living polymerization, are convenient for the synthesis of telechelic polymers because they allow the introduction of functional groups at one or both ends of the polymer chain with relative ease. This can be accomplished by termination of the living chain with an agent containing the desired functional group,[3] and/or by initiation of the chain with a suitably functionalized initiator.[4] Telechelic polymers are useful in multiple applications including surface modification,[5] as drug delivery systems,[6] or as precursors in the synthesis of block copolymers.[7]

In the current investigation we have determined that telechelic polymers are useful in the preparation of thermal interface materials (TIM), used in electronic equipment to enhance heat transfer between an electronic component (package) and a heat sink. A major challenge in TIM formulation is to ensure that the material is electrically insulating, while maintaining a high thermal conductivity (see Chapters 2 and 4). While thermal conductivity is of primary importance in these applications, proper selection of the polymer serving as binder in the formulation is also essential. It will be demonstrated in Chapter 4 that formulations incorporating metallic particles that are intrinsically electrically insulating can help to increase the thermal conductivity of the TIM. Another method to achieve this goal, which is the main focus of this Thesis, is to use telechelic oligomers with a metal-binding functional group at one end to effectively encapsulate conductive metallic particles.

With this goal in mind the interactions of PEO-$NH_2$ with copper were investigated, as it was discovered that this oligomer has the ability to bind at the surface of metals and/or the oxide layer at their surface, thus providing electrical insulation to the particles. X-ray photoelectron spectroscopy (XPS)[8,9] and contact angle measurements[10] both confirmed the formation of bonds

between these materials. Infrared radiation (IR) spectroscopy[9] also served to characterize the binding interactions between copper and PEO-$NH_2$.

## 3.3 Experimental Procedures

### 3.3.1 Ethylene Oxide Purification

Ethylene oxide (EO, Eastman Kodak) was purified on a high vacuum (HV) line. This compound is extremely toxic and volatile (b.p. 10 °C), so it should be handled carefully in a well-ventilated fume hood. An EO ampoule (ca. 100 g) was cooled to 0 °C and transferred to an ampoule with a Teflon stopcock, a magnetic stirring bar, and approximately 2 g of calcium hydride ($CaH_2$) as a drying agent. The mixture was stirred in the sealed ampoule at room temperature overnight. The ampoule was then mounted on a vacuum manifold equipped with a round-bottomed flask (RBF) and another sealable ampoule, as shown in Figure 3.1. The monomer was degassed with three successive cycles of freezing, evacuation, and thawing. After sealing the ampoule containing the EO, the remainder of the manifold was evacuated and flamed to remove adsorbed water. After purging the apparatus with dry nitrogen, 9 ml (8.82 g) of phenylmagnesium chloride solution (PhMgCl, Aldrich, 2.0 M in tetrahydrofuran, THF) was added to flask (B) with a syringe. The solvent was removed under vacuum and the EO was recondensed to the flask. The EO was stirred with PhMgCl for 1 h while cooled in an ice/water bath, to minimize polymerization and maintain a low vapor pressure. The purified EO was then slowly recondensed (over 3 – 4 h) to the storage ampoule (A).

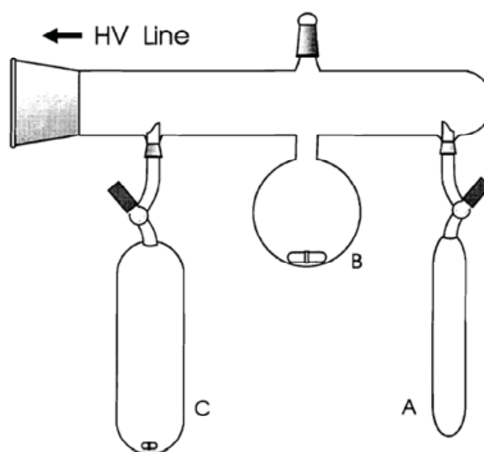


**Figure 3.1 Setup for EO purification on a vacuum line (A: purified monomer storage ampoule, B: round-bottomed flask, C: monomer ampoule). Adapted from Reference (11).**

### 3.3.2 Purification of 2-Ethanolamine

Ethanolamine (Aldrich, 50 ml) was stirred over magnesium metal (ca. 1.6 g) in a RBF for 10 hours, distilled at 70 °C under dry nitrogen, and stored under nitrogen in a Schlenk flask.

### 3.3.3 Diphenylmethylpotassium

Diphenylmethylpotassium (DPMK) was prepared in two steps as previously reported.[4] A 500 ml three-neck RBF containing a magnetic stirring bar was connected to the HV line, evacuated, and flamed. The flask was purged with dry nitrogen and naphthalene (16 g, 0.125 mol) was added, followed by freshly distilled THF (~120 ml). After stirring for 15 min potassium metal (4.56 g, 0.117 mol) was added, causing the colorless solution to turn dark olive green, and the solution was stirred further at room temperature under nitrogen for 10 h. The resulting dark green potassium naphthalide solution was filtered with a Schlenk funnel under nitrogen atmosphere. The potassium naphthalide concentration was determined by triplicate titrations of 100 mg

samples of 2,6-di-*tert*-butyl-4-methyl phenol (BHT), yielding an average concentration of 0.96 ± 0.05 M. The solution was stored in a Schlenk flask under nitrogen in a freezer at -20 °C.

In the second step of the DPMK synthesis, potassium naphthalide was reacted with diphenylmethane in the following manner. A 500 ml three-neck RBF was attached to the HV line, evacuated, and flamed. After filling with nitrogen, 16.5 ml (0.099 mol, 16.67 g) of diphenylmethane and 100 ml (0.096 mol) of potassium naphthalide solution were added. The flask was then removed from the HV line but kept under nitrogen and stirred overnight, leading to a color change from dark green to bright red. The DPMK solution was stored in the refrigerator (4 °C) under nitrogen in a Schlenk flask. Repeating the titration of the DPMK solution with BHT three times yielded an average concentration of 1.06 ± 0.05 M (the concentration was slightly higher than the potassium naphthalide solution due to solvent evaporation).

### 3.3.4 Polymerization of Ethylene Oxide (EO)

A thick wall ampoule was installed on the HV manifold, together with a purified EO ampoule (23.7 g, 0.54 mol), as shown in Figure 3.2. All the components, with the exception of the EO ampoule, were evacuated and flamed to remove adsorbed moisture. After purging with nitrogen, the stopcock of the thick wall ampoule was removed and 6.1 ml (0.101 mol) of 2-ethanolamine, 40 ml of dry THF, and 95 ml (0.099 mol) of DPMK solution were added. This corresponds to a calculated number-average molecular weight ($M_n$) of 281 g/mol, or a number-average degree of polymerization ($DP_n$) of 5.

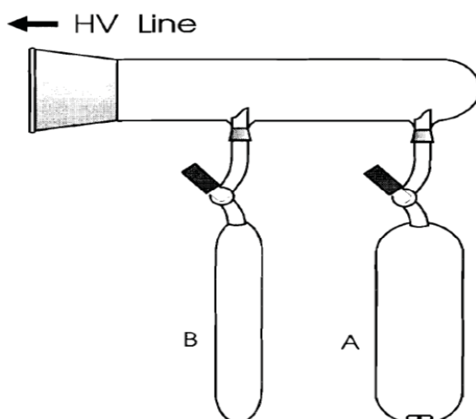


**Figure 3.2 Polymerization manifold (A: thick wall reaction ampoule, B: purified monomer ampoule). Adapted from Reference (11).**

The ampoule was purged with nitrogen, sealed, and stirred for 3 h at 30 °C in an oil bath. The ampoule was then frozen in liquid nitrogen, evacuated, and the stopcock of the EO ampoule was slowly opened to recondense the monomer to the thick wall ampoule (B) containing the initiator. After the transfer, the ampoule was brought to room temperature, filled with nitrogen, removed from the manifold, and placed in a 35 °C oil bath. The reaction was stirred for 20 h to achieve nearly complete monomer conversion. The color of the solution turned brown during the reaction, and to light brown when the reaction was terminated by adding 8 ml of 1% aqueous HCl. The polymer, denoted as PEO5-$NH_2$, was recovered and purified by liquid-liquid extraction using hexane and water following concentration by rotary evaporation. For further purification, PEO5-$NH_2$ was passed through a column (7 mm diameter and 80 mm length) of Celite 545 (Aldrich).

A similar procedure was used for the synthesis of an oligomeric EO sample with $DP_n$ = 15 (PEO15-$NH_2$).

### 3.3.5 Alternate Method for MPEG-$NH_2$ Synthesis

Another approach was investigated to prepare the telechelic polymers, by the modification of commercial oligo(ethylene glycol) monomethyl ether (Aldrich, $M_n$ = 550 g/mol), also known as methoxy poly(ethylene glycol) or MPEG. The reaction conditions used were based on those reported by Zalipsky et al.[12] MPEG (22.4 g, 20.5 ml, 40.2 mmol) and pyridine (3.2 g, 3.2 ml, 40.2 mmol) were stirred in a 100 ml RBF for 5 min, and thionyl chloride (14.4 g, 8.8 ml, 121 mmol) was added drop-wise. The colorless solution turned light pink, and the formation of pyridinium hydrochloride and the evolution of $SO_2$ gas were evident. The reaction was allowed to proceed under reflux (100 °C) for 5 h, leading to a color change to dark orange-red. After cooling the solution was filtered on a Buchner funnel, stirred with anhydrous $K_2CO_3$, and filtered again to remove excess $K_2CO_3$. The resulting MPEG-Cl was dried and obtained in 90% yield (19.8 g).

For the amination reaction, MPEG-Cl (19.8 g, 34.9 mmol) was mixed with 60 ml of ammonium hydroxide ($NH_4OH$, EMD Chemicals) solution in water (28 - 30 % wt) in a round bottom flask with magnetic stirrer bar. The flask was sealed and solution was allowed to react for 2 days at 50 $^oC$. Then the solution was cooled to room temperature, and excess $NH_4OH$ and the water were removed using a rotary evaporator. The MPEG-$NH_2$ was recovered and purified by liquid-liquid extraction with hexane and water (85 % yield, 16.8 g).

### 3.3.6 Polymer Characterization

The oligomers were characterized by $^1H$ NMR spectroscopy on a Bruker 300 MHz instrument at each step of the reaction. The spectra were obtained in deuterated chloroform ($CDCl_3$, 2 mg/ml) and analyzed with the MestReC software package after accumulating 16 scans. $^1H$ NMR analysis

confirmed the presence of primary amines and provided the $M_n$ for each sample, using the mole ratio of C**H**$_2$–$NH_2$ to the -C**H**$_2$-C**H**$_2$O- protons.

Size exclusion chromatography (SEC) was also used for molecular weight and polydispersity analysis. The SEC instrument consisted of a Waters Model 510 solvent delivery pump, a Waters R401 differential refractometer detector, and a 500 mm Jordi DVB mixed-bed column with a polystyrene molecular weight range of $10^2$ - $10^7$ g/mol. THF served as eluent and all the samples were run at room temperature at a flow rate of 1 ml/min, at a sample concentration of approximately 3 mg/ml. The instrument was calibrated with narrowly dispersed linear PEO standards in the molecular weight range 106-3120 g/mol, and the data were analyzed with the Astra Version 4.70.07 software package.

End-group titration was also used to determine the $M_n$ of one of the telechelic oligomer samples. This technique is applicable if it is assumed that there is one amine end-group for every chain in the sample. The titration of the amino end-groups was done with a perchloric acid solution in dichloromethane containing one to two drops of methyl violet (0.5 % solution in dichloromethane) as indicator. The perchloric acid solution was standardized by titration of three 50 mg samples of phenylethylamine in 15 ml of methylene chloride and a drop of indicator solution, resulting in an acid concentration of $0.101 \pm 0.008$ mol/l. The same procedure was used for the oligomer (PEO5-$NH_2$), yielding a $M_n$ value of $307 \pm 5$ g/mol.

Infrared (IR) spectroscopy analysis was used to confirm the presence of amino groups in the sample. The IR measurements were carried out on a Perkin-Elmer Spectrum RX I FT-IR spectrophotometer. One drop of the sample was placed between two sodium chloride disks and the spectrum was recorded from 500 – 4500 $cm^{-1}$. A peak is expected at 3370 $cm^{-1}$ for primary

amines ($NH_2$).[13] Comparison of the spectra with a spectral database[14] also confirmed the presence of primary amine functional groups in the three oligomers synthesized.

To investigate the interactions of the PEO-$NH_2$ oligomers with copper, bond formation was examined by XPS analysis, contact angle measurements, and electrical insulation resistance measurements. These methods are discussed in each of the following sections.

### 3.3.7 X-ray Photoelectron Spectroscopy (XPS)

XPS was used to confirm bonding between the primary amine functional group of the telechelic oligomers and the metal oxide layer and/or bare copper surface. The measurements were performed with a multi-technique ultra-high vacuum imaging XPS microprobe system (Thermo VG Scientific ESCALab 250) equipped with a hemispherical analyzer (150 mm mean radius) and a monochromatic AlK$\alpha$ (1486.60 eV) X-ray source. Since the XPS technique uses ultra-high vacuum (UHV) conditions, the samples must be dried prior to analysis. To this end, one drop of the oligomer was placed on the surface of a polished copper plate ($8 \times 6$ mm$^2$) and washed with 10 ml of acetone twice to rinse away any non-bound polymer. The copper plates in their bare state and after treatment with unmodified PEO (MPEG) and PEO-$NH_2$ were air-dried, attached to the circular sample holder of the instrument with double-sided adhesive metal tape, and placed in the XPS chamber. The sampling depth for this technique was approximately 1–30 nm, depending on the kinetic energy and the direction of the photoelectrons emitted.

The peaks for Cu2p, O1s, C1s, and N1s in both washed samples of MPEG and PEO-$NH_2$ were also studied individually for different sputtering times to confirm bonding of -$NH_2$ to the copper surface and the absence of the oligomer in the deeper layers of copper.

### 3.3.8 Contact Angle (CA) Measurements

The contact angle measurements were performed on both bare and treated copper plates ($30 \times 30$ $mm^2$) to determine the influence of PEO-$NH_2$ oligomers on the wetting properties of the copper substrate. The copper surfaces were carefully polished with a cotton buffering wheel. The surfaces were then cleaned with THF to remove buffering compound residues, submerged in a beaker filled with THF, and sonicated for 30 min. The plates were then dried using non-abrasive lint-free wipes (KimWipes). The CA measurements were performed for an apolar liquid (polydimethylsiloxane, PDMS) and for polar liquids (deionized water and ethylene glycol, EG) on the bare and PEG-treated copper surfaces. The copper surfaces treated with MPEG ($M_n$ = 550 g/mol) or with PEO-$NH_2$ ($DP_n$ = 5, 15) were obtained by coating the cleaned copper surfaces with a thin layer of the respective oligomers. After 5 min, the plates were washed with deionized water and allowed to dry under ambient conditions for 1 hour. One drop of liquid (50 µl) was then applied on each plate which was placed on the sample stage where the camera captured the images. The analysis software was set for 300 and 180 seconds with 1 and 0.5 second image capture intervals, respectively.

### 3.3.9 Resistivity Measurements

The electrical insulation properties of the samples were characterized through resistivity ($\rho,\ \Omega$m) measurements between two electrodes in a cell using a voltage of 50 to 1000 V (direct current, DC). This test was done to monitor the influence of the encapsulation of copper flakes on the electrical resistivity of the samples. For this purpose, a Teflon cell $(5 \times 5 \times 6\ \mathrm{mm}^2)$ was designed with two copper electrodes $(6 \times 7\ \mathrm{mm}^2)$ on opposite sides (Figure 3.3) that were connected to an insulation meter (FLUKE, model 1587). The resistance of the samples was measured and converted to resistivity using the equation $\rho = (R \times A)/L$ (where R is the

resistance, A is the cross sectional area, and L is the length of the cell). The empty cell was first tested to ensure that there was no leakage current (entry $S_1$ in Table 3.1 and Table 3.5). The cell was then completely filled with a sample and tested over the 50 – 1000 V range. The cell was cleaned with THF and air-dried between sample measurements.

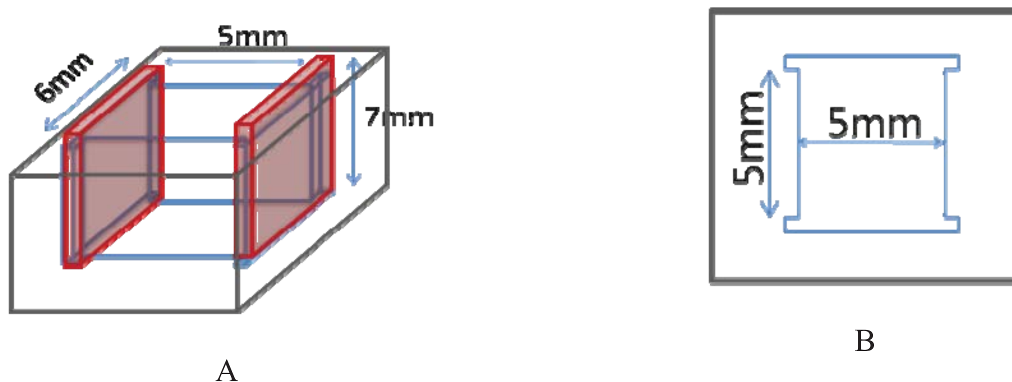


**Figure 3.3 Schematic view of the testing cell designed for the insulation resistance measurements, (A) with two electrodes and (B) view of the cell from the top.**

Four different TIM formulations were prepared and identified as $S_2$, $S_3$, $S_4$, and $S_5$ (see Table 3.1). Sample $S_2$ was prepared by mixing only 40% w/w triethylene glycol dimethyl ether (TriEGDME) and 60% w/w PEO5-$NH_2$, whereas sample $S_3$ was prepared in the same manner but using Celite-filtered PEO5-$NH_2$ i.e. the oligomer was passed through a column of Celite 545 (Aldrich). Sample $S_4$ was prepared by mixing Cu flakes (Umicore, $d_{50}$ = 3 μm), TriEGDME (40% w/w of liquid portion), and PEO5-$NH_2$ (60% w/w of the liquid portion) to obtain 86% w/w solids content, whereas for sample $S_5$ the Celite-filtered PEO5-$NH_2$ was used.

**Table 3.1 Samples for insulation resistance measurements.**

| $S_1$ | empty cell |
|---|---|
| $S_2$ | 60 % w/w PEO5-$NH_2$ + 40 % w/w TriEGDME |
| $S_3$ | 60 % w/w Filtered PEO5-$NH_2$ + 40 % w/w TriEGDME |
| $S_4$ | 86% w/w Cu + 8.4 % w/w PEO5-$NH_2$ + 5.6 % w/w TriEGDME |
| $S_5$ | 86% w/w Cu + 8.4 % w/w Filtered PEO5-$NH_2$ + 5.6 w/w % TriEGDME |

## 3.4 Results and Discussion

### 3.4.1 Synthesis

The EO oligomers were synthesized by anionic polymerization, and also by an alternate method based on the chemical modification of a commercial MPEG sample. The oligomers were characterized by different techniques including $^1H$ NMR spectroscopy and size exclusion chromatography (SEC), and end group titration. The $^1H$ NMR spectrum obtained for PEO5-$NH_2$ ($DP_n$ = 5) oligomers in $CDCl_3$ is shown in Figure 3.4, with the peaks assigned to -N**H₂**, -C**H₂**-$NH_2$, -C**H₂**-C**H₂**O-, and $CDCl_3$ labeled as A-D, respectively. The number-average molecular weights ($M_n$) for the different PEO-$NH_2$ samples synthesized, obtained by NMR and SEC analysis, are compared in Table 3.2. $DP_n$ corresponds to the subscript n in the formula $H_2N$-$CH_2$-$CH_2$-O-($CH_2$-$CH_2$-O)$_n$-H for PEO-$NH_2$ and $H_2N$-$CH_2$-$CH_2$-(O-$CH_2$-$CH_2$)$_n$-O-$CH_3$ for MPEG -$NH_2$. The values obtained by the different methods are in reasonable agreement except for the PEO15-$NH_2$ sample, synthesized with target $DP_n$ of 15. The results of $^1H$ NMR analysis yielded a lower $DP_n$ = 13 in that case, while the SEC results yielded $DP_n$ = 20, higher than the target $DP_n$. For the MPEG-$NH_2$ sample, the degree of polymerization provided by the supplier was 11 and the $^1H$ NMR analysis result was $DP_n$ = 13, while SEC analysis yielded $DP_n$ = 15. The higher

values obtained from SEC measurements could be related to interactions between PEO-$NH_2$ and the porous particles of the SEC column packing.

End group titration analysis was done only for sample PEO5-$NH_2$ and yielded a number-average molecular weight $M_n = 307 \pm 5$ g/mol, corresponding to $DP_n$ = 6 when excluding the ethanolamine fragment.

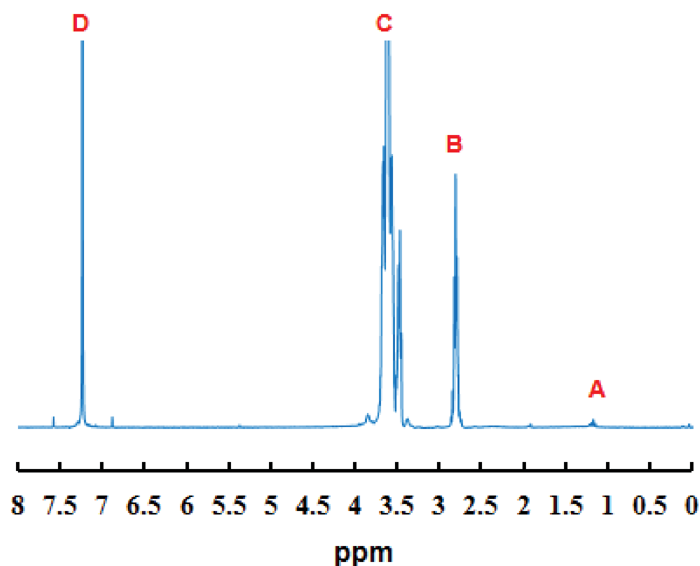


**Figure 3.4 $^1$H NMR spectrum for PEO5-$NH_2$ in deuterated chloroform.**

Oligomer density measurements were performed using a pycnometer. The procedure was repeated three times, resulting in an average density of $1.09 \pm 0.01$ g/ml for PEO5-$NH_2$, $1.13 \pm 0.01$ g/ml for PEO15-$NH_2$, and $1.17 \pm 0.01$ g/ml for MPEG-$NH_2$.

To investigate the interactions of the PEO-$NH_2$ oligomers with copper surfaces, XPS analysis, contact angle measurements, and electrical resistivity measurements were used. The results obtained by these methods are discussed in each of the following sections.

**Table 3.2 Molecular weight characterization of PEG-$NH_2$ oligomers by $^1H$ NMR and SEC analysis.**

| Oligomers | $M_n$ from $^1H$ NMR | $M_n$ from SEC |
|---|---|---|
| **PEO5-$NH_2$** | 281 g/mol ($DP_n$ = 5) | 320 g/mol (PDI=1.15) |
| **PEO15-$NH_2$** | 620 g/mol ($DP_n$ = 13) | 949 g/mol (PDI=1.19) |
| **MPEG-$NH_2$** | 619 g/mol ($DP_n$ = 13) | 724 g/mol (PDI=1.12) |

### 3.4.2 XPS Analysis

The XPS results shown in Figure 3.5 - Figure 3.9 confirm the presence of a nitrogen-containing compound bound on the surface of the samples treated with PEO5-$NH_2$ in the near surface region of the copper plate, and thus of -$NH_2$ groups bound to the metal oxide layer and/or the bare metal exposed at the surface (where the oxide layer was etched away).

Figure 3.5 shows the XPS survey (overall) spectra for Cu plates treated with the PEO5-$NH_2$ (A) and MPEG (B) samples. Each sample was placed on the Cu plate and then rinsed off with acetone before the measurement. The peaks in the spectrum correspond to electrons ejected due to the photoelectric effect and emission due to the Auger effect. The Auger effect happens when an electron from an outer shell of an atom fills the hole produced by an earlier XPS process. This electron transfers the energy difference to another electron which is emitted from the atom (Auger electron). The Auger electrons are emitted from the surface with kinetic energies which only depend on the electronic state of the element responsible for the ejected

electron. This means that the position of Auger lines does not change if the characteristic energy of the X-ray source changes.[15]

Peaks corresponding to the C1s, N1s, O1s, and Cu2p emissions appear at 284.7, 398.4, 532.5, and 933 eV, respectively.[15,16] The NIST database[16] can be used to facilitate the quantitative surface analysis of XPS spectra. Comparison of the two spectra shown in Figure 3.5 clearly indicates that there are very small peaks for C1s in the top spectrum for the washed MPEG sample. This means that very small amounts of oligomer residues were left on the surface after washing the MPEG-treated copper plate with acetone (i.e. the washing process was not quite sufficient to completely remove the oligomer, or due to handling). The Cu Auger features from the copper plate are more visible in this sample since the surface was not covered by the oligomer.

The O1s peak at 532.5 eV in the bottom spectrum (PEO-$NH_2$, A) is assigned to C-O-C from the oligomer backbone, and the Cu2p3/2 peaks at 933 eV correspond to CuO from the copper plate.[17,18] The presence of these peaks indicate that the PEO-$NH_2$ oligomers are not completely covering the surface of the copper plate, and there could be some defects or pinholes in the oligomer layer. This means that photoelectrons from the copper surface (through these defects or pinholes) can be detected by the XPS instrument (probing depth of 8-10 nm[15]). The intensity of the Cu-related peaks is nevertheless much smaller after treatment with PEO-$NH_2$ than in the top spectrum (MPEG, B). Therefore the spectrum for sample A, treated with PEO-$NH_2$, indicates that even after washing of the copper substrate the oligomer still persisted on the surface, suggesting that it was bound to the surface.

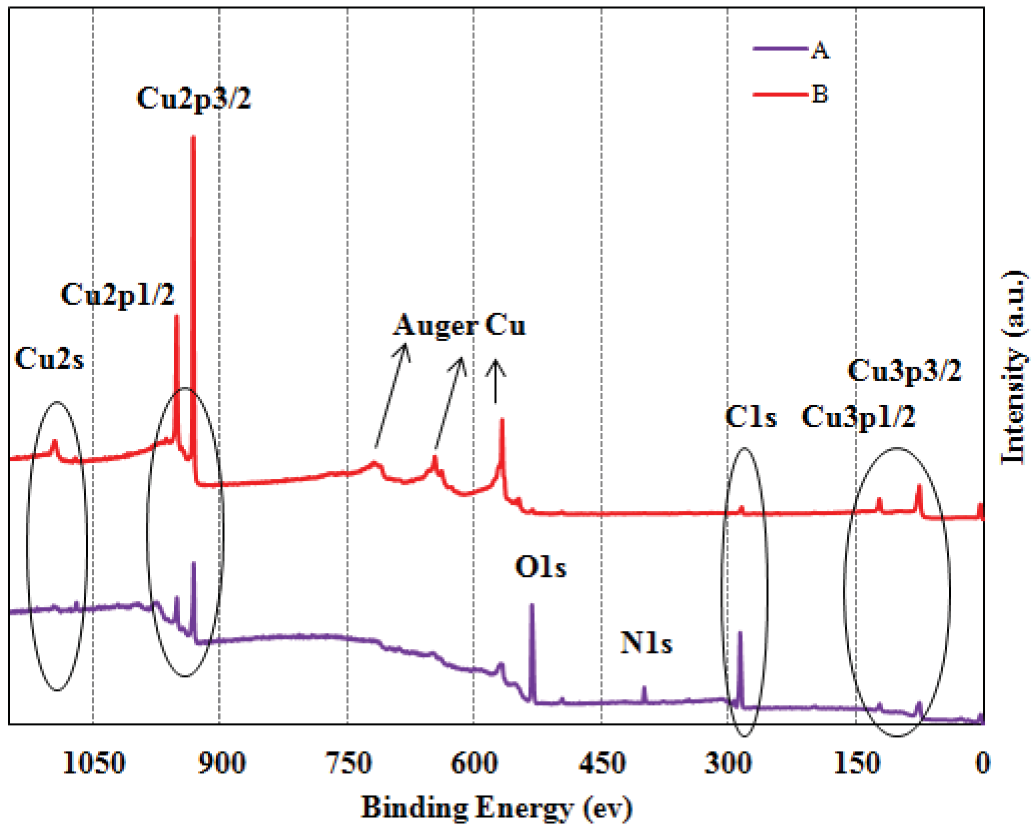


**Figure 3.5 XPS survey spectra for copper substrates treated with PEO-$NH_2$ (A, bottom, violet) and MPEG (B, top, red) samples.**

To study the inner layers of the surface, the depth profiling technique was used to reach these layers by etching the surface for a certain period of time (sputtering time). The peaks for Cu2p, O1s, C1s, and N1s in both washed samples of MPEG (B) and PEO-$NH_2$ (A) were studied individually for different sputtering times. At time zero there is a slight shift in the peak positions from 933 eV, presumably due to the presence of surface contaminants on the surface of the copper substrate.[15] Figure 3.6 shows the peak for Cu2p after sputtering of the surface for up to 10 min. Each line represents the XPS spectrum at different sputtering times. All the Cu2p peaks

have an asymmetrical shape at 933 eV for CuO, except the one present at t=0 due to contamination on the surface which is removed after 20 seconds of sputtering.

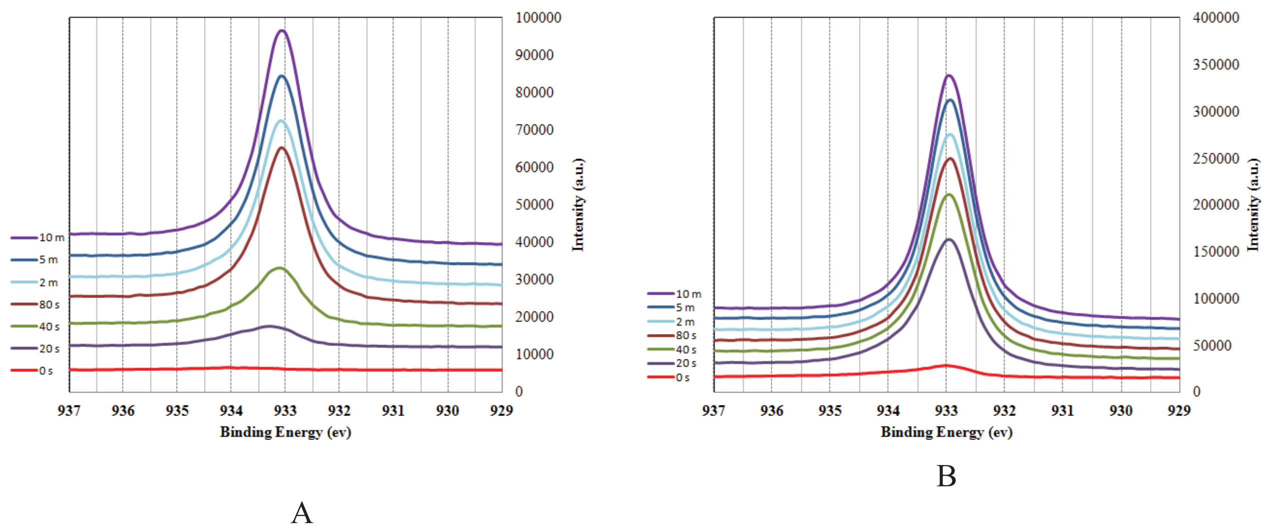


**Figure 3.6 XPS spectra for Cu2p peak of PEO-$NH_2$ (A) and MPEG (B) on copper substrate for different sputtering times (red = 0 s, dark blue = 20 s, green = 40 s, dark red = 80 s, light blue = 2 m, blue-green = 5 m, and purple = 10 m ).**

Before sputtering of the surface (time zero) no peak was observed in Figure 3.6A, but a peak of increasing intensity gradually appeared for longer sample sputtering times (after removing some of the oligomer layer from the Cu surface). In Figure 3.6B, for the MPEG-treated surface, the intensity of the peaks increased much more rapidly with sputtering time, and the peaks slightly shifted to 932.5 eV, which corresponds to bare Cu metal.[16]

The results in Figure 3.6A shows that even after 10 minutes of sputtering, the intensity of the Cu2p peak is still about one fourth of the intensity of the Cu2p peak in Figure 3.6B. This means that sputtering (cleaning) of the surface is not very efficient for the PEO-$NH_2$ oligomers, and 10 minutes of sputtering in not enough to completely remove the oligomer layer (this may

also depend on the initial thickness of the oligomer layer). Figure 3.7 shows the peaks corresponding to the O1s emission for copper plates after treatment with the PEO-$NH_2$ (A) and MPEG (B) samples and washing.

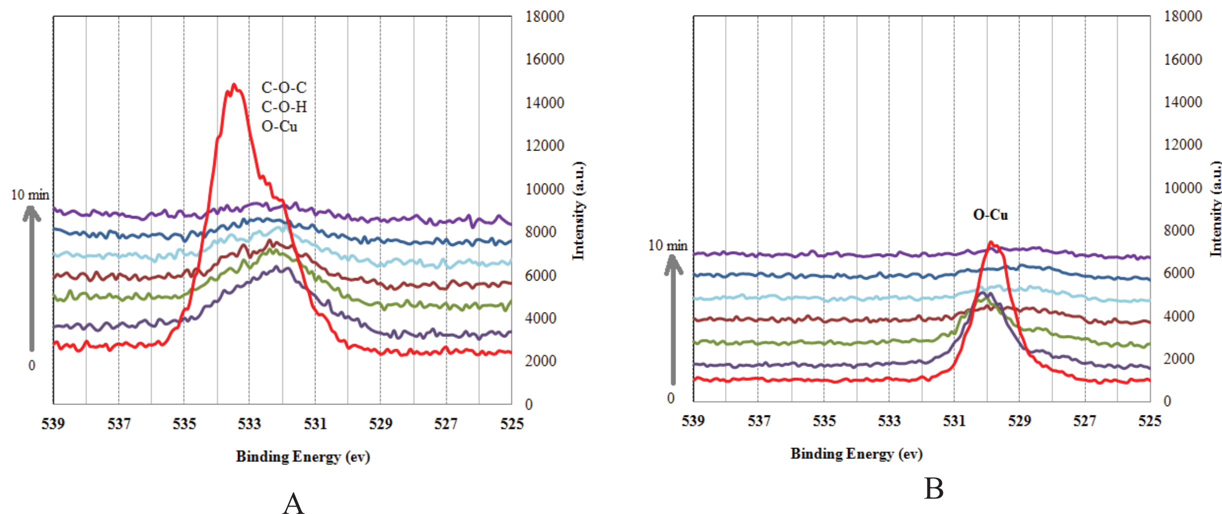


**Figure 3.7 XPS spectra for the O1s peaks of PEO-$NH_2$ (A) and MPEG (B) on copper for different sputtering times (same scale used for both samples).**

The asymmetrical peak in Figure 3.7A (PEO-$NH_2$), extending from 529 - 535 eV, correspond to the oxygen-carbon bonds (532.5 eV) and oxygen-hydrogen bonds (532.9 eV) of the PEO-$NH_2$ oligomers, and the oxygen-copper bond (530 eV), and is almost gone after 10 minutes of sputtering. The peak is much more intense in the spectrum at t = 0 due to presence of the oligomers on the surface, and slightly shifted due to surface contamination.

In Figure 3.7B, the peak at 530 eV corresponds to copper oxide, and is also flattened after sputtering for 10 minutes. The peak at time equal zero is slightly shifted due to presence of dirt (contamination) on the surface.

The C1s peaks were also studied, and the results obtained are shown in Figure 3.8 for PEO-$NH_2$ (A) and MPEG (B). There are four peaks in the 283 – 289 eV range for carbon bonds in Figure 3.8A, namely for C-H (285 eV), C-N (285.8 eV), C-C (286.5 eV), and C-O (287 eV) bonds.[15] An additional peak at 294 eV for the PEO-$NH_2$ sample is assigned to transitions from the C1s level to the $\sigma^*$ (C-N) bonds[19] and disappears after 5 min of sputtering. In Figure 3.8B, weaker peaks for the MPEG oligomer also appeared, meaning that washing the copper surface with acetone was insufficient to completely remove the oligomers residues from the surface.

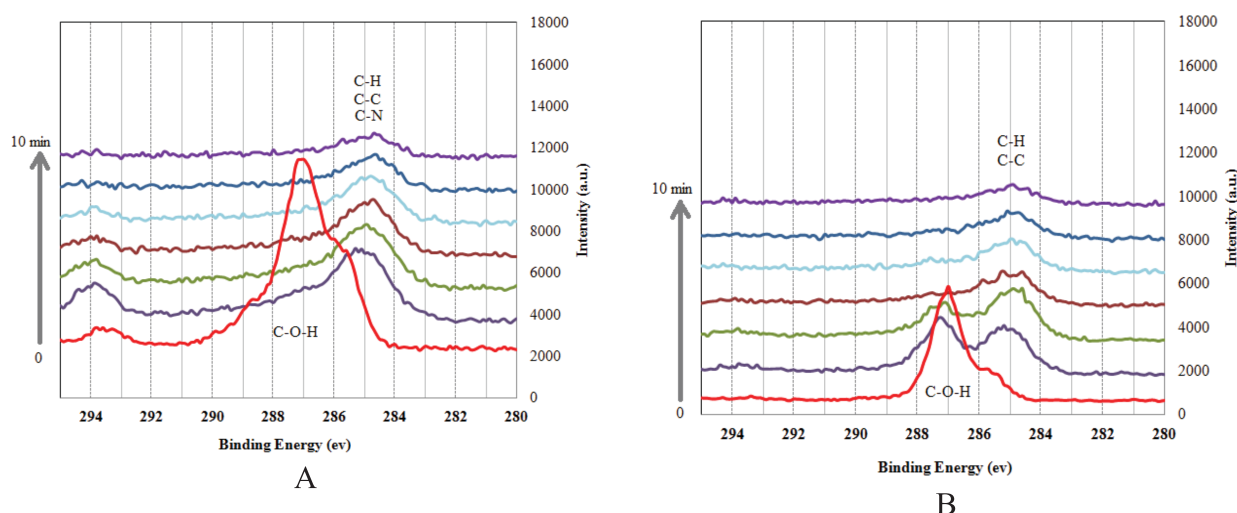


**Figure 3.8 XPS spectra for C1s peaks of PEO-$NH_2$ (A) and MPEG (B) on copper for different sputtering times.**

The peak for N1s on the washed copper substrate treated with PEO-$NH_2$ is shown in Figure 3.9 for different sputtering times. The peak at 400.8 eV at time equal to zero corresponds to C-$NH_2$ bonding,[20] and after 20 second sputtering, the peak is shifted toward 399 eV, which corresponds to Cu-$NH_2$ bonds, and it disappears from the copper surface after 2 min of sputtering. This means that the concentration of -$NH_2$ decreased (i.e. the N atoms were removed

from the surface). This peak disappears much faster relatively to the peaks in Figure 3.9, because there is only one -$NH_2$ residue per oligomer chain (lower atomic concentration). The black line in Figure 3.9 corresponds to the survey spectrum for the copper substrate treated with MPEG (top spectrum in Figure 3.5) and is plotted for comparison (absence of N atoms in the sample).

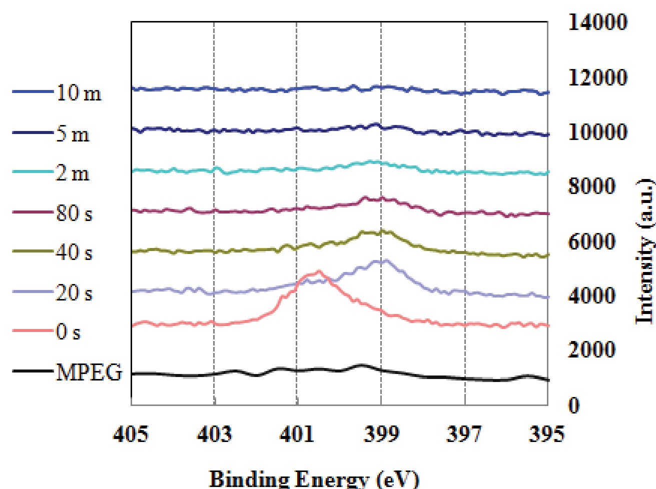


**Figure 3.9 XPS spectra for the N1s peak for copper substrate treated with MPEG (black line) and PEO-$NH_2$ for different sputtering times.**

### 3.4.3 Contact angle (CA) measurements

The optical contact angle (or sessile drop) method was used to study the influence of the PEO-$NH_2$ oligomers on the wetting properties of the copper substrate (see Chapter 2, Section 2.4). The uncertainty in the contact angle measurements obtained were typically 3 - 4$^o$, depending on the resolution of the images used. The measurements were repeated three times for each sample and the standard deviation was calculated. Table 3.3 provides the contact angles for the different copper surfaces (bare, MPEG-treated, and PEO5-$NH_2$-treated). The results obtained

for PEO15-$NH_2$ were essentially identical to PEO5-$NH_2$, and they are not shown in the table. The bare and treated surfaces were tested with different liquids by placing a drop of each liquid on the surface and measuring the contact angles. Since PDMS is very apolar, the contact angle measurements were the same on all the surfaces.

**Table 3.3 Contact angle of liquids on different surfaces.**

| Surface | Water | EG | PDMS |
|---|---|---|---|
| **Bare Cu** | 83° | 70° | 46° |
| **MPEG** | 69° | 54° | 46° |
| **PEO5-$NH_2$** | 43° | 41° | 46° |

Contact angle measurements can be used to determine the interfacial free energy or surface tension (the work required to increase the surface of a substance by one unit area).[21] According to the Lifshitz-van der Waals and Lewis acid-base (LW/AB) theory proposed by van Oss et al.,[10] the surface energy can be decomposed into two parts given by the equation (3.1)

$$\gamma = \gamma^{LW} + \gamma^{AB} = \gamma^{LW} + 2\sqrt{\gamma^{+}\gamma^{-}} \qquad (3.1)$$

where the superscript LW represents the Lifshitz-van der Waals interactions including London dispersion forces, Debye polarization, and Keeson forces, and AB represents the Lewis acid-base interactions. The parameters $\gamma^{+}$and $\gamma^{-}$correspond to the Lewis acid (electron acceptor) and Lewis base (electron donor) components of the surface energy, respectively. In order to determine the parameters $\gamma_S^{LW}$, $\gamma_S^{+}$ and $\gamma_S^{-}$, contact angle measurements with three liquids, one apolar and two polar (one being water) are required, using equation (3.2).[10,22]

$$\gamma_L(1 + cos\theta) = 2\left(\sqrt{\gamma_S^{LW}\gamma_L^{LW}} + \sqrt{\gamma_S^{+}\gamma_L^{-}} + \sqrt{\gamma_S^{-}\gamma_L^{+}}\right) \quad (3.2)$$

where $\theta$ is the contact angle obtained from image analysis. Equations 3.1 and 3.2 are used to calculate the unknown parameters above. The free energy of interfacial interaction is then obtained as Equation (3.3):

$$\Delta G_{SL}^{IF} = -2\left(\sqrt{\gamma_S^{LW}} - \sqrt{\gamma_L^{LW}}\right)^2 - 4\left(\sqrt{\gamma_S^{+}\gamma_S^{-}} + \sqrt{\gamma_L^{+}\gamma_L^{-}} - \sqrt{\gamma_S^{+}\gamma_L^{-}} - \sqrt{\gamma_S^{-}\gamma_L^{+}}\right) \quad (3.3)$$

Contact angle measurements were used to determine the parameters $\gamma_S^{LW}$, $\gamma_S^{+}$, $\gamma_S^{-}$, and subsequently $\Delta G_{SL}^{IF}$ according to that method, and the results obtained are summarized in Table 3.4. When $\Delta G_{SL}^{IF} < 0$ the substrate is considered hydrophobic, and the magnitude of the parameter qualifies the degree of hydrophobicity; conversely, $\Delta G_{SL}^{IF} \geq 0$ is associated with a hydrophilic substrate. Larger $\gamma^{+}$ (or $\gamma^{-}$) values relate to a stronger ability to accept (or provide) electrons. Our results clearly indicate that the surfaces coated with PEO5-$NH_2$ are less hydrophobic than the bare and unfunctionalized MPEG-treated surfaces.

**Table 3.4 Surface energy components and $\Delta G_{SL}^{IF}$ ($mJ/m^2$) for copper.**

| Surface | $\gamma_S^{LW}$ | $\gamma_S^{+}$ | $\gamma_S^{-}$ | $\Delta G_{SL}^{IF}$ |
|---|---|---|---|---|
| **Bare Cu** | 5.1 | 2.5 | 15.2 | $-25 \pm 2$ |
| **MPEG** | 5.1 | 4.3 | 20.6 | $-38 \pm 2$ |
| **PEO5-$NH_2$** | 5.1 | 74.7 | 0.2 | $-13 \pm 2$ |

### 3.4.4 Insulation Resistance Measurements

The insulation resistance results (the resistivity $\rho$, expressed in $\Omega$m ), determined at different DC voltages for various formulations, are listed in Table 3.5. The resistivity of bulk copper, a good

electrical conductor, is 17 nΩm.[24] The results given in Table 3.5 for samples $S_1$ show that there was negligible leakage current in the empty cell, and that samples $S_3$ and $S_5$, containing the Celite-filtered PEO-$NH_2$ oligomer, are better electrical insulators than the non-purified samples ($S_2$ and $S_4$). This is attributed to a lower concentration of conducting salt residues in the Celite-purified PEO-$NH_2$ sample. The results also show that the copper flakes were electrically insulated to a large extent, presumably due to their encapsulation by PEO-$NH_2$. Indeed, the resistivity of these samples was around $10^{11}$ times larger than for bulk copper. For the larger applied electric fields, the electrical resistivity remains constant; this is presumably related to overloading of the testing instrument.

**Table 3.5 The resistivity results for different samples.**

| Electric Field (V/mm) | $\rho$ (Ωm) $S_1$ | $\rho$ (Ωm) $S_2$ | $\rho$ (Ωm) $S_3$ | $\rho$ (Ωm) $S_4$ | $\rho$ (Ωm) $S_5$ |
|---|---|---|---|---|---|
| **10** | 462000 | 246 | 410 | 2050 | 5248 |
| **20** | 902000 | 246 | 492 | 2050 | 5166 |
| **50** | 2255000 | 0 | 820 | 1640 | 4920 |
| **100** | 4510000 | 0 | 820 | 820 | 4920 |
| **200** | NA | 0 | 820 | 820 | 820 |

## 3.5 Conclusions

PEO-$NH_2$ oligomers were synthesized either by anionic polymerization or through the chemical modification of MPEG oligomers. $^1$H NMR analysis was used to confirm the structure of the oligomers, including their molecular weight and the presence of a primary amine end group. Analysis by SEC and end group titration were also employed to determine the molecular weight

of the oligomers. IR spectroscopy analysis further confirmed the presence of primary amine end groups in the samples. The interactions of the PEO-$NH_2$ oligomers with copper surfaces were investigated using XPS, contact angle measurements, and electrical insulation resistance measurements. The results obtained in all cases were consistent with the presence of oligomers bonded to the surface of copper.

# Chapter 4

## Improved Thermal Interface Materials (TIM) for Applications in Microelectronics

## 4.1 Overview

Thermal interface materials (TIM) are used to facilitate heat transfer from electronic packages (e.g. microprocessors or other high power devices) to a heat sink. These materials consist of heat-conducting solid filler particles dispersed in a liquid matrix. In this research, different TIM compositions based on metallic particle fillers were investigated in a systematic fashion, to take advantage of the high intrinsic thermal conductivity of metals. A major challenge in TIM formulations with metallic fillers is to render these materials as much electrically insulating as possible, while maintaining a high effective thermal conductivity. To this end, mixtures of different metallic fillers and liquid polymeric matrices were examined. A novel type of end-reactive (telechelic) polymer was developed for the project, namely an ethylene oxide oligomer with an amino end group. This compound was found to be a very efficient additive in TIM formulations to promote matrix-filler interactions. The results obtained demonstrated significant improvements in the effective thermal conductivity of TIM formulations incorporating these oligomers as compared to formulations without them, as well as in comparison with commercial TIM samples.

## 4.2 Introduction

Heat transfer has been a subject of interest to the electronics industry for a long time. In applications such as microcomputers and telecommunications, where the size of components is typically small and the thermal density is high, heat transfer across contacting interfaces becomes an essential factor determining product reliability. Heat transfer across metallic or ceramic-metallic joints thus becomes an important problem in many microelectronic applications.

One common approach to improve heat dissipation in an electronic device involves heat sinks, as discussed in Chapter 2. However when two surfaces are in contact, the solid-solid mechanical contact usually occurs only over a very small fraction of the surface (< 3 %) due to surface roughness (see Figure 2.3 and Figure 2.4 in Chapter 2). Even for smooth surfaces under load, microroughness and uneven surface mating may reduce the actual contact area. These uneven interfaces present between an electronic package and a heat sink can play a major role in determining the thermal contact resistance, and ultimately heat dissipation.

Efficient heat removal from an electronic packaging involves three major steps: (a) heat transfer within the electronic package such as a CPU, (b) heat transfer from the package to the heat sink, and (c) heat transfer from the heat sink to the ambient environment. In this research, the main goal was to design materials enabling efficient heat transfer from the package surface to the heat sink. To achieve this goal, we focused on TIM formulations using different metallic filler particles and polymeric binders.

A TIM used between an electronic package and a heat sink fills the voids or air gaps and thus increases the effective contact area between the two surfaces.[1] It also helps to decrease the thermal joint resistance and the device operation temperature. Commonly used TIM in the industry include greases, oils, gases, thin metallic and non-metallic coatings, metallic foils, phase change materials, and polymeric composites.[2] In our research, we focus on fluidic-metallic filler mixtures.

Proper selection of the filler particle size and shape, as well as the type of polymer, is very important in increasing the effective contact area between an electronic package and a heat sink, which is necessary to reduce joint resistance and improve overall effective thermal conductivity (conductance), as discussed in Chapter 2. While many experimental and theoretical

studies have focused on the effects of filler particles in TIM compositions, less attention has been devoted to the polymer properties and their interactions with the fillers. One of our goals was therefore to find an oligomer that can bind to metallic surfaces, so as to form a stable but thin electrically insulating coating at the surface of metallic filler particles. One possibility to achieve this is to use telechelic polymers, containing functional groups at one or both chain ends.[3] In this work we studied the influence of several polymers and different filler particles on the effective thermal conductivity of the TIM. Specifically, polydimethylsiloxane (PDMS) and ethylene glycol oligomers (di-, tri- and tetraethylene glycol with either -OH or methoxy end groups) were compared. The effect of the addition of surface-active agents, and particularly ethylene oxide oligomers with an amino end group (PEO-$NH_2$) as surfactant, to the ethylene glycol oligomers was also studied. This surfactant has the ability to bind on metal surfaces such as copper, making it electrically insulating, as shown in Chapter 3, and also to increase the effective thermal conductivity of the TIM. The TIM formulations containing surfactant also showed better spreadability when they were applied to surfaces.

The influence of electrically insulated filler particles was studied according to two different strategies: by mixing electrically insulating and conducting particles below the percolation limit of the conducting component, and by encapsulating the filler with PEO-$NH_2$ surfactant or with silane coupling agents. The shape and size of the particles used in the TIM formulations were studied with SEM, testing sieves, and using a Coulter Counter Multisizer II.

## 4.3 Background and Method

### 4.3.1 Thermal Resistance Measurement Method

The thermal resistance was measured according to ASTM standard D 5470 (a standard cell for thermal resistance measurements across materials of known thickness), using an instrument designed in the Microelectronics Heat Transfer Laboratory (MHTL), Department of Mechanical and Mechatronics Engineering, University of Waterloo, as described in general terms in Chapter 2. This instrument consists of four basic units including the test column, loading, cooling, and measurement systems, as described in Section 2.5.2. Pictorial and schematic representations of the testing apparatus are provided in Figure 4.1 and Figure 4.2, respectively.

**Figure 4.1 Pictures of the system used.**

The temperature, current, voltage, and the load were automatically measured and controlled with a Keithley 2700 data logger and a custom-made LabView program. The temperature of each flux meter is determined based on the temperature gradient and location of each RTD in the blocks. An electric cartridge heater is installed in another copper block to heat the lower flux meter. The heat flux is measured to determine the interface resistance as discussed

in Chapter 2. The contact pressure is adjustable and ranges from 5 to 100 PSI. It is applied and measured to ensure efficient contact between the TIM and the upper and lower flux meter surfaces.

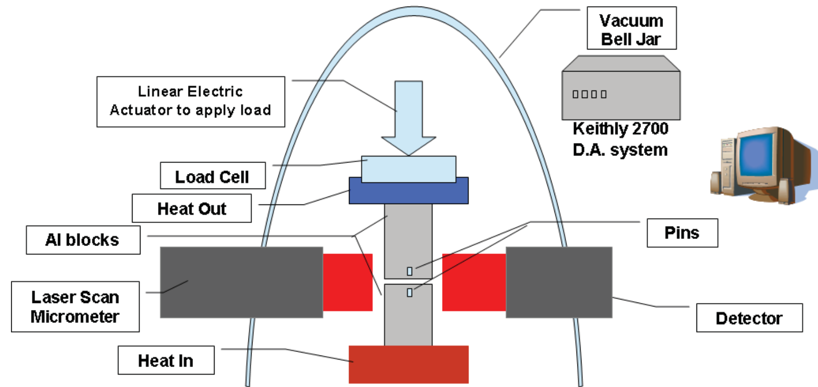


**Figure 4.2 Schematic representation of the system used.**

The flux meter surfaces are cleaned with acetone to eliminate contamination of the testing surfaces (e.g. residues of different TIM left in the surface asperities). The bond-line thickness (BLT), which is the layer thickness that supports the load and prevents direct surface contact, is measured with a laser-scan micrometer (Mitutoyo) with an accuracy of 0.3 % within a measurable range of 0.3 to 30 mm (with a resolution varying from 0.02 to 100 μm). Sample thickness is defined by $X - X_0$, where $X_0$ and X are the initial (without TIM) and secondary (with TIM) distances between the pins in Figure 4.3. The sample thickness was controlled for specific thicknesses using shims at the corners of the lower heat flux-meter, as shown in Figure 4.4.

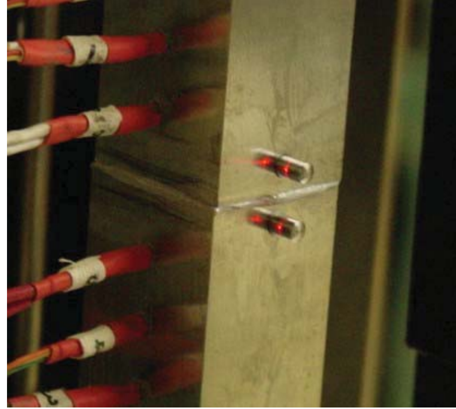

**Figure 4.3 Photograph of the flux meter with the pins used for the thickness measurements using a laser micrometer.**

Shims varying in thickness from 25.4 to 864 μm were used for the effective thermal conductivity measurements.

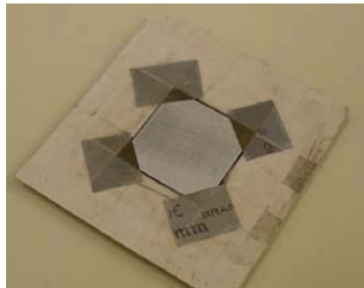

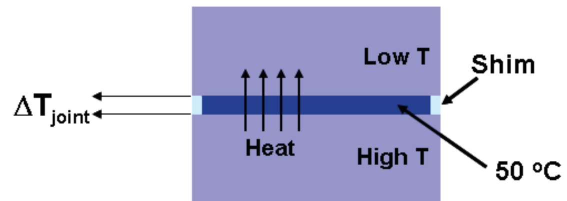


**Figure 4.4 (Left) A photograph of the flux meter with a shim. (Right) Schematic representation of the flux meter spacing with a shim.**

## 4.4 Experimental Procedure for TIM Preparations

### 4.4.1 Metallic Fillers Analysis

The metallic particles used as fillers in the TIM formulations were copper, aluminum, and silver, either in spherical powder or flake forms. The characteristics of the different particles used are summarized in Table 4.1.

**Table 4.1 Characteristics of the metallic particles used in the TIM formulations.**

| Filler ID | Metal | Supplier | Geometry | Average size | Electrically Conducting |
|---|---|---|---|---|---|
| **1** | Aluminum | A&C Amer. Chem. | Spherical | <65 μm | N |
| **2** | Aluminum | Anachemia | Spherical | <75 μm | N |
| **3** | Copper | Umicore | Flakes | 1 μm | Y |
| **4** | Copper | Umicore | Flakes | 3 μm | Y |
| **5** | Copper | Umicore | Flakes | 5 mm | Y |
| **6** | Copper | Umicore | Flakes | 8 μm | Y |
| **7** | Copper | Umicore | Flakes | 14 μm | Y |
| **8** | Copper | Umicore | Spherical | 1 μm | Y |
| **9** | Copper | Umicore | Spherical | 4 μm | Y |
| **10** | Copper | Aldrich | Spherical | <100 nm | Y |
| **11** | Copper | Aldrich | Spherical | 3 μm | Y |
| **12** | Copper | Aldrich | Spherical | <10 μm | Y |
| **13** | Silver | Aldrich | Flakes | <10 μm | Y |
| **14** | Silver | Alfa Aesar | Flakes | 4-8 μm | Y |
| **15** | Silver | Alfa Aesar | Flakes | <10 μm | Y |

#### 4.4.1.1 Testing Sieves

The particle size distribution of the aluminum powders (Anachemia and A & C) was determined using a series of testing sieves described in Table 4.2. Figure 4.5 provides examples of size distributions determined with the series of testing sieving for two different aluminum powders.

**Table 4.2 Testing sieves series for particles size analysis.**

| Sieve Description | Average Opening Size (μm) |
|---|---|
| **635** | 20 |
| **500** | 25 |
| **400** | 37 |
| **325** | 44 |
| **230** | 65 |
| **200** | 75 |

The results show that the A&C sample had smaller aluminum particles (< 65 μm) than the Anachemia sample (< 75 μm). For the size fraction below 20 μm (the smallest size fraction) a Coulter Counter Multisizer II was used for further analysis, which will be discussed in the next section.

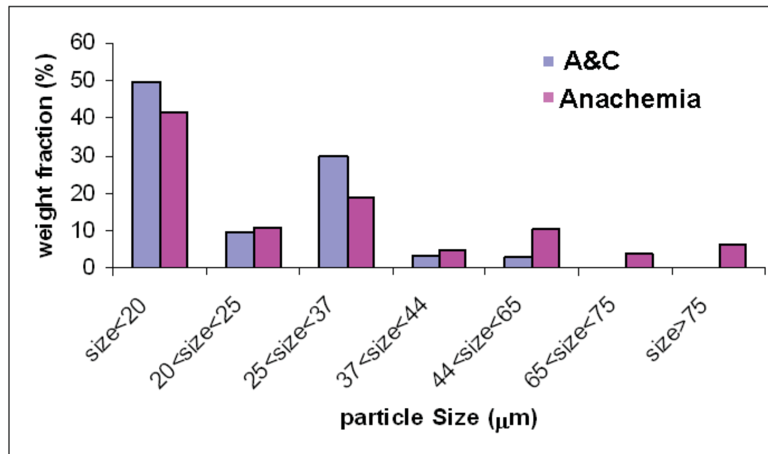


**Figure 4.5 Size distributions of aluminum powders determined by sieving.**

#### 4.4.1.2 Coulter Counter Multisizer II

Since the size distribution of filler particles is an important factor determining the performance of a TIM, the Coulter Counter Multisizer II was used to determine the size distribution of the Al particles in the smallest size fraction of the testing sieves. The instrument was calibrated using polystyrene latex particle samples with narrow size distributions and median diameters in the 5-20 μm range. A raw sample was prepared using 20 ml of electrolyte solution (Isoton II) and about 14 mg of the aluminum powder. The solution was shaken gently before each measurement. The instrument was first run for a background scan with only the Isoton II solution, and 4 ml of the raw sample were added to the sample jar of the instrument containing 250 ml of Isoton II. The results of the coulter counter measurements indicate the large number fractions for the particles with diameter of two microns and lower (Figure 4.6).

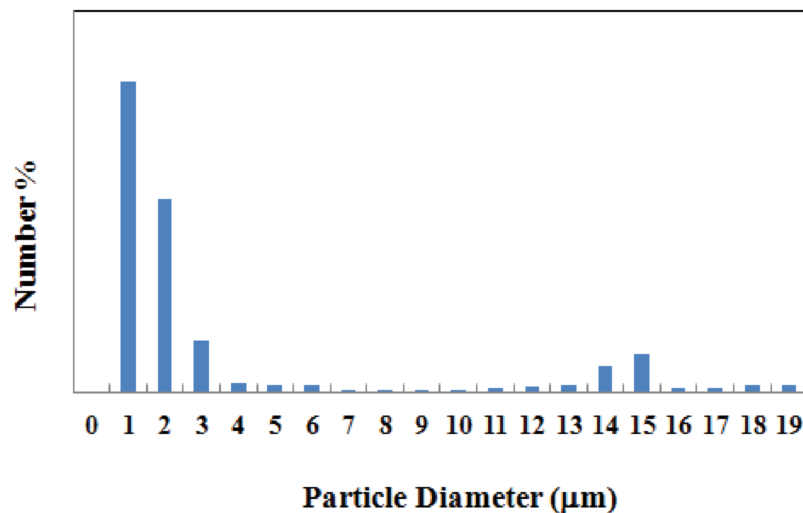


**Figure 4.6 Coulter counter result for the smallest Al powder fraction of the testing sieves.**

#### 4.4.1.3 Scanning Electron Microscopy

We compared the geometry, the size distribution, and the appearance of Al particle samples from two suppliers (A&C American Chemicals and Anachemia), as well as silver flakes (Aldrich, size <10 μm) and copper flakes (Umicore, $d_{50}$ =3 μm, typical ratio of large diameter to thickness 3:1 and typical aspect ratio 3:2). The SEM images for the Al powder (Anachemia), the Cu flakes, and the Ag flakes are shown in Figure 4.7 and Figure 4.8.

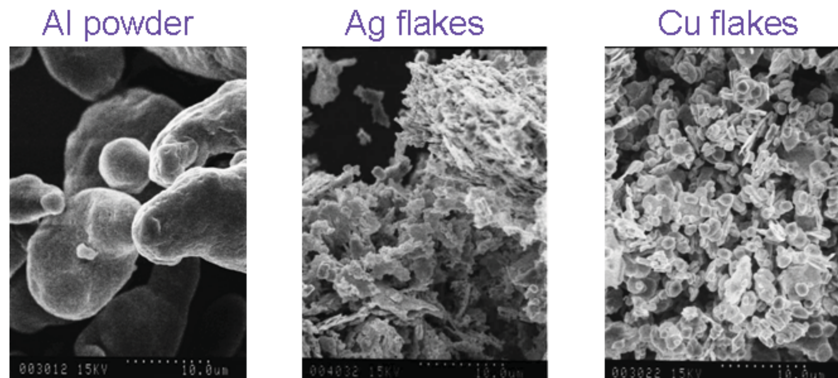


**Figure 4.7 SEM pictures of metallic fillers (scale 10 μm).**

.

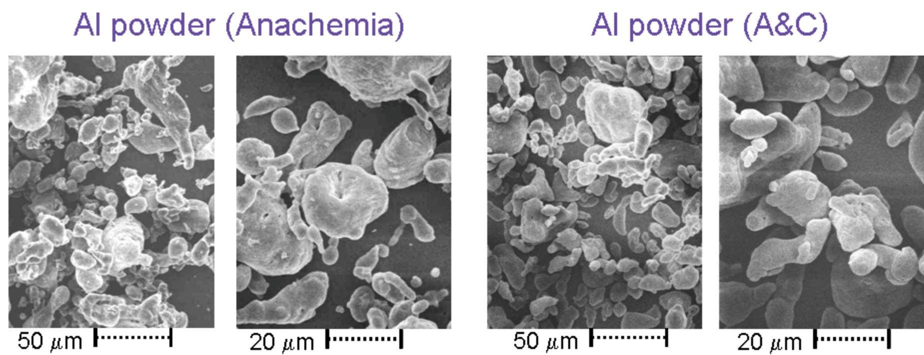


**Figure 4.8 SEM pictures for aluminum powders.**

### 4.4.2 Electrically Insulating Methods

A major challenge in TIM formulation with metallic filler particles is to maintain the composite electrically insulating while achieving a high effective thermal conductivity. Different strategies were investigated to make the TIM formulations electrically insulating.

**Mixing fillers:** The aluminum particles were found to be electrically insulating, while the copper and silver particles were good electrical conductors. The aluminum powders are thought to be electrically insulating due to the presence of a metal oxide (alumina) layer on their surface. Mixing electrically insulating and conducting particles with different geometries, while staying below the percolation limit of the conducting component, was therefore investigated as a method to maximize the effective thermal conductivity of the TIM formulations. Under these conditions, the thickness of the oxide layer at the surface of the metallic particles can be an important parameter controlling the effective thermal conductivity of the TIM. Any path interruption between the filler particles due to air gaps or the alumina layer decreases the effective thermal conductivity due to their insulating character. A higher effective thermal conductivity may therefore be achieved with electrically insulating metallic particles (through their metal oxide layer) with minimal separation. For that reason, we studied the effective thermal conductivity of TIM formulations prepared from aluminum particles with different particle size and oxide contents, as will be discussed in the Results section.

**Particle encapsulation:** An alternative method to render metallic particles such as copper flakes electrically insulating is through encapsulation with coupling agents and PEO-$NH_2$ (e.g. Chapter 3). Functionalized organosilanes were investigated for their ability to bind to inorganic substrates and form complexes with the metal oxide layer. Four different silane coupling agents were used to encapsulate the copper flakes and make them electrically

insulating. Bis(trimethoxysilyl)hexane, 1,2-bis(trimethoxysilyl)decane, N-(2-aminoethyl)-3-aminopropylsilanetriol, and 3-trimethoxysilylpropyldiethylenetriamine were purchased from Gelest Inc. A dispersion of 1 g of copper flakes ($d_{50}$ =3 μm) in 1 g of hexane was mixed with 0.10 g of the coupling agent. The dispersions were stirred for 1.5 hour and centrifuged. The residual solvent was allowed to dry in a fume hood overnight and the treated copper flakes were placed in a vacuum oven for 16 hours at 120 °C. All the samples formed rigid aggregates after curing. With the exception of the sample prepared with trimethoxysilylpropyl-diethylenetriamine, the samples were electrically conductive. The procedure was repeated but the copper flakes were washed and sonicated with hexane after centrifugation and the solvent was decanted to prevent the formation of rigid aggregates. Bis(trimethoxy silyl)hexane and 1,2-bis(trimethoxysilyl)decane formed rigid aggregates again, while N-(2-aminoethyl)-3-aminopropylsilanetriol and 3-trimethoxysilylpropyl-diethylenetriamine formed coarse powders. All the samples were electrically conductive. In a different attempt, the 1 g copper flake samples ($d_{50}$ =3 μm) were treated with 5% wt of the coupling agents (0.05 g) in 1 g of toluene. After 3 hours of stirring, 0.1 g of deionized water (5% of total weight for each sample) was added to the dispersions that were stirred for another hour to induce the hydrolysis of the coupling agents. The solutions were centrifuged, the solvents were decanted, and the copper flakes were left in a fume hood overnight to dry before placing them in a vacuum oven for 16 hours at 120 °C. The first and second samples formed rigid aggregates and the last two formed coarse powders. All the samples were electrically conducting, except for the one treated with 3-trimethoxysilylpropyl-diethylenetriamine. The same procedure was repeated with the addition of 10 % wt of deionized water (0.2 g) to each sample after five hours of stirring with the silane coupling agent. The solutions were stirred with water overnight, centrifuged, dried, and placed in a vacuum oven for

16 hours at 120 °C. The samples displayed the same results as those obtained by the previous method. The two coupling agents bis(trimethoxy silyl)hexane and 1,2-bis(trimethoxysilyl)decane were thus abandoned because they did not display insulating properties for the copper flakes. N-(2-Aminoethyl)-3-aminopropylsilanetriol was tested again in two samples with and without deionized water in toluene, using the same procedures described above, and yielded electrically conductive samples.

However, 3-trimethoxysilylpropyldiethylenetriamine yielded insulated copper flakes. Figure 4.9 summarizes schematically the steps involved in the insulation process. Since the sample was subsequently cured at 120 °C, the process yielded chunky and coarse copper flake aggregates. This greatly affected the performance of the TIM derived from these materials, as will be discussed in the Results section.

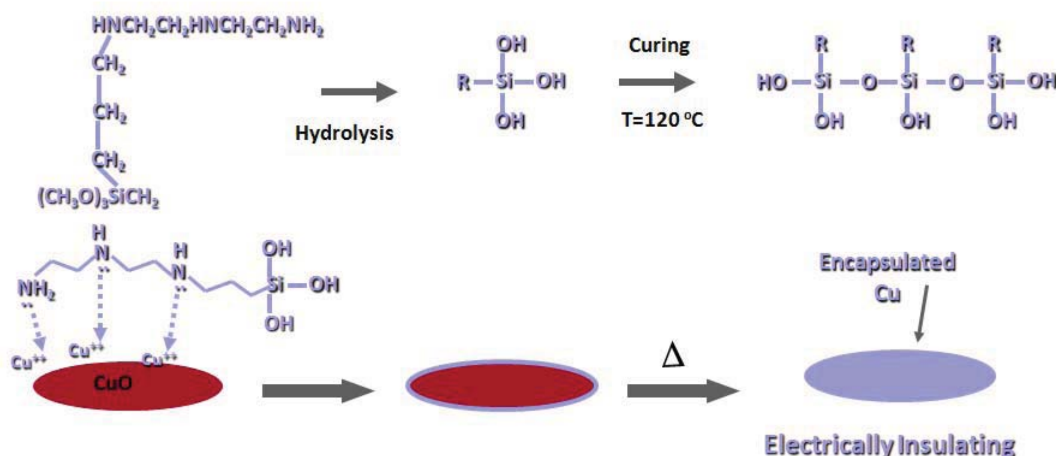


**Figure 4.9 Schematic representation of the insulation of copper flakes with silane coupling agents.**

Functionalized surface-active agents such as PEO-NH2 can bind with metallic and metallic oxide layers, thus encapsulating metallic particles such as copper flakes, and

subsequently yielding non-conducting TIM formulations. As discussed in Chapter 3, the insulation resistance measurements indicated that the copper flakes insulated with the PEO-NH2 surfactant had a resistivity orders of magnitude higher than bulk copper.

### 4.4.3 Polymeric Matrix

The different types of polymers and oligomers used in TIM formulations are listed in Table 4.3. The oligomers $E_1$, $E_2$, and F were synthesized as described in Chapter 3 as novel types of surface-binding agents potentially enhancing matrix-filler interactions. The other polymers were purchased from commercial suppliers (Aldrich).

**Table 4.3 Characteristics of matrix materials used in TIM formulations. The letters A, $B_i$, $C_i$, $D_i$, $E_i$, F, and $G_i$ identify the matrix type used.**

| **Polymers** | **Polydimethylsiloxane (PDMS), A** | **Poly(ethylene glycol) (PEG 200), $B_1$** | **Poly(ethylene glycol) (PEG 400), $B_2$** |
|---|---|---|---|
| **Oligomers** | Diethylene glycol (DiEG), **$C_1$** | Triethylene glycol (TriEG), **$D_1$** | Tetraethylene glycol (TetraEG), **$G_1$** |
| | DiEG monomethyl ether (DiEGMME), **$C_2$** | TriEG monomethyl ether (TriEGMME), **$D_2$** | TetraEG monomethyl ether (TetraEGMME), **$G_2$** |
| | DiEG Dimethyl ether (DiEGDME), **$C_3$** | TriEG Dimethyl ether (TriEGDME), **$D_3$** | TetraEG Dimethyl ether (TetraEGDME), **$G_3$** |
| | DiEG monoethyl ether (DiEGMEE), **$C_4$** | TriEG monoethyl ether (TriEGMEE), **$D_4$** | TetraEG monoethyl ether (TetraEGMEE), **$G_4$** |
| | DiEG Diethyl ether (DiEGDEE), **$C_5$** | TriEG Diethyl ether (TriEGDEE), **$D_5$** | TetraEG Diethyl ether (TetraEGDEE), **$G_5$** |
| | Amino Pentaethylene oxide (PEO5-$NH_2$), **$E_1$** | Amino Polyethylene oxide (PEO15-$NH_2$), **$E_2$** | Amino Methoxy polyethylene glycol (MPEG-$NH_2$), **F** |

## 4.5 Experimental Procedures for Measuring the Effective Thermal Conductivity

Different TIM formulations were generated by compounding one or more matrix materials (A-G in Table 4.3) with one or two types of metallic particles (entries 1-15 in Table 4.1). The type and amount of each component incorporated is specified in the sample nomenclature used. For example, $4(86)+E_1(8.4)+D_3(5.6)$ corresponds to a mixture of 86 g of 3 μm copper flakes, 8.4 g of surfactant PEO5-$NH_2$, and 5.6 g of triethyleneglycol dimethyl ether, for a total weight of 100 g.

The effective thermal conductivity of the TIM samples was measured as a function of layer thickness according to the ASTM standard D 5470 as described earlier. The LabView program interface allowed selection of the desired interface temperature, and a series of loads could be selected, however, using shims for thickness of the TIM the load was not varied and fixed at 50 PSI. Then the control system automatically sets the linear actuator to the initial load, controls the heaters to set the interface temperature (50 °C), calculates the thermal resistance, and determines steady state values (within ±0.025%) before cycling to the next load. The apparatus maintains the mean temperature of the joint within ±5% of the desired set point (50 °C), and the pressure within ±1% of the set point. Changes in joint temperature, heating rate, joint thermal conductivity, and joint thermal resistance are automatically monitored. When the ratio of the slope for the last ten recorded values for all the convergence parameters is less than 0.05%, the system determines that steady-state conditions have been reached. The cooling bath on the instrument was set at 20 °C manually as a heat sink. All relevant data (load, joint temperature, lower and upper heat flux, and joint resistance) were stored in text files which could easily be viewed after the experiment.

The applied load was set in two different ways: For the measurements with shims, the load was set at 50 PSI (0.345 MPa) throughout the measurements, and for measurements without shims, the load was set to vary from 5 to 100 PSI, at intervals of 5 PSI over 20 cycles.

The surface of the flux meters was cleaned with acetone before the measurements, and a thin layer of mineral oil was applied to the heating and cooling blocks to minimize the contact resistance. The desired amount of TIM was then placed in the center of the lower flux meter, which was placed on the heating block, and the upper flux meter was placed on top of it. For experiments with shims, the shim was placed before installing the upper flux meter. The setup was verified for proper alignment before loading. The desired joint temperature was set by controlling the heater voltage through the software.

To estimate the uncertainty on the joint resistance measurements, one needs to know the uncertainty in the parameters used (inherent in the temperature drop at the interface) and the heat flow rate calculations,[4] in other words the uncertainty on the temperature drop across the joint (0.2 $^{o}$C), and the uncertainty on the heat flow rate, $Q$. The uncertainty on $Q$ is determined by the uncertainty on the temperature gradient calculated using a least squares linear fit of the RTD temperature measurements, and was estimated as $0.5\%.$,[5] and the difference in the heat flow rates between the two flux meters due to heat loss to the surroundings. Since the mean of the upper and lower heat flow readings is used to calculate resistance, one half of a percent difference between the upper and lower flux meters was assumed for the uncertainty on $Q_{ave}$.[5] The uncertainties can be combined using the method described by Moffat[6] to calculate the uncertainty in the thermal joint resistance as[5]

$$\frac{\delta R}{R} = \left[\left(\frac{\delta \Delta T}{\Delta T}\right)^2 + \left(\frac{\delta Q}{Q}\right)^2\right]^{1/2} \quad (4.1)$$

$$\frac{\delta R}{R} = \left[\left(\frac{0.2}{\Delta T}\right)^2 + (0.005)^2 + \left(\frac{1}{2}\frac{Q_{hot} - Q_{cold}}{Q_{ave}}\right)^2\right]^{1/2}$$

The uncertatinty in heat flow rate across joint is calculated to be 2%.[7] The uncertainty in TIM thickness measurements (using the laser scan micrometer) was 0.3 %, which is much smaller than the uncertainly calculated for the thermal joint resistance (15% on average), and it can therefore be ignored in calculating the uncertainty on the effective thermal conductivity measurements. Therefore, the uncertainty on the effective thermal conductivity is the same as the uncertainty on the thermal joint resistance.

## 4.6 Results and Discussion

The results of the Coulter Counter Multisizer II analysis showed that the diameter of the particle sizes were $d_{50} = 1.69 \pm 0.19$ μm for the A & C Al powder, and $d_{50} = 2.67 \pm 0.25$ μm for the Anachemia Al powder. Table 4.4 summarizes electrical conductivity results for mixtures of copper flakes ($d_{50}$ =3 μm) with A & C aluminum powders, without any liquid binder.

**Table 4.4 Electrical characteristics of mixtures on non-conducting Al particles with conducting Cu flakes.**

| Cu weight % | Al weight % | Cu volume % | Al volume % | Electrically Conducting |
|---|---|---|---|---|
| 86 | 14 | 65 | 35 | Y |
| 83 | 17 | 60 | 40 | N |
| 80 | 20 | 55 | 45 | N |
| 77 | 23 | 50 | 50 | N |
| 50 | 50 | 23 | 77 | N |

The results for mixtures of copper flakes with the Anachemia aluminum powder were identical. When the volume fraction of the aluminum powder increased above 40%, the mixture became electrically insulated. The percolation limit of the copper particles in this particular mixture is therefore somewhere between 60 and 65% by volume.

Since Cu and Al have high intrinsic thermal conductivities (400 and 237 W/mK, respectively), we attempted to maximize the volume fraction of solid filler in the TIM formulations. However we noticed that, as the amount of the aluminum powder in the formulation was increased, the spreadability of the TIM decreased markedly due to the spherical geometry and the coarseness of the aluminum powders. Since spreadability is an important factor in applying a TIM to a surface and obtaining a thin layer, volume fractions of 77 and 23% for the aluminum powder and the copper flakes, respectively, were selected for the TIM formulations. These volume fractions correspond to 50% weight fractions for each of the fillers.

The number of TIM formulations surveyed during the project was quite large (over 150 samples). However for the sake of conciseness, only selected results will be presented here to illustrate the influence of specific parameters on the performance of the materials developed. The uncertainties on the effective thermal conductivities were estimated from the statistical error on the slope of the least square fits for plot of the thermal resistance vs. thickness of the TIM.

### 4.6.1 Commercial TIM

Arctic-Silver5 and Shin-Etsu X23-7783D are two commercial high-performance TIM compositions used as benchmark materials for comparison to the new formulations tested. While these TIM are widely used, it was hoped that we could develop TIM with higher effective thermal conductivities and/or at a lower cost. In an attempt to achieve this, the effective thermal

conductivity ($k$) and joint resistance ($R$) of TIM formulations incorporating different polymers and filler particles were compared to these commercial materials.

Figure 4.10 represents the results gathered for the commercial TIM formulations.

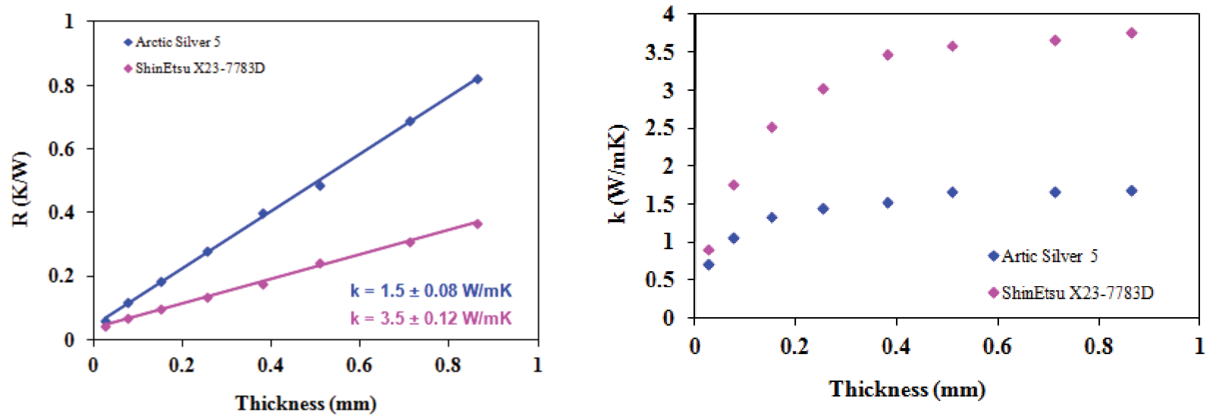


**Figure 4.10 Plots of thermal joint resistance (left) and effective thermal conductivity (right) as a function of thickness for commercial TIM compositions.**

Plots of $k$ versus $h$ (thickness) yielded effective thermal conductivity values of about 1.5 and 3.8 W/mK for Arctic-silver5 and Shin-Etsu X23-7783D, respectively. The effective thermal conductivity was almost constant for thick layers (bulk properties) but decreased for thinner layers, presumably due to significant contact resistance contributions.

### 4.6.2 Particle Encapsulation with Silanes and PEO-$NH_2$

The encapsulation of copper flakes was studied to make the fillers electrically insulated. We used silane coupling agents (to form a silicate layer on the particles) in TIM compositions, as described in Section 4.4.2 (particle encapsulation), and only one of the silane coupling agents, 3-trimethoxysilylpropyldiethylenetriamine, yielded insulated copper flakes but formed a coarse Cu powder. The Cu powder treated with this silane reagent was used in TIM formulations mixed

with Cu flakes (ID 4) and with Al powder (ID 2, small particles passing through the No. 635 testing sieve, < 20 μm). The results for different samples prepared with varying weight fractions of silane-encapsulated Cu are listed in Table 4.5 (all the samples were electrically insulating and the results were obtained without shims for these samples). We could not attain thin TIM films in the effective thermal conductivity measurements due to the presence of the coarse Cu powder, so only bulk thermal conductivities are reported. The lowest thickness achieved during each test (at an applied pressure of 100 PSI), with uncertainly of 0.3 % from the laser scan micrometer, are also listed in Table 4.5. As the amount of the encapsulated copper was increased in the TIM formulations spreadability decreased, and therefore the contact resistance rose and the effective thermal conductivity decreased.

**Table 4.5 Characteristics of TIM compositions for silane encapsulation of filler particles.**

| Sample ID | Composition | Bulk k (W/mK) | Thickness (mm) |
|---|---|---|---|
| **1** | 4(41.4)+silane encapsulated 4(4.6)+ 2(46)+ $D_3$(8) | 5.88 ± 0.16 | 0.30 |
| **2** | 4(34.5)+silane encapsulated 4(11.5)+ 2(46)+ $D_3$(8) | 3.96 ± 0.21 | 0.32 |
| **3** | 4(23)+silane encapsulated 4(23)+ 2(46)+ $D_3$(8) | 3.06 ± 0.28 | 0.40 |
| **4** | 4(11.5)+silane encapsulated 4(34.5)+ 2(46)+ $D_3$(8) | 2.00 ± 0.3 | 0.41 |

In another series of experiments, copper flakes encapsulated with different amounts of PEO5-$NH_2$ (ID $E_1$) surfactant were combined with aluminum (ID 2, particles < 20 μm) and TriEGDME (ID $D_3$) to give TIM compositions with 92-90% wt solids contents. The results for effective thermal conductivity measurements obtained without shims (with a load set to vary from 5 to 100 PSI, at intervals of 5 PSI over 20 cycles) indicate that the thermal joint resistance

obtained is lower when $PEO\text{-}NH_2$ is used as a surfactant in the TIM. Table 4.6 and Figure 4.11 summarize the results for the 100 PSI load (the detailed results for different loads are reported in Appendix 4.8).

**Table 4.6 Characteristics of TIM compositions with $PEO\text{-}NH_2$ encapsulation of the filler particles (100 PSI load).**

| Sample ID | Composition | Bulk k (W/mK) |
|---|---|---|
| **$S_1$** | $2(46)+4(46)+D_3(7.2)+E_1(0.8)$ | 3.50 ± 0.45 |
| **$S_2$** | $2(46)+4(46)+ D_3 (6.4)+E_1(1.6)$ | 4.53 ± 0.51 |
| **$S_3$** | $2(46)+4(46)+ D_3 (5.6)+E_1(2.4)$ | 5.72 ± 0.25 |
| **$S_4$** | $2(45.5)+4(45.5)+ D_3 (4.4)+E_1(3.6)$ | 6.93 ± 0.78 |
| **$S_5$** | $2(45)+4(45)+ D_3 (5)+E_1(5)$ | 7.21 ± 0.16 |
| **$S_6$** | $2(45)+4(45)+ D_3 (4)+E_1(6)$ | 9.40 ± 0.85 |

This effect is attributed to enhanced wetting of the filler surface as a result of binding of $PEO\text{-}NH_2$ with the metal oxide layer at the surface of the particles, or with the bare metallic surface. The effective thermal conductivity is highest for TIM compositions with higher $PEO\text{-}NH_2$ contents (60% by weight of the liquid components). The joint resistance also decreases as the thickness of the TIM layer decreases (applied pressure increases), which is due to improved joint contact. A thickness of 0.07 mm was achieved for samples 5 and 6, with higher surfactant concentrations. The surfactant therefore apparently enhances the spreadability of the TIM.

The effective thermal conductivities were calculated from the reciprocal of the slope in Figure 4.11.

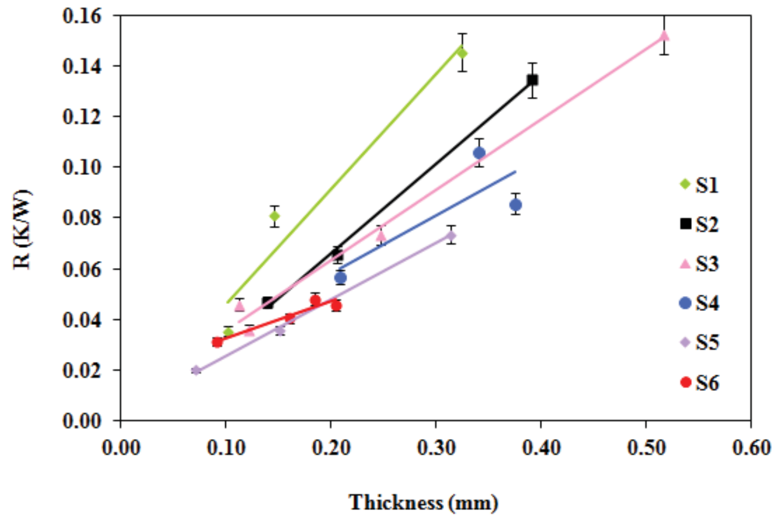


**Figure 4.11 Thermal joint resistance versus TIM thickness for the samples in Table 4.6 (100 PSI load).**

Higher effective thermal conductivities were achieved as the concentration of surfactant increased in the TIM formulations. Sample 6, containing 60 % surfactant in the liquid component, had the highest effective thermal conductivity, presumably due to the effect of the surfactant on surface wetting of the metals.

### 4.6.3 Mixtures of Particles Versus Single Components

For all the compositions incorporating two different particle types, a weight ratio of 1:1 was used for the fillers. Silver has an intrinsic thermal conductivity (429 W/mK) similar to copper (400 W/mK)[8] but the latter is much cheaper, so there is potentially no advantage in using silver in the TIM compositions. A first series of measurements was obtained for TIM compositions with weight fractions of metal fillers adjusted to provide comparable spreadabilities.

**Effect of copper flake size:** The thermal joint resistance was measured for TIM compositions containing a mixture of liquids $D_3$(5.6)+$E_1$(8.4), and a single filler component (copper flakes) varying in size from 3 to 14 μm (Figure 4.12).

These results were obtained without shims. The thermal joint resistance remained almost constant over the range of applied loads from 5 to 100 PSI, except for the largest copper flakes (ID 7, with 14 μm size), which may be due to experimental error (for instance, the surface of the flux meters may not have been fully wetted with the sample in that case). For this sample, the joint resistance decreased as the load increased (better contact between the heat flux meters and the TIM, and therefore lower contact resistance).

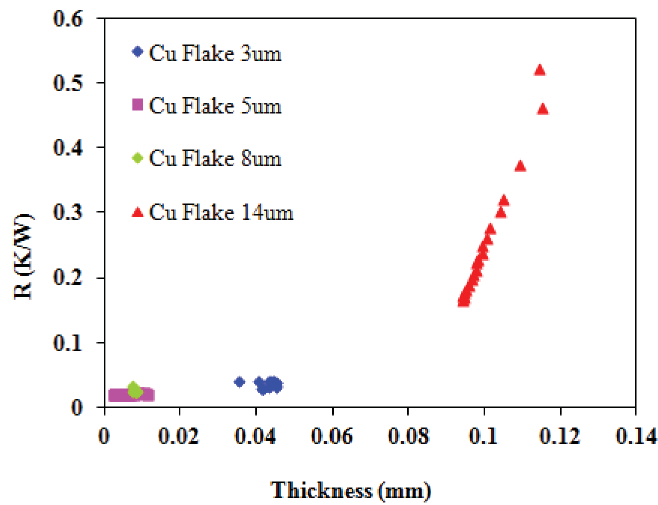


**Figure 4.12 Thermal joint resistance of TIM formulations measured without shims: blue for 4(86) + $D_3$(5.6) + $E_1$(8.4), pink for 5(86) + $D_3$(5.6) + $E_1$(8.4), green for 6(86) + $D_3$(5.6) + $E_1$(8.4), and red for 7(86) + $D_3$(5.6) + $E_1$(8.4).**

The effective thermal conductivity of these samples is reported in Table 4.7. The lowest thickness attained for sample 1 was 0.04 mm while for samples 2 and 3, with larger flake sizes, it

was even lower. This could be related to deformation of the larger flakes at high applied pressures (100 PSI). The uncertainly on the thickness measurements obtained from the laser scan micrometer was 0.3 %. For sample 4 the spreadability was poorer due to the large size of the Cu flakes (14 μm). The effective thermal conductivity of the samples did not follow any specific trend, possibly due to deformation of the flakes by increasing the applied pressure. The sample with smallest Cu flake size showed better spreadability and a lower uncertainly in effective thermal conductivity, and presumably less significant flake deformation during the test. Therefore, the Cu flakes (ID 4, 3 μm size) were selected for subsequent TIM formulations.

**Table 4.7 Characteristics of TIM compositions for different sizes of Cu flakes.**

| Sample ID | Composition | k (W/mK) | Thickness (mm) |
|---|---|---|---|
| **1** | 4(86)+$D_3$(5.6)+$E_1$(8.4) | 1.63 ± 0.08 | 0.04 |
| **2** | 5(86)+$D_3$(5.6)+$E_1$(8.4) | 1.87 ± 0.57 | 0.004 |
| **3** | 6(86)+$D_3$(5.6)+$E_1$(8.4) | 1.92 ± 0.08 | 0.008 |
| **4** | 7(86)+$D_3$(5.6)+$E_1$(8.4) | 1.1 ± 0.28 | 0.09 |

**Effect of ethylene glycol oligomers:** The effect of methyl ether end groups in the ethylene glycol oligomers used for mixtures of liquids (PEO-$NH_2$+oligomers) with a single solid filler (copper flake, ID 4) was also studied. The results are compared in Table 4.8 for triEG mono- and dimethyl ether end groups. The effective thermal conductivity of these samples is essentially identical, although the presence of the methyl ether groups affects the boiling point or volatility of the ethylene glycol component (boiling point of $D_1$=285 $^oC$, $D_2$=122 $^oC$, and $D_3$=216 $^oC$). Considering that the results are very similar, it may be preferable to select triEG for the TIM

formulations, considering its higher boiling point, to minimize loss of the oligomeric binder in high temperature operation (50 $^{o}$C and above).

**Table 4.8 The effective thermal conductivity of TIM containing copper flakes with different oligomeric binders.**

| Composition | k (W/mK) |
|---|---|
| 4(86)+$D_1$(5.6)+$E_1$(8.4) | 1.59±0.15 |
| 4(86)+$D_2$(5.6)+$E_1$(8.4) | 1.72±0.11 |
| 4(86)+$D_3$(5.6)+$E_1$(8.4) | 1.63±0.08 |

**Effect of filler shape:** The effect of spherical particles (Al powder, ID 2) was also studied for TIM compositions incorporating PDMS (ID A) and copper flakes (ID 4) with and without aluminum. In Figure 4.13, the thermal joint resistance of three samples is compared versus TIM thickness.

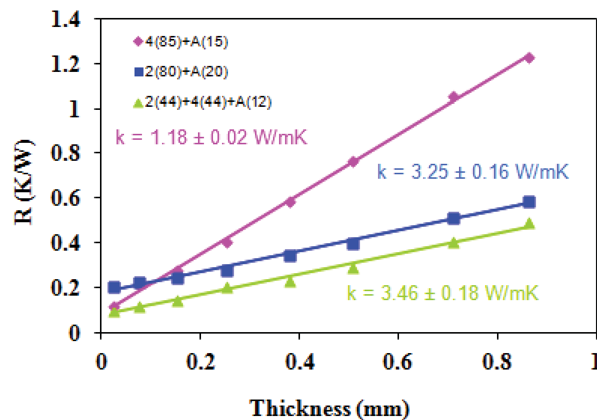


**Figure 4.13 Thermal joint resistance versus TIM thickness, pink for 4(85) + A(15), blue for 2(80) + A(20), and green for 2(44) + 4(44) + A(12).**

The weight fractions were adjusted for constant viscosity. The results were obtained for measurements with shims at a constant load of 50 PSI.

**Effect of single component and mixed fillers:** The presence of aluminum particles (mixture of large and small Al particles + small Cu flakes) in the TIM clearly decreases the thermal joint resistance and enhances the effective thermal conductivity, due to the increased volume fraction of metallic fillers. Since Cu flakes have a high intrinsic thermal conductivity, the effective thermal conductivity of the TIM increases. To maintain TIM spreadability, it was possible to attain higher solids contents with mixtures of Al and Cu fillers than with Al alone. This can be explained by the fact that the density of aluminum (2.7 g/mL) is much lower than copper (8.96 g/mL), so that the fraction of the total volume occupied by the Al filler is higher. In these mixtures, the gaps between the large spherical Al particles are therefore filled by the smaller Cu flakes, which have a high intrinsic thermal conductivity. The heat flows more readily through the high conductivity metallic domains under these conditions.

Since a lower thermal joint resistance and better spreadability were achieved for TIM compositions with larger amounts of surfactant, the composition of the liquids binder was set to 40% TriEGDME and 60% PEO-$NH_2$ in the following measurements.

**Effect of surfactant (one filler type):** The following measurements were performed using a single metallic filler with a constant weight fraction (86% w/w), and only one polymer in the TIM formulations. The results (**Error! Reference source not found.**) obtained for the copper flakes with two different PEO-$NH_2$ oligomers, PEO5-$NH_2$ ($DP_n$ = 5) and PEO15-$NH_2$ ($DP_n$ = 15), and PDMS (100 cSt, ID A) show that the shorter chain compound gives a higher $k$ value.

This difference may be related to the thinner insulating layer formed around the metallic

This difference may be related to the thinner insulating layer formed around the metallic particles by the shorter oligomer chains. The lowest sample thickness (0.006 mm) was reached for both samples containing PEO-$NH_2$, while the lowest thickness for the sample containing PDMS was 0.015 mm.

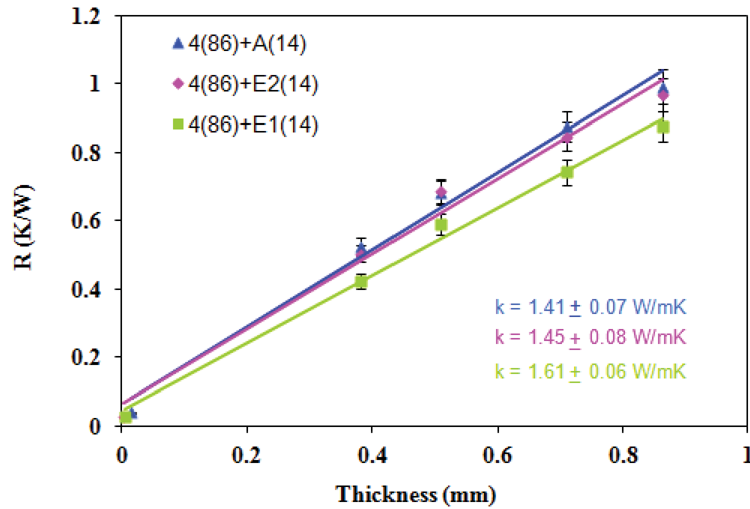


**Figure 4.14 Thermal joint resistance of TIM compositions: blue for 4(86) + A(14), pink for 4(86) + E2(14), green for 4(86) + E1(14).**

**Effect of surfactant (binary filler mixtures):** In Figure 4.15, the influence of the PEO-$NH_2$ segment size in the surfactant used ($DP_n$= 5 and 15) was examined for two TIM compositions containing aluminum powder (ID 2), copper flakes (ID 4) and TriEGDME (ID $D_3$) and PEO-$NH_2$ (ID $E_1$, $E_2$). These results were obtained without shims. The thickness of the TIM layer decreased as the applied load was increased in this case.

Thinner layers were achieved for the shorter chain surfactant, presumably due to better spreadability of the TIM. The effective thermal conductivity of the materials, calculated from the slope of graphs of R vs. h yielded comparable k values within error limits. These do not

correspond to the bulk thermal conductivity of the TIM, as the layer thickness was low. The bulk thermal conductivity is defined for thick layers, and remains constant for higher thicknesses. For example in Figure 4.10 (the plot of effective thermal conductivity versus thickness), the plateau in the plot indicates the bulk thermal conductivity of the sample.

Unfortunately, the aluminum powders are difficult to obtain in Canada, due to export restrictions in the US. Consequently, subsequent research focused on copper flakes as metallic fillers. In addition, it was observed that the exclusive use of copper flakes is desirable in terms of achieving good spreadability for TIM compositions with high solid contents.

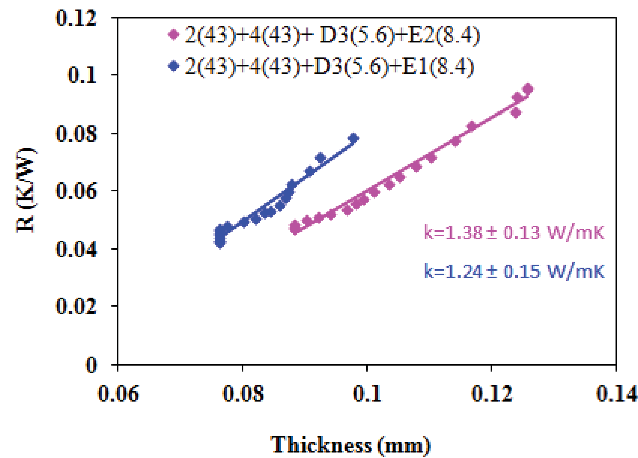


**Figure 4.15 Thermal joint resistance versus TIM thickness, pink for 2(43) + 4(43) + $D_3$(5.6) + $E_2$(8.4), blue for 2(43) + 4(43) + $D_3$(5.6) + $E_1$(8.4).**

**Effect of liquid binder:** The influence of the liquid binder on the effective thermal conductivity of TIM composition with a single component (copper flakes, ID 4) was studied. The results for the effective thermal conductivity are listed in Table 4.9

**Table 4.9 The effective thermal conductivity of TIM containing copper flakes with different liquid binders.**

| Composites | k (W/mK) |
|---|---|
| 4(86)+A(14) | 1.41 ± 0.07 |
| 4(86)+$E_2$(14) | 1.45 ± 0.08 |
| 4(86)+F(14) | 1.44 ± 0.14 |
| 4(86)+$B_1$(14) | 1.56 ± 0.09 |
| 4(86)+$B_2$(14) | 1.58 ± 0.07 |
| 4(86)+$E_1$(14) | 1.61 ± 0.06 |

The resulting effective thermal conductivities are relatively close for all the samples, the TIM with PDMS and PEO-$NH_2$ ($DP_n$ = 5) having the lowest and the highest effective thermal conductivities, respectively. The TIM with MPEG-$NH_2$ oligomer also showed poorer spreadability than the one with PEO-$NH_2$.

**Effect of filler weight fraction:** The weight fraction of the metallic particles in the TIM formulations plays an important role in the performance of these materials, but also influences their spreadability. The TIM samples were prepared with copper flakes (ID 4), TriEGDME (ID $D_3$), and PEO-$NH_2$ ($E_2$) where the copper flakes weight fractions varied (82, 84 and 86% w/w) in very thin (4-14 μm) TIM layers. The results obtained are shown in Figure 4.16. These results were obtained without shims for a load range of 5 – 100 PSI. It is clear that thinner layers (0.004 mm) were achieved for the 82% and 84% samples due to their better spreadability (higher liquid portion).

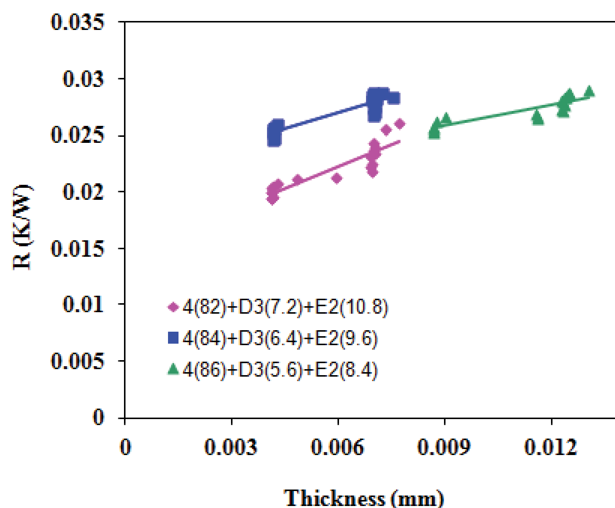


**Figure 4.16 Thermal joint resistance versus TIM thickness, pink for 4(82) + $D_3$(7.2) + $E_2$(10.8), blue for 4(84) + $D_3$(6.4) + $E_2$(9.6), and green for 4(86) + $D_3$(5.6) + $E_2$(8.4).**

The results also show that while the same layer thickness was achieved for the 82 % and 84 % solid samples, the joint resistance was lower for the 82 % sample. A higher liquid portion in the TIM formulation with 82 % solids may help to fill air gaps at the surfaces and decrease the joint resistance and the contact resistance. The effective thermal conductivity values, obtained from the inverse of the slope for these TIM, are listed in Table 4.10

**Table 4.10 The effective thermal conductivity of TIM containing Cu flakes, TriEGDME, and PEO15-$NH_2$ for thin layers.**

| Composition | k (W/mK) |
|---|---|
| 4(82)+$D_3$(7.2)+$E_2$(10.8) | 1.24 ± 0.08 |
| 4(84)+$D_3$(6.4)+$E_2$(9.6) | 1.69 ± 0.05 |
| 4(86)+$D_3$(5.6)+$E_2$(8.4) | 2.53 ± 0.11 |

**Effect of surfactant (MPEG-$NH_2$):** The joint resistance for TIM compositions containing MPEG-$NH_2$ (ID F) is compared in Table 4.11 for TIM composition containing copper flake (ID 4) and aluminum powder (ID 2) fillers. The samples containing Al particles have a large standard deviation, since the Al particles are spherical coarse powders and decrease the spreadability of the TIM (leading to a higher contact resistance). The effective thermal conductivity of the TIM decreases due to the presence of an alumina layer on the Al particles, which interrupts the heat flow path in the TIM. The samples incorporating only copper flakes have a better performance (spreadability), and a higher effective thermal conductivity due to the presence of the surfactant, the encapsulation of the Cu flakes, and the higher intrinsic thermal conductivity of copper. It was also possible to achieve lower layer thicknesses while measuring the effective thermal conductivity in these systems.

**Table 4.11 The effective thermal conductivity of TIM containing MPEG-$NH_2$.**

| Composition | k (W/mK) |
|---|---|
| 4(86)+F(14) | 1.44 ± 0.14 |
| 4(86)+$D_3$(5.6)+F(8.4) | 1.36 ± 0.23 |
| 2(43)+4(43)+$D_3$(5.6)+F(8.4) | 1.11 ± 0.19 |
| 2(86)+$D_3$(5.6)+F(8.4) | 0.96 ± 0.28 |

Finally, the performance of two samples (4(82)+$E_1$(18) and 4(84)+$E_1$(16)) is compared to that of the commercial TIM formulations in Figure 4.17. The solids content of the samples was adjusted such that their viscosity was similar to that of the commercial TIM preparations (Shin Etsu X23-7783D and Arctic Silver5), although Arctic Silver showed less consistency for holding

together after spreading it (the liquid component was squeezed out when the pressure was applied on the sample). Thinner layers and joint resistance values, comparable to or lower than for the commercial materials, were achieved with our samples. In addition, the range of thicknesses achieved only varied slightly with the applied load for our samples, in contrast to the commercial TIM samples. The contact resistance of the commercial TIM samples extrapolates to a negative resistance, which is not reasonable. This is presumably due to the better spreadability of our samples as compared to the commercial TIM samples.

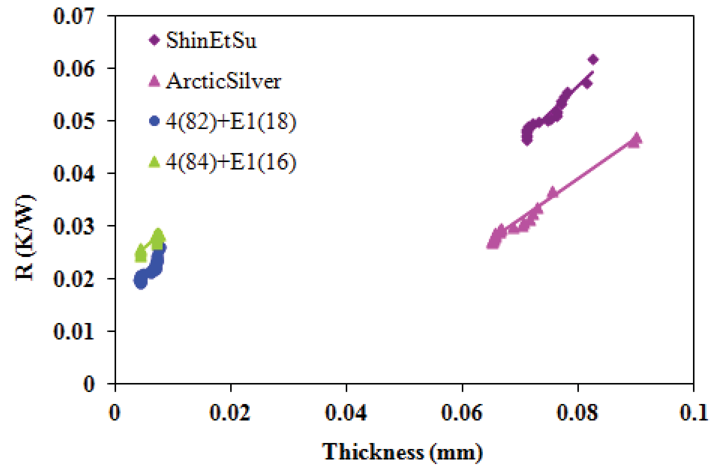


**Figure 4.17 Thermal joint resistance variation with TIM layer thickness: Purple for Shin Etsu X23-7783D, pink for Arctic Silver5, blue for 4(82) + $E_1$(18), and green for 4(84) + $E_1$(16).**

The commercial TIM and our samples were also tested as thin films at a constant load of 50 PSI, and the results obtained are summarized in Table 4.12. The PEO-$NH_2$ surfactant led to improved spreadability and consistency for thin TIM layers (minimum thickness of 0.004 mm achieved vs. 0.06 mm for the commercial TIM).

**Table 4.12 The effective thermal conductivity of TIM for thin layers.**

| Composition | k (W/mK) | Thickness (mm) |
|---|---|---|
| 4(82)+$E_1$(18) | 1.24 ± 0.08 | 0.004 |
| 4(84)+$E_1$(16) | 1.69 ± 0.05 | 0.004 |
| Shin-Etsu | 0.77 ± 0.01 | 0.071 |
| Arctic Silver 5 | 1.04 ± 0.01 | 0.065 |

## 4.7 Conclusions

TIM compositions with effective thermal conductivities up to 9.4 W/mK have been obtained through systematic formulation optimization. The influence of different parameters including the geometry and the volume fraction of the fillers, and surface wetting on the performance of these materials has been explored. Optimal results have been obtained for TIM compositions incorporating copper flakes dispersed in an oligo(ethylene glycol) – amino oligo(ethylene oxide) surfactant mixture (PEO-$NH_2$). These surfactants were shown to bind to the surface of the copper filler particles in XPS and contact angle measurements (Chapter 3), which explains the increased effective thermal conductivity observed for these mixtures. The weight fraction of metallic fillers in the TIM impacts spreadability, thus the weight fraction was set to 86% to give a workable and paste-like consistency, providing thin TIM layers with a low thermal joint resistance. The amine-terminated surfactant essentially insulates the TIM and enhances the effective thermal conductivity of the TIM. Thin layers (down to 0.004 mm) were achieved for TIM compositions containing surfactant and copper flakes as compared to commercial TIM formulations (0.07 mm), in addition to higher effective thermal conductivities. The results of the effective thermal conductivity measurements were used for mathematical modeling, to predict the effect of the

surfactant in the TIM formulations as well as the geometry of particles. This will be discussed in Chapter 5.

## 4.8 Appendix: Bulk Thermal Conductivity versus Load

The experiments reported in Table 4.6 were performed for different loads 5-100 PSI (5 PSI intervals for 20 cycles). The effective thermal conductivities, obtained from the inverse of the slope for each load, are listed in

Table 4.13.

**Table 4.13 The effective thermal conductivity of TIM for different applied loads.**

| Loads (PSI) | *k* (W/mK) $S_1$ | *k* (W/mK) $S_2$ | *k* (W/mK) $S_3$ | *k* (W/mK) $S_4$ | *k* (W/mK) $S_5$ | *k* (W/mK) $S_6$ |
|---|---|---|---|---|---|---|
| 5 | 3.82 | 4.01 | 5.49 | 5.79 | 6.06 | 9.00 |
| 10 | 3.65 | 4.04 | 5.56 | 5.75 | 5.97 | 8.43 |
| 15 | 3.67 | 4.04 | 5.53 | 5.51 | 5.95 | 8.60 |
| 20 | 3.66 | 3.96 | 5.46 | 5.30 | 6.04 | 8.75 |
| 25 | 3.69 | 4.01 | 5.39 | 5.12 | 6.22 | 8.41 |
| 30 | 3.56 | 3.99 | 5.39 | 5.13 | 6.24 | 9.43 |
| 35 | 3.48 | 4.03 | 5.10 | 5.65 | 6.25 | 8.98 |
| 40 | 3.47 | 4.05 | 5.70 | 5.51 | 6.28 | 10.03 |
| 45 | 3.50 | 4.10 | 5.69 | 5.27 | 6.58 | 10.20 |
| 50 | 3.47 | 4.10 | 5.79 | 5.34 | 6.60 | 10.82 |
| 55 | 3.48 | 4.09 | 5.75 | 5.43 | 6.64 | 10.22 |
| 60 | 3.57 | 4.12 | 5.41 | 5.47 | 6.70 | 10.90 |
| 65 | 3.57 | 4.24 | 5.43 | 5.59 | 6.84 | 11.60 |
| 70 | 3.53 | 4.31 | 5.68 | 5.75 | 6.83 | 9.93 |
| 75 | 3.44 | 4.37 | 5.61 | 6.38 | 6.85 | 10.87 |
| 80 | 3.47 | 4.47 | 5.64 | 6.52 | 6.94 | 10.44 |
| 85 | 3.42 | 4.54 | 5.41 | 6.68 | 7.04 | 10.82 |
| 90 | 3.43 | 4.53 | 5.53 | 6.77 | 7.19 | 10.52 |
| 95 | 3.51 | 4.55 | 5.60 | 6.79 | 7.34 | 9.40 |
| 100 | 3.51 | 4.53 | 5.72 | 6.93 | 7.21 | 9.40 |

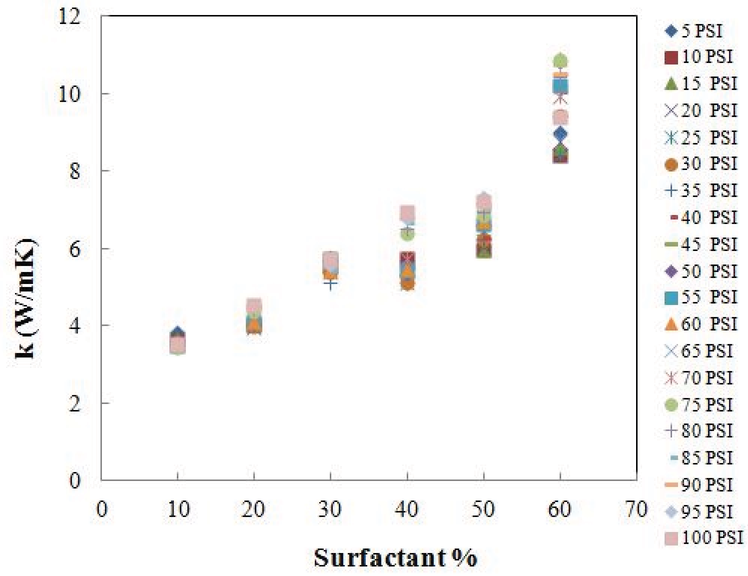


**Figure 4.18 The effective thermal conductivity of TIM vs. surfactant percentage for different applied loads 5-100 PSI.**

# Chapter 5

## Mathematical Modeling of Thermal Interface Materials (TIM)

## 5.1 Overview

The thermal conductivity of thermal interface materials (TIM) depends on various factors including the choice of filler and matrix, the filler geometry, the fraction of each component, and surface wetting (the presence of surfactants). By exploring these different factors, we have experimentally demonstrated that incorporating copper flakes dispersed in an oligo(ethylene glycol) – amino oligo(ethylene oxide) surfactant mixture (PEO-$NH_2$) gives optimal thermal conductivity for TIM compositions. We observed that these surfactants bind on the surface of the copper filler particles, resulting in increased thermal conductivity. To date, a number of theoretical approaches have been developed for predicting the effective thermal conductivity of these composites. In the present chapter, a computational approach based on the random resistor networks (RRN) method was applied to study the effective thermal conductivity of the TIM. We present results for the effect of the size distribution (mono- and polydispersed ) and geometry (particles and flakes, as well as their combination) of metallic fillers on the effective thermal conductivity of the TIM. To study the effects of surfactants on the effective thermal conductivity of the composites, we assumed that the effective thermal conductivity of the filler particles (and/or matrix) depend on the percentage of the surfactant and defined "surfactant concentration-dependent thermal conductivities". The results for different combinations of filler particles, matrix, and surfactant are compared with the experimental data.

## 5.2 Introduction

Thermal interface materials (TIM), containing a base matrix like oligo(ethylene glycol) and added metallic fillers, such as aluminum particles, are adopted in electronics packaging to facilitate heat dissipation across points of contact between parts. The theoretical prediction of the

thermal conductivity of a TIM, and other composite materials, has been the subject of numerous investigations over the last few decades. This is mainly due to their important applications in a wide range of areas of science and engineering. Widely used analytical approaches include Maxwell's[1] and Bruggeman's equations,[2] as well as their modified versions.[3,4] Examples of numerical methods include the Nielsen model[5] and the percolation model[6] (see Chapter 2). Although some of these analytical or numerical methods show reasonable agreement with the experimental data for low filler volume fractions, the results of these methods do not agree satisfactorily when the filler volume fraction is high.

A random resistor network (RRN) is a simple model for an inhomogeneous conductor.[7] This method has been recently used to numerically estimate the effective thermal conductivity of composite materials.[8] The main advantages of this model are its ability to account for high volume fractions of particles, particle geometry, size distributions, and the presence of surfactants.

In this chapter we first review the RRN method, and then present the details of the numerical algorithm used. Next, we examine the effects of the size distribution and the geometry of metallic fillers on the effective thermal conductivity of the TIM. The results are compared with the available experimental data. Finally, we present and discuss the results for surfactant concentration-dependent thermal conductivities.

## 5.3 Random Resistor Network Method

The random resistor network (RRN) method uses the analogy between the thermal and electrical conductivity of composites to estimate the effective thermal conductivity of composite materials. In an electrical network, the current $I_{ij}$ in a bond $ij$ is given by $I_{ij} = g_{ij}(V_i - V_j)$, where $g_{ij}$ is

the bond conductance (Figure 5.1), and $V_i$ and $V_j$ are the voltages at sites $i$ and $j$. The current conservation equation at each node ($i$) in the network (Kirchhoff's law) gives

$$\sum_j I_{ij} = \sum_j g_{ij}(V_i - V_j) = 0 \tag{5.1}$$

where the sum is over all the neighbouring sites (sites $j$ connected to site $i$ through a bond).

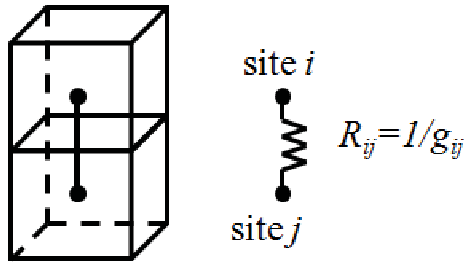


**Figure 5.1 The center of the matrix or filler is replaced by a node (site) in the lattice. The electrical resistance between neighbouring nodes is represented by a resistor.**

The voltages at the top and the bottom boundaries are given as $V_t$ and $V_b$ (a fixed voltage difference between the top and bottom layers in one direction and periodic boundary conditions in other directions). The conductance of the bonds is selected from a probability distribution function that represents the conductance distribution of the material based upon a fixed volume fraction of filler. Equation (5.1) must be satisfied at every node of the network, resulting in a set of simultaneous equations for the voltages (i.e. for a given distribution of conductances). This set of equations can be solved to obtain the voltage distribution in the network. The effective electrical conductivity is then calculated by applying Ohm’s law across the material,

$$g_e^{(S)} = \frac{\overbrace{(I/A)}^{J}}{\underbrace{(\Delta V/h)}_{E}} = \frac{h}{A} \frac{\overbrace{\sum_i \sum_j g_{ij,t} \Delta V_{ij,t}}^{\text{total current flow in the top layer}}}{\underbrace{(V_t - V_b)}_{G=I/\Delta V \text{ (conductance)}}} \tag{5.2}$$

Then, taking the average over the random realizations, we obtain $g_e = < g_e^{(S)} >$, where $g_e^{(S)}$ is the effective electrical conductivity for realization $S$.

Similarly, for the effective thermal conductivity, we have

$$\sum_j Q_{ij} = \sum_j \sigma_{ij} (T_i - T_j) = 0 \tag{5.3}$$

where $\sigma_{ij}$, i.e. the thermal conductance of a bond, is selected from a probability density function (which describes the conductance distribution of the material for the given volume fraction of filler). Similarly to the previous case the boundary conditions are given by the temperatures $T_t$ and $T_b$ at the top and bottom layers, respectively, with the *z*-axis running perpendicularly through the top and bottom faces of the material, and periodic boundary conditions in the *x*- and *y*-directions. The solution to the set of equations gives the temperature distribution in the network, from which the effective thermal conductivity can be calculated in analogy to Ohm's law, Equation (5.2),

$$k_e^{(S)} = \frac{(Q/A)}{(\Delta T/h)} = \frac{h}{A} \underbrace{\frac{\sum_i \sum_j \sigma_{ij,t} \Delta T_{ij,t}}{T_t - T_b}}_{\Sigma = \frac{Q}{\Delta T} \text{(conductance)}} \tag{5.4}$$

Again, taking the average over the random realizations gives $k_e = < k_e^{(S)} >$, where $k_e^{(S)}$ is the effective thermal conductivity for realization $S$.

The conductance $\sigma_{ij}$ between two adjacent nodes can be classified as: (1) the thermal conductance between two adjacent particles, (2) the thermal conductance between two adjacent matrix materials, and (3) the thermal conductance between a particle and its neighbouring

matrix; i.e. $\sigma_{pp}$, $\sigma_{mm}$, and $\sigma_{pm}$, respectively; see Figure 5.2. For the first two cases, the thermal particle-particle and matrix-matrix conductance are considered to be the thermal conductance of the particle and the matrix themselves, respectively. We then use the approximation $\sigma_i = k_i A_{\text{cube}}/h_{\text{cube}} = k_i r$, where $r$ is the lattice space (Figure 5.2), to obtain the conductance from the conductivity of the particles ($k_p$) or the matrix ($k_m$). The thermal particle-matrix conductance is obtained from $\sigma_{pm} = 2\sigma_p\sigma_m/(\sigma_p+\sigma_m)$; note that $R_{pm} = (R_p + R_m)/2$.

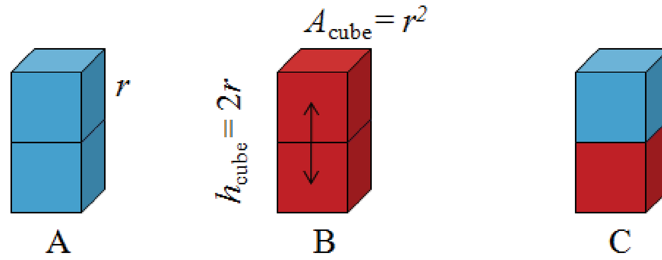


**Figure 5.2 Possible adjacent nodes in the lattice: (A) particle-particle, (B) matrix-matrix, and (C) particle-matrix (red: matrix, blue: metal).**

## 5.4 Numerical Algorithm

### 5.4.1 Generation of the Random Resistor Network

A Matlab code was developed based on the random resistor network method.[7,9] The network is constructed of equally sized cubes, arranged in an $N_1 \times N_2 \times N_3$ array. In the first step of the algorithm, the cubes are randomly assigned to be either matrix or particle in such a way as to reproduce the given volume fraction $\varphi$ of filler. In the simulations we fix the size of the lattice ($h$, thickness of the TIM layer), thus the dimension of the cubes are $r = h/(N_3 - 1)$ and the area

of the lattice is $A = r^2 N_1 N_2$. As the resolution of the lattice is varied ($N_1 = N_2 = N_3$), the dimensions of the cubes and the area of the lattice change. Figure 5.3 shows a sample structure of a random resistor network for $N_1 = N_2 = N_3 = 20$, where the top and bottom layers are fixed to be particles (simulation times are reported in Appendix 5.9).

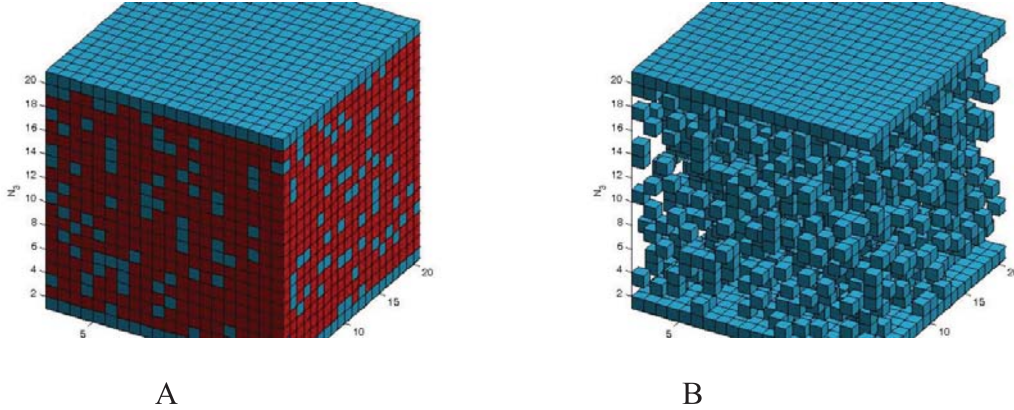

A B

**Figure 5.3 A sample structure for a random resistor network. (A) Monodispersed Al particles (volume fraction $\varphi_{Al} = 0.2$), lattice size $N_1 = N_2 = N_3 = 20$, $h_{\mathrm{TIM}} = 150$ μm and $r \approx 8$ μm (red: polymeric matrix, blue: Al particles). (B) As in panel A, but the polymeric matrix was removed for clarity.**

The polydispersed size distribution of the particles was taken into account by considering a random combination of small and large solid fillers that preserves the overall volume fraction of the solid fillers. According to our Al particles analysis results reported in Chapter 4, we can approximately divide the Al particles into two particles sizes, as shown in Figure 4.5. Numerically, we assign cubes to the smaller particles and boxes of $3 \times 3 \times 3$ (containing 27 cubes) to the large particles. In Figure 5.4, a sample structure for two sizes of solid fillers is presented for a lattice size $N_1 = N_2 = N_3 = 20$, corresponding to particle diameters of about 8

μm and 24 μm for the small and large particles, respectively. Note that, for comparison with the experimental data, we used a lattice size $N_1 = N_2 = N_3 = 50$, corresponding to cubes with a size of about 3 μm.

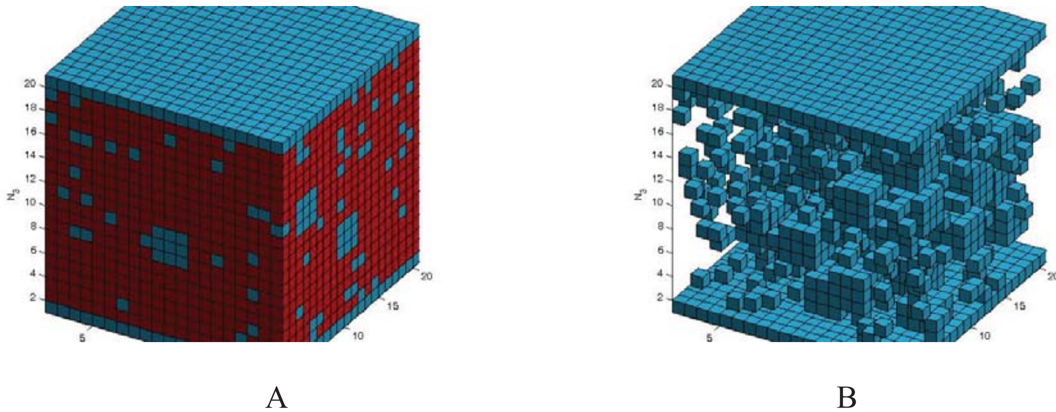

A B

**Figure 5.4 A sample structure for a random resistor network: (A) Polydispersed Al particles (input $\varphi_{Al} = 0.08$ and output $\varphi_{Al} = 0.21$), $N_1 = N_2 = N_3 = 20$ (red: matrix, blue: Al particles). The large particles occupy $3 \times 3 \times 3$ lattice sites, while smaller particles are $1 \times 1 \times 1$. (B) As in panel A, but with the background matrix removed for clarity.**

Given that copper flakes are closer to two dimensional (rectangular) objects, we assigned a rectangle of $3 \times 2$ cubes for each flake. The copper flakes can randomly take horizontal or vertical orientations. A sample structure of such a network is presented in Figure 5.5, where we used a lattice size $N_1 = N_2 = N_3 = 20$.

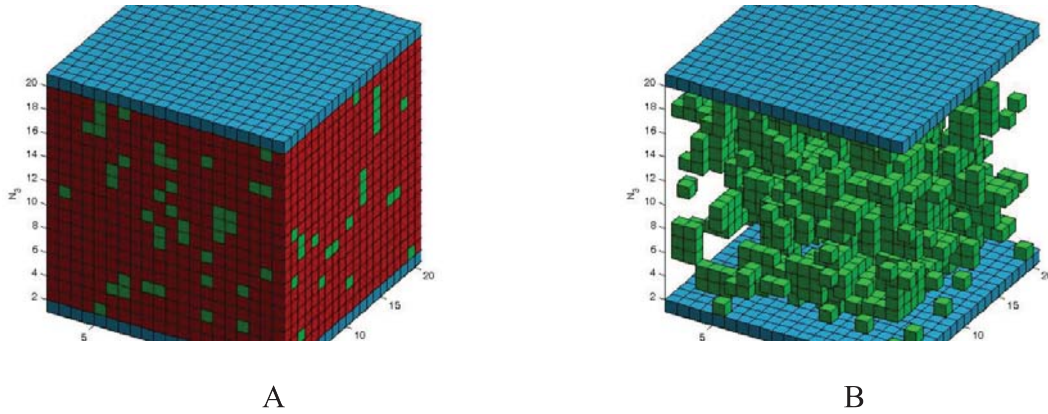

A B

**Figure 5.5 A sample structure for a random resistor network: (A) Copper flakes (input $\varphi_{Cu} = 0.05$ and output $\varphi_{Cu} = 0.21$), $N_1 = N_2 = N_3 = 20$ (red: matrix, green: copper flakes). (B) As in panel A, but with the background matrix removed for clarity.**

We also considered a combination of small and/or large Al particles with the copper flakes as fillers (Figure 5.6). A corresponding bond thermal conductance was assigned to each configuration of the network. In all simulations, the boundary conditions (temperature) were selected to be 70 $^{o}$C and 20 $^{o}$C at the top and the bottom layers, respectively, with the *z*-axis aligned with the temperature gradient (and periodic boundary conditions in *x*- and *y*-directions). The effective thermal conductivity was calculated from the resulting temperature distribution in the network according to Equation (5.4). In the next section, the code will be used to determine the effective conductivity of the composites for monodispersed and polydispersed Al particles and copper flakes.

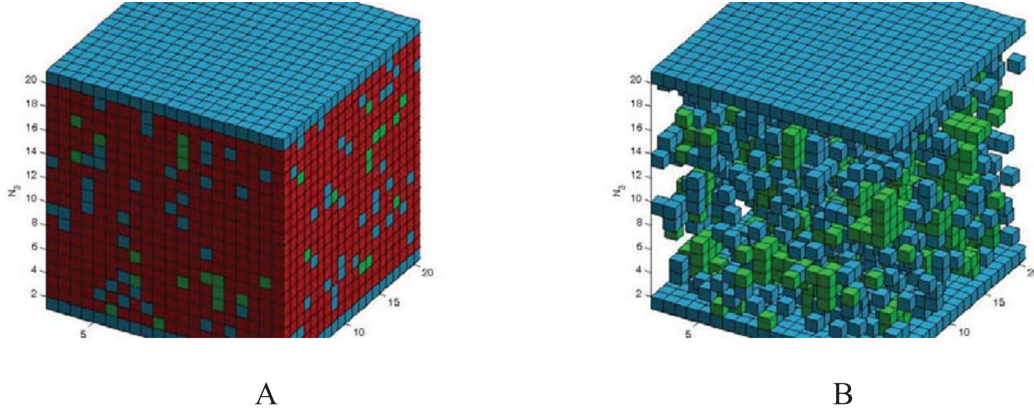

A B

**Figure 5.6 A sample structure for a random resistor network: (A) Copper flakes (input $\varphi_{Cu} = 0.024$ and output $\varphi_{Cu} = 0.081$), and monodispersed Al particles ($\varphi_{Al} = 0.116$), $N_1 = N_2 = N_3 = 20$ (red: matrix, blue: Al particles, and green: copper flakes). (B) As in panel A, but with the background matrix removed for clarity.**

### 5.4.2 Generating Simultaneous Equations (Calculating Effective Thermal Conductivity)

After generating the random resistor network, the simultaneous equations for the voltage (Equation (5.3)) can be described in a matrix form as

$$\mathrm{A}X = B \tag{5.5}$$

where A is a $N_1N_2(N_3-2) \times N_1N_2(N_3-2)$ matrix that is a function of bond conductances, and $B$ is a $N_1N_2(N_3-2)$ vector containing the temperatures at the top and bottom layers. The vector $X$ represents the temperature distribution of the network. After generating the matrix A and the vector $B$, the temperature distribution can be obtained as

$$X = \mathrm{A}^{-1}B \tag{5.6}$$

This vector can be simply reshaped (using the Matlab command "reshape") in a $N_1N_2(N_2-2) \times N_1N_2(N_3-2)$ matrix form. Then, the effective thermal conductivity can be calculated from Equation (5.4).

### 5.4.3 Effect of Boundaries

The top and bottom layers (boundaries) of the network were selected to be (i) randomly particle or matrix (from the same distribution used for the rest of the network) or (ii) particles. The effect of boundaries can be eliminated by proper selection of the lattice size. This means that if the network is large enough, then whatever species occupy the top and bottom layers will not change the effective thermal conductivity of the network. When we compared the results of the experimental data for effective thermal conductivity with the simulations results, we used a lattice size $N_1 = N_2 = N_3 = 50$ to eliminate the boundary effect (see Figure 5.11).

The simulation considers the thermal conductance from the center of the top layer to the center of the bottom layer, which means that it ignores the half layer of the top and bottom layers. This has been illustrated for a one dimensional network in Figure 5.7. However, we can include the contribution of these half layers using resistors in series. If we assume that the top and bottom layers are fixed to be particles, we obtain (Figure 5.7) $R_{\mathrm{eff}}^{\mathrm{c}} = R_1 + R_{\mathrm{eff}} + R_2$ or

$$\frac{1}{\sigma_{\mathrm{eff}}^{\mathrm{c}}} = \frac{1}{\sigma_1} + \frac{1}{\sigma_{\mathrm{eff}}} + \frac{1}{\sigma_2} \tag{5.7}$$

The corrected effective thermal conductivity, $k_{\mathrm{eff}}^{\mathrm{c}}$ , is then given by

$$\frac{h}{Ak_{\mathrm{eff}}^{\mathrm{c}}} = \frac{(r/2)}{Ak_p} + \frac{(h-r)}{Ak_{\mathrm{eff}}} + \frac{(r/2)}{Ak_p} \tag{5.8}$$

where $k_{\mathrm{eff}}$ is the effective thermal conductivity obtained from simulations without considering the half layers. The thickness and area of the lattice (TIM) are $h$ and $A$, respectively; $r$ is the lattice space, and $k_p$ is the thermal conductivity of particles. This can be rewritten as

$$k_{\mathrm{eff}}^{\mathrm{c}} = \frac{hk_{\mathrm{p}}k_{\mathrm{eff}}}{(hk_{\mathrm{p}} + rk_{\mathrm{eff}} - rk_{\mathrm{p}})} \tag{5.9}$$

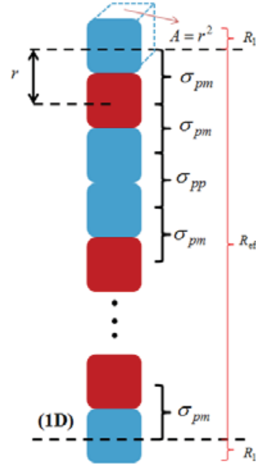


**Figure 5.7 One dimensional representation of the network (red: matrix, blue: metallic fillers).**

For a lattice size of $N_1 = N_2 = N_3 = 50$, $r \ll h$ and the Equation (5.9) approximately reduces to $k_{\text{eff}}^{\text{c}} \approx k_{\text{eff}}$.

## 5.5 Validation of the Matlab Code

We used several tests to validate the performance of the Matlab code. First, we considered a homogeneous network. In this case, all cells (cubes) are the same type of material, for example Al particles, and hence the effective thermal conductivity of the network should be equal to the effective thermal conductivity of the Al particles (dominated by the alumina layer), i.e. $k_{\text{p}} = 29$ W/mK. We performed numerical simulations for a $N_1 \times N_2 \times N_3$ lattice, choosing different values for $N_1$, $N_2$ and $N_3$ where all the cells (including boundaries) are particles. We confirmed the expected result of $k_{\text{eff}} = k_{\text{p}} = 29$ W/mK from the simulations. Similar confirmation was obtained for the effective thermal conductivity when we considered all the cells (including boundaries) to be the matrix, $k_{\text{eff}} = k_{\text{m}} = 0.158$ W/mK measured for oligo(ethylene glycol).

Next, we considered a one dimensional network ($1 \times 1 \times N_3$). If we fix the boundary of the network at the top and bottom layers to be particles, and the cells between these layers are randomly chosen to be either polymeric matrix or fillers, then the thermal conductivity of the system is the average thermal conductivity of all possible configurations. For example, for $N_3 = 3$ there are only two possible cases, with either a particle or a matrix in the middle, as shown in Figure 5.8.

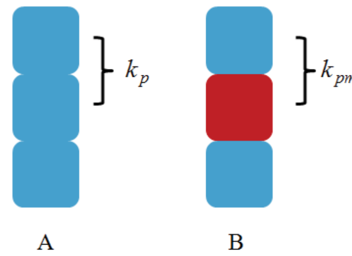


**Figure 5.8 Possible cases for the random network $1 \times 1 \times N_3$, if top and bottom layers are fixed to be particles (red: matrix, blue: metal).**

In this case, the effective thermal conductivity of the network is either ${k_{\mathrm{eff}}}^{(1)} = k_{\mathrm{p}}$, or ${k_{\mathrm{eff}}}^{(2)} = k_{\mathrm{pm}} = 2k_{\mathrm{p}}k_{\mathrm{m}}/(k_{\mathrm{p}} + k_{\mathrm{m}})$, where ${k_{\mathrm{eff}}}^{(1)}$ and ${k_{\mathrm{eff}}}^{(2)}$ are the effective thermal conductivity for realizations 1 and 2, respectively. If we choose the volume fraction of the filler to be $\varphi = 0.5$, the effective thermal conductivity of the network is $k_{\mathrm{eff}} = \left({k_{\mathrm{eff}}}^{(1)} + {k_{\mathrm{eff}}}^{(2)}\right)/2$. Using the values $k_{\mathrm{p}} = 29$ W/mK and $k_{\mathrm{m}} = 0.158$ W/mK, we obtain $k_{\mathrm{pm}} = 0.314$ W/mK and subsequently $k_{\mathrm{eff}} = 14.7$ W/mK, which is in agreement with the result obtained from the code using the same values of the parameters with 10000 realizations ($k_{\mathrm{eff}} = 14.7 \pm 0.01$ W/mK).

For a random network of $1 \times 1 \times 4$, we have four cases (again, fixing the boundaries to be particles), as shown in Figure 5.9.

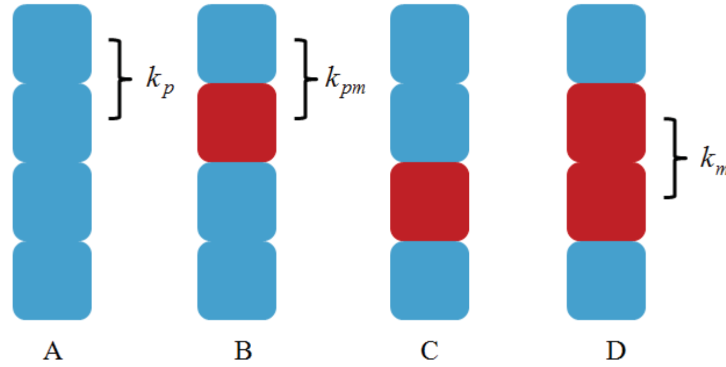


**Figure 5.9 Possible cases for the random network1 × 1 × 4, if the top and bottom layers are fixed to be particles (red: matrix, blue: metal).**

The effective thermal conductivity for case A in Figure 5.9 is ${k_{\text{eff}}}^{(1)} = k_{\text{p}}$. For case B, we can write ${R_{\text{eff}}}^{(2)} = 2R_{\text{pm}} + R_{\text{p}}$, and rewriting this equation in terms of the thermal conductances gives

$$\frac{1}{{\sigma_{\text{eff}}}^{(2)}} = 2\frac{1}{\sigma_{\text{pm}}} + \frac{1}{\sigma_{\text{p}}} = \frac{2\sigma_{\text{p}} + \sigma_{\text{pm}}}{\sigma_{\text{pm}}\sigma_{\text{p}}} \tag{5.10}$$

Thus, the effective thermal conductivity is given by

$${k_{\text{eff}}}^{(2)} = \frac{h}{A}{\sigma_{\text{eff}}}^{(2)} = \frac{(N_3 - 1)r}{N_1 N_2 r^2}\frac{k_{\text{pm}}k_{\text{p}}}{2k_{\text{p}} + k_{\text{pm}}}r = \frac{3k_{\text{pm}}k_{\text{p}}}{2k_{\text{p}} + k_{\text{pm}}} \tag{5.11}$$

Using $\mathrm{N_3} = 4$, $\mathrm{k_p} = 29$ W/mK, $\mathrm{k_m} = 0.158$ W/mK, and $\mathrm{k_{pm}} = 0.314$ W/mK, we obtain ${\mathrm{k_{eff}}}^{(2)} = 0.469$ W/mK for the configuration B. For the configuration C, ${\mathrm{k_{eff}}}^{(3)} = {\mathrm{k_{eff}}}^{(2)} = 0.469$ W/mK (see Figure 5.9).

For the last case, shown in Figure 5.9 D, we have $R_{\text{eff}}^{(4)} = 2R_{\text{pm}} + R_{\text{m}}$, and using a similar approach as above gives

$$k_{\text{eff}}^{(4)} = \frac{h}{A}\sigma_{\text{eff}}^{(4)} = \frac{(N_3 - 1)r}{N_1 N_2 r^2}\frac{k_{\text{pm}} k_{\text{m}}}{2k_{\text{m}} + k_{\text{pm}}} r = \frac{3k_{\text{pm}} k_{\text{m}}}{2k_{\text{m}} + k_{\text{pm}}} \tag{5.12}$$

Again, using the same values for $k_{\text{p}}$, $k_{\text{m}}$, and $k_{\text{pm}}$ as above, we calculate $k_{\text{eff}}^{(4)} = 0.235$ W/mK. If we consider $\varphi = 0.5$, all cases in Figure 5.9 occur with equal weights; thus we find the average of these four cases in order to obtain the effective thermal conductivity of the composite, $k_{\text{eff}} = 7.54$ W/mK. This agrees with the result of numerical simulations using the same values of the parameters for 10000 realizations ($k_{\text{eff}} = 7.54 \pm 0.01$ W/mK).

Based on these analytical calculations, we can derive a formula for the general case of $1 \times 1 \times \text{N}_3$. If we consider $\alpha$, $\beta$ and $\gamma$ to stand for the number of matrix-matrix, particle-particle, and particle-matrix bonds, respectively, we have $\alpha + \beta + \gamma = N_3 - 1$. Then we can write $R_{\text{eff}}^{(s)} = \alpha R_{\text{m}} + \beta R_{\text{p}} + \gamma R_{\text{pm}}$, which gives

$$\frac{1}{\sigma_{\text{eff}}^{(s)}} = \alpha\frac{1}{\sigma_{\text{m}}} + \beta\frac{1}{\sigma_{\text{p}}} + \gamma\frac{1}{\sigma_{\text{pm}}} \tag{5.13}$$

If we rewrite Equation (5.13), we have

$$\begin{aligned} \sigma_{\text{eff}}^{(s)} &= \frac{\sigma_{\text{m}}\sigma_{\text{p}}\sigma_{\text{pm}}}{\alpha\sigma_{\text{p}}\sigma_{\text{pm}} + \beta\sigma_{\text{m}}\sigma_{\text{pm}} + \gamma\sigma_{\text{m}}\sigma_{\text{p}}} \\ &= \frac{r^3 k_{\text{m}} k_{\text{p}} k_{\text{pm}}}{\alpha r^2 k_{\text{p}} k_{\text{pm}} + \beta r^2 k_{\text{m}} k_{\text{pm}} + \gamma r^2 k_{\text{m}} k_{\text{p}}} \end{aligned} \tag{5.14}$$

Finally, the effective thermal conductivity is obtained from Equation (5.14)

$$k_{\text{eff}}^{(s)} = \frac{h}{A}\sigma_{\text{eff}}^{(s)} = \frac{(N_3 - 1)r}{\underbrace{N_1 N_2}_{1} r^2} . \frac{r k_{\text{m}} k_{\text{p}} k_{\text{pm}}}{\alpha k_{\text{p}} k_{\text{m}} + \beta k_{\text{m}} k_{\text{pm}} + \gamma k_{\text{m}} k_{\text{p}}} \tag{5.15}$$

which gives

$$k_{\text{eff}}{}^{(s)} = \frac{k_{\text{m}} k_{\text{p}} k_{\text{pm}} (N_3 - 1)}{\alpha k_{\text{p}} k_{\text{pm}} + \beta k_{\text{m}} k_{\text{pm}} + \gamma k_{\text{m}} k_{\text{p}}} \tag{5.16}$$

For example, if $\beta = \gamma = 0$ (only matrix-matrix bounds present), then ($\alpha = N_3 - 1$) and we have

$$k_{\text{eff}}{}^{(s)} = \frac{k_{\text{m}} k_{\text{p}} k_{\text{pm}} (N_3 - 1)}{\underbrace{\alpha}_{(N_3 - 1)} \; k_{\text{p}} k_{\text{pm}}} = k_{\text{m}} \tag{5.17}$$

and if $\alpha = \gamma = 0$ (only particle-particle bounds present), then ($\beta = N_3 - 1$) and we have

$$k_{\text{eff}}{}^{(s)} = \frac{k_{\text{m}} k_{\text{p}} k_{\text{pm}} (N_3 - 1)}{\underbrace{\beta}_{(N_3 - 1)} \; k_{\text{pm}} k_{\text{m}}} = k_{\text{p}} \tag{5.18}$$

as expected.

### 5.5.1 One-dimensional Simulations

For a one-dimensional random resistor network, the effective thermal conductivity is given by the following equation for resistors in series

$$\frac{1}{k_{\text{eff}}} = \frac{\varphi}{k_{\text{p}}} + \frac{1 - \varphi}{k_{\text{m}}} \tag{5.19}$$

Figure 5.10 shows the results for the one-dimensional simulations ($1 \times 1 \times 100$) for the effective thermal conductivity as a function of the filler volume fraction ($\varphi$), using $k_{\text{p}} = 29$ W/mK, $k_{\text{m}} = 0.158$ W/mK, and 1000 realizations (top and bottom layers fixed to be particles). For comparison, the analytical result for a one-dimensional network is also plotted using Equation (5.19). The effective thermal conductivity of the composite obtained from the simulations becomes $k_{\text{m}} = 0.158$ W/mK when the volume fraction of solid filler approaches zero, as expected from Equation (5.17). As the filler volume fraction ($\varphi$) increases, the effective thermal conductivity remains almost constant below the percolation threshold, however it

increases suddenly and reaches 29 W/mK, the conductivity of alumina-coated Al filler particles, at $\varphi = 1$, as expected from Equation (5.18). As shown in Figure 5.10, the simulation results are in good agreement with the analytical results.

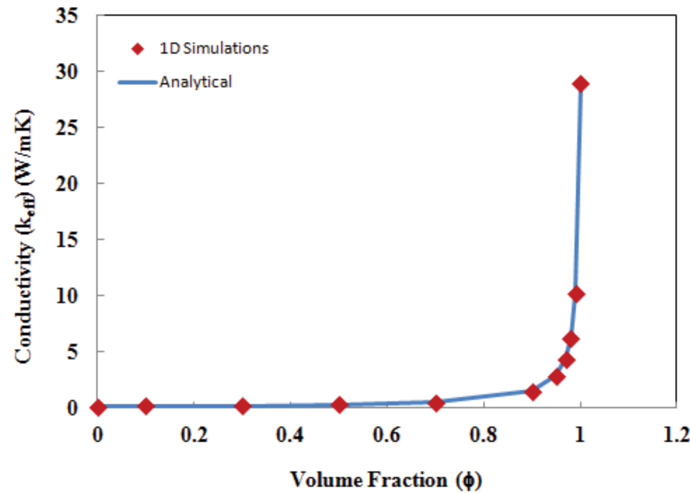


**Figure 5.10 Results of one-dimensional simulations for the effective thermal conductivity ($k_{\text{eff}}$) as a function of the filler volume fraction ($\varphi$).**

If we set the volume fraction of the solid fillers at $\varphi = 0.5$, the effective thermal conductivity of the system approaches a constant value for large $N_3$ values (see Figure 5.11). For these results the physical thickness of the TIM ($h$) was set to 150 μm, and thus increasing $N_3$ increases the resolution. For example, $N_3 = 50$ and $N_3 = 100$ correspond to particle physical lengths of 3 μm and 1.5 μm, respectively. The results for the effective thermal conductivity are presented in Figure 5.11 for three cases: simulations for fixed boundaries (top and bottom layers set to be particles), random boundaries (top and bottom layers randomly selected to be either particles or matrix), and using correction factors related to the top and bottom half layers

obtained from Equation (5.9), when the boundaries are set to be particles. In addition, the analytical results for $\varphi = 0.5$, determined from Equation (5.19), are included for comparison.

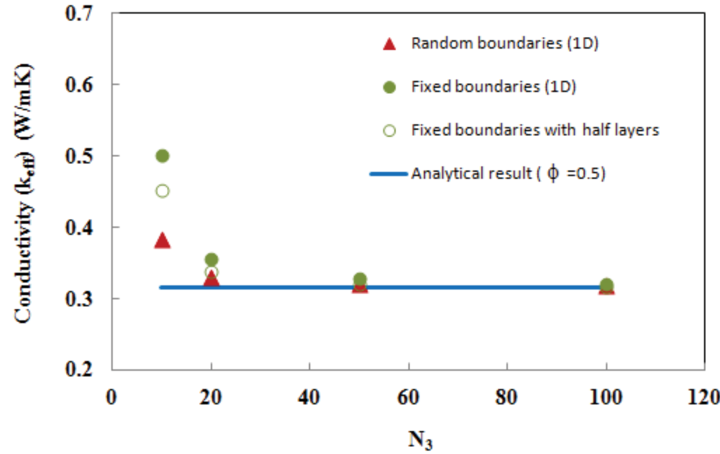


**Figure 5.11 Results of one-dimensional simulations for the effective thermal conductivity ($k_{eff}$) as a function of the lattice size $N_3$ (filler volume fraction $\varphi = 0.5$).**

The results show that for $N_3 \gtrsim 50$ all four cases converge to the constant value obtained from analytical calculations of Equation (5.19).

### 5.5.2 Three-dimensional Simulations

We can define upper and lower bound thermal conductivities for a given volume fraction of filler ($\varphi$) and thermal conductivities for the matrix ($k_m$) and the filler particles ($k_p$) using Equation (2.9), as shown in Figure 2.8. We can estimate a lower bound if the two components (matrix and particle) are arranged parallel to the direction of heat flow ($1/k_{eff}^{\parallel} = \varphi/k_p + (1-\varphi)/k_m$), and an upper bound if the two components are ordered perpendicularly to the direction of heat flow ($k_{eff}^{\perp} = \varphi k_p + (1-\varphi)k_m$). Figure 5.12 shows the results of the three-dimensional simulations

where $N_3 = 20$ is held constant and the cross-sectional area $N_1 = N_2$ increases for $\varphi = 0.1$ (A) and $\varphi = 0.5$ (B). For these results the boundaries were fixed to be particles for 1000 realizations.

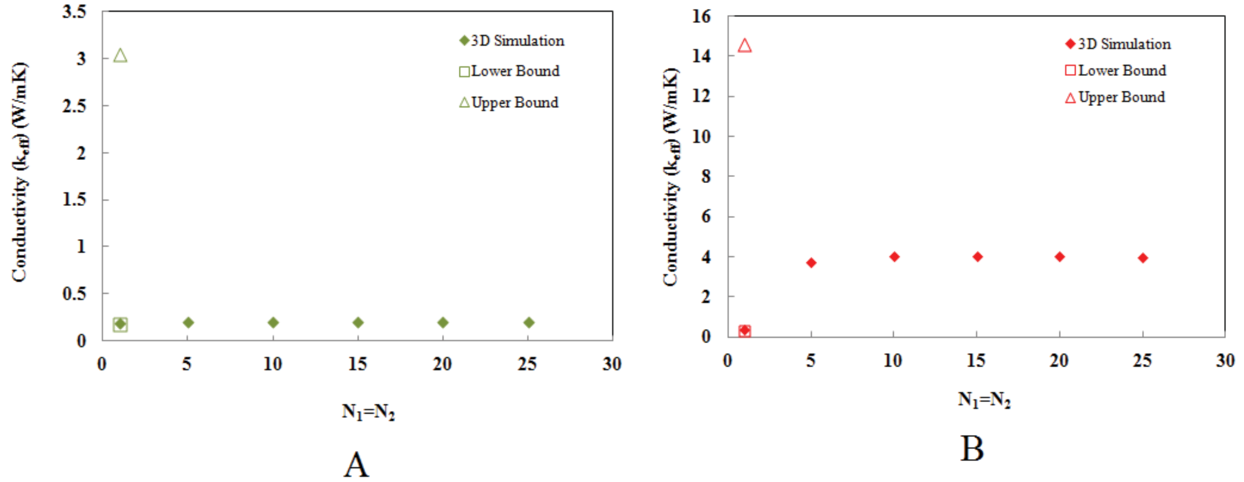


**Figure 5.12 Three-dimensional simulation results for the effective thermal conductivity as a function of $N_1 = N_2$, for the filler volume fraction (A) $\varphi = 0.1$ and (B) $\varphi = 0.5$.**

For a low volume fraction ($\varphi = 0.1$), the effective thermal conductivity remains constant as $N_1 = N_2$ increases. However, for a higher volume fraction ($\varphi = 0.5$) the effective thermal conductivity increases as $N_1 = N_2$ increases and reaches a plateau for $N_1 = N_2 > 10$. The upper and lower bounds for the effective thermal conductivities are included in Figure 5.12 for comparison. The effective thermal conductivity of the network is located between the lower and upper bounds of the effective thermal conductivities, as expected.

## 5.6 Polydispersity and Geometry of Fillers

### 5.6.1 Monodispersed Al Particles

Simulation results are presented in Figure 5.13 for monodispersed Al particles and polymeric matrix (diamonds) in a network $N = N_1 = N_2 = N_3 = 20$ using 500 realizations. The thickness of the TIM ($h$) was set at 150 μm, referring to a physical dimension of about 8 μm for each cube. In this figure, the results of simulations are represented as the red (diamond) data points. The analytical expressions for the lower bound ($k_{\text{eff}}^{\parallel}$, squares) and the upper bound ($k_{\text{eff}}^{\perp}$, triangles) are presented in Figure 5.13 as well.

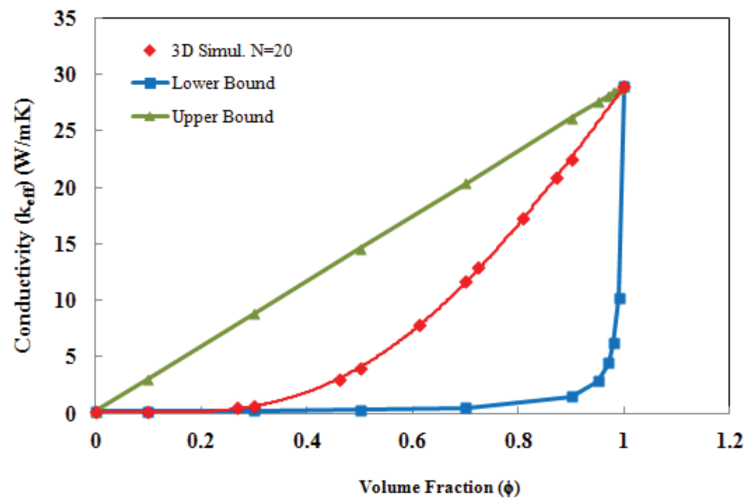


**Figure 5.13 Effective thermal conductivity as a function of particle volume fraction $\varphi$ for monodispersed Al particles and polymeric matrix for red line (diamonds), blue line (squares) for lower bound and green line (triangles) for upper bound (the network size $20 \times 20 \times 20$ using 500 realizations).**

The effective thermal conductivity of the network lies between the lower and upper bound for the thermal conductivities, as expected. The effective thermal conductivity of the network was found to be 0.158 W/mK when $\varphi = 0$ (only matrix in the network) and 29 W/mK when $\varphi = 1$ (only alumina-coated Al particles in the network). The effective thermal conductivity increases as the volume fraction of Al particles increases, as expected, due to the higher effective thermal conductivity of Al particles as compared to the polymeric matrix.

### 5.6.2 Polydispersed Al Particles

As mentioned in the previous sections, the polydispersity of Al particles was approximated by considering a (random) combination of small ($1 \times 1 \times 1$) and large ($3 \times 3 \times 3$) cubic cells (90% small and 10% large). Figure 5.14 shows the simulation results for the effective thermal conductivity of mono- and polydispersed Al particles in a network of $20 \times 20 \times 20$ using 500 realizations (top and bottom layers fixed to be particles). In this case, we did not observe a significant difference between the thermal conductivity of monodispersed and polydispersed networks. This could be due to the fact that a large Al particle is represented by a group of small particles (containing 27 cubes), see Figure 5.4. Thus, a realization of small and large particles could be considered as a possible configuration of only small particles which, in some regions, are randomly grouped together to make a large particle (this is more likely for higher volume fraction values and small networks).

### 5.6.3 Copper Flake Filler

The copper flakes were included in the simulation by considering them as two-dimensional rectangular cells randomly distributed in the network as shown in Figure 5.5. The results of the simulations for a network of $20 \times 20 \times 20$ using 500 realizations are presented in Figure 5.15; the results for the Al particles are also included for comparison.

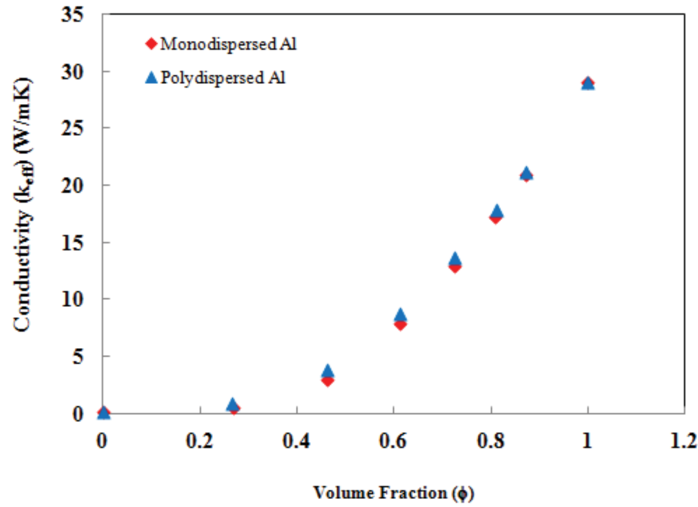


**Figure 5.14 Effective thermal conductivity as a function of the filler volume fraction $\varphi$, for mono- and polydispersed Al particles and a polymeric matrix (red diamonds and blue triangles data points, respectively) for a network of $20 \times 20 \times 20$ using 500 realizations.**

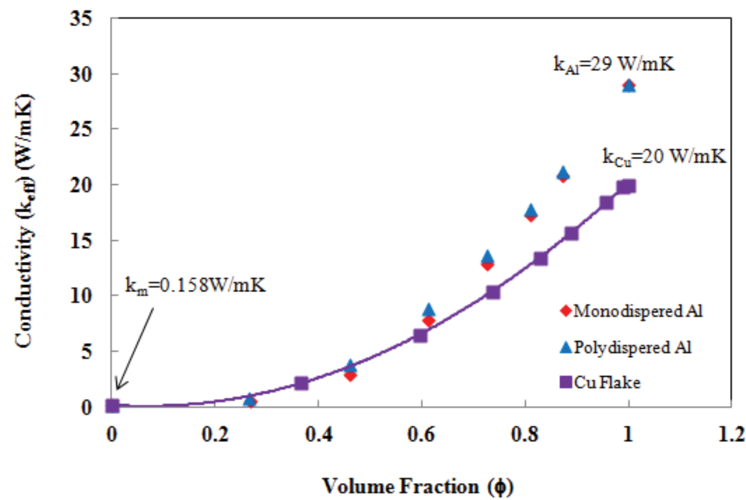


**Figure 5.15 Effective thermal conductivity as a function of the filler volume fraction $\varphi$ for copper flakes (purple squares), and Al particles (red diamonds for mono- and blue triangles for polydispersed particles) with polymeric matrix, for a network size of $20 \times 20 \times 20$ using 500 realizations.**

The effective thermal conductivity starts from 0.158 W/mK at zero volume fraction of flakes (only polymeric matrix present) and goes up as $\varphi$ is increased. It reaches 20 W/mK, the effective thermal conductivity of copper oxide, at $\varphi = 1$.

### 5.6.4 Mixture of Al Particles and Cu Flakes

As discussed in Chapter 4, the addition of copper flakes in TIM compositions of Al particles and a polymeric matrix increases the weight fraction of the solid filler without significantly affecting the viscosity of the TIM due to the Cu flake geometry, as compared to TIM containing only Al particles and a polymeric matrix. Since the weight fraction of metallic filler increases in the TIM formulations, the effective thermal conductivity of the TIM increases. Figure 5.16 shows the simulation results for a mixture of Cu flakes with both mono- and polydisperesed Al particles.

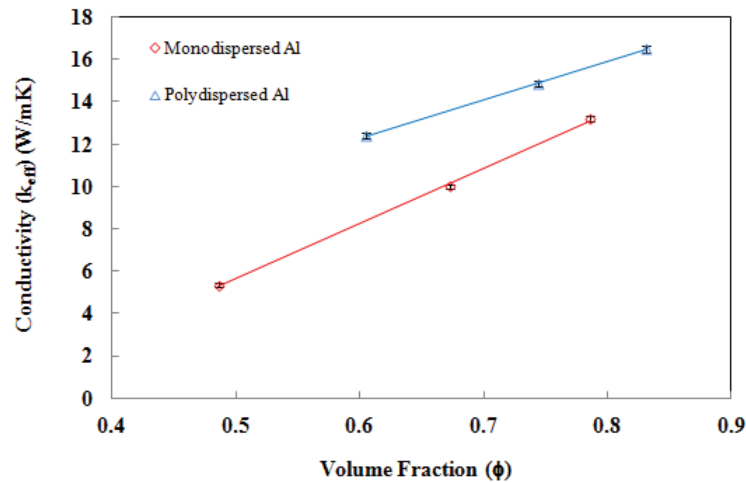


**Figure 5.16 Thermal conductivity as a function of the filler volume fraction $\varphi$ for copper flakes mixed with monodispersed (red, bottom) and polydispersed (blue, top) Al particles with a polymeric matrix, a network size of $20 \times 20 \times 20$ with 500 realizations.**

In the simulations we employed a network size of $20 \times 20 \times 20$ with 500 realizations, where the top and bottom layers were fixed to be Al particles. The volume fraction of Al particles was set to value of $\varphi_{\mathrm{Al}} = 0.3$, whereas the Cu flake volume fractions varied: $\varphi_{\mathrm{Cu}} = 0.1$, 0.2, and 0.3. The effective thermal conductivity was enhanced by increasing the volume fraction of copper flakes, due to the increased solids content with a high intrinsic thermal conductivity. The standard deviation on the simulations was obtained by repeating the simulations for each $\varphi_{\mathrm{Cu}}$ three times, resulting in a 2.5 % deviation (see Appendix 5.9).

## 5.7 Simulation vs. Experimental Results

According to the experimental data reported in Chapter 4 good results, reaching up to 9.4 W/mK, were obtained for the effective thermal conductivity of TIM compositions incorporating polydispersed Al particles, Cu flakes, oligo(ethylene glycol), and amino oligo(ethylene oxide), PEO-$NH_2$ surfactant. In this section, we applied the numerical simulations to TIM formulations containing fillers and a polymeric matrix (with and without surfactant) to explore different factors influencing the effective thermal conductivity of a TIM. In the numerical simulations we used a network size of $50 \times 50 \times 50$ with 100 realizations, to compare the computational results with the experimental results, unless otherwise specified. In addition, boundary conditions were considered such that the top and bottom layers were randomly chosen to be either particles or matrix.

### 5.7.1 Effective Thermal Conductivity of Fillers

The experimental results for TIM samples containing polydispersed Al particles and a polymeric matrix with weight fractions of 72%, 75%, and 78% w/w (corresponding to volume fractions of 48%, 52%, and 55% v/v, respectively) are compared with the simulation results in Figure 5.17 A.

The sample with a higher volume fraction has a slightly higher effective thermal conductivity than predicted. Uncertainties on the experimental results (5 %) due to instrumental errors are indicated, as well as the standard deviation on the simulation results obtained by repeating the simulations three times (3 %).

The simulation results were obtained by estimating an effective thermal conductivity for the Al particles ($k_{\mathrm{eff}}^{\mathrm{Al}}$). This quantity is not neccesarily the same as the thermal conductivity of the pure Al particles: The alumina layer on the Al particles is porous, and the air trapped in it (Figure 5.17 B) has a significant influence in decreasing the effective thermal conductivity of the particles. Another possibility that could explain the decrease in $k_{\mathrm{eff}}^{\mathrm{Al}}$ is the presence of air trapped between the particles and the polymeric binder and/or between the TIM and the flux meters. By comparing the results of the numerical simulations with the experimental data for a given volume fraction (48%, for example), we estimated the effective thermal conductivity of the Al particles (with the alumina layer) to be $k_{\mathrm{eff}}^{\mathrm{Al}} = 7$ W/mK rather than 29 W/mK, which is the effective thermal conductivity of solid alumina. This estimated conductivity, $k_{\mathrm{eff}}^{\mathrm{Al}} = 7$ W/mK, was then used to determine the effective thermal conductivity of the TIM for the other volume fractions (52% and 55%).

To estimate the effective thermal conductivity of the Cu flakes in the network, we compared the experimental results for TIM samples containing only Cu flakes and the polymeric matrix with weight fractions of 83%, 85%, and 88% w/w with the simulation results for the coresponding volume fractions (35%, 39%, and 45% v/v, respectively), see Figure 5.18 A. Similarly to the Al particles, error bars calculated from the instrumental uncertainties (5%), and the standard deviation for triplicate simulations (1.5%) are included in the plots. By comparing the simulation results with the experimental data, the effective thermal conductivity of Cu flakes

in the network was estimated to be $k_{\mathrm{eff}}^{\mathrm{Cu}} = 9$ W/mK rather than 20 W/mK, which is the effective thermal conductivity of copper oxide. Similarly to Figure 5.17, we used the effective thermal conductivity of Cu flakes ($k_{\mathrm{eff}}^{\mathrm{Cu}}$) estimated from the experimental result for one of the volume fractions to obtain the effective thermal conductivitities of the TIM for the other volume fractions.

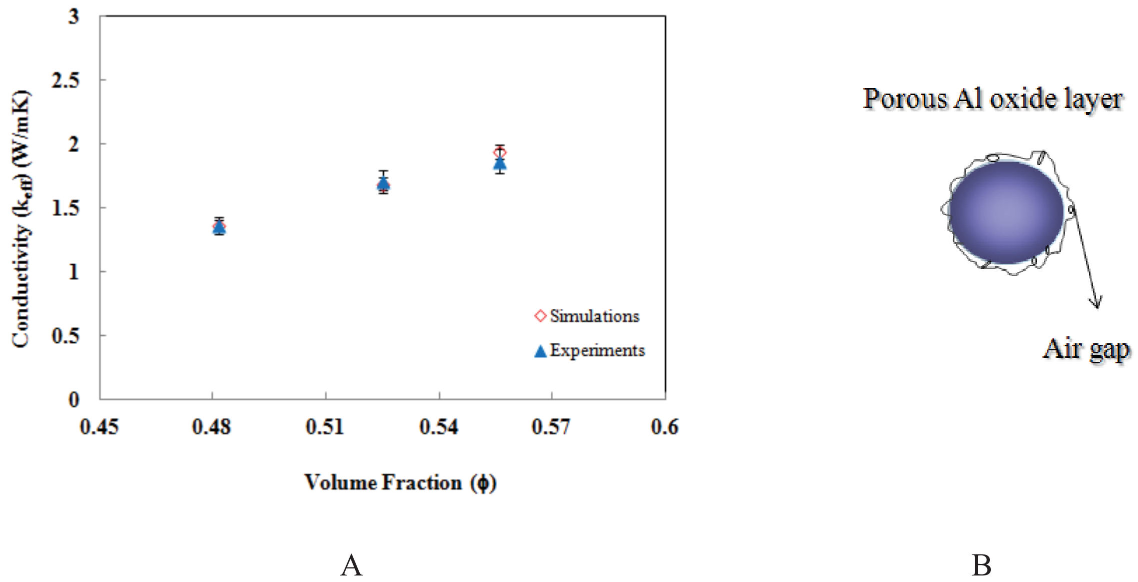


**Figure 5.17 (A) Experimental (blue triangles) and numerical (red diamonds) results for the effective thermal conductivity of composites containing polydispersed Al particles (sizes $1 \times 1 \times 1$ and $3 \times 3 \times 3$) and a polymeric matrix as a function of the filler volume fraction $\varphi$. (B) Schematic view of the porous oxide layer of Al particles and the air gaps.**

The air gap in the copper oxide layer should decrease the effective thermal conductivity of the flakes, as shown in Figure 5.18 B. Air trapped between the particles and the polymeric binder and/or between the TIM and the flux meters may also lead to a decrease in $k_{\mathrm{eff}}^{\mathrm{Cu}}$. Given that aluminium is more reactive toward atmospheric oxidation than copper, it is expected that the

oxide layer of aluminum would be thicker (and more porous). Thus the oxide layer has less influence on the conductivity of the copper flakes as compared to the Al particles.

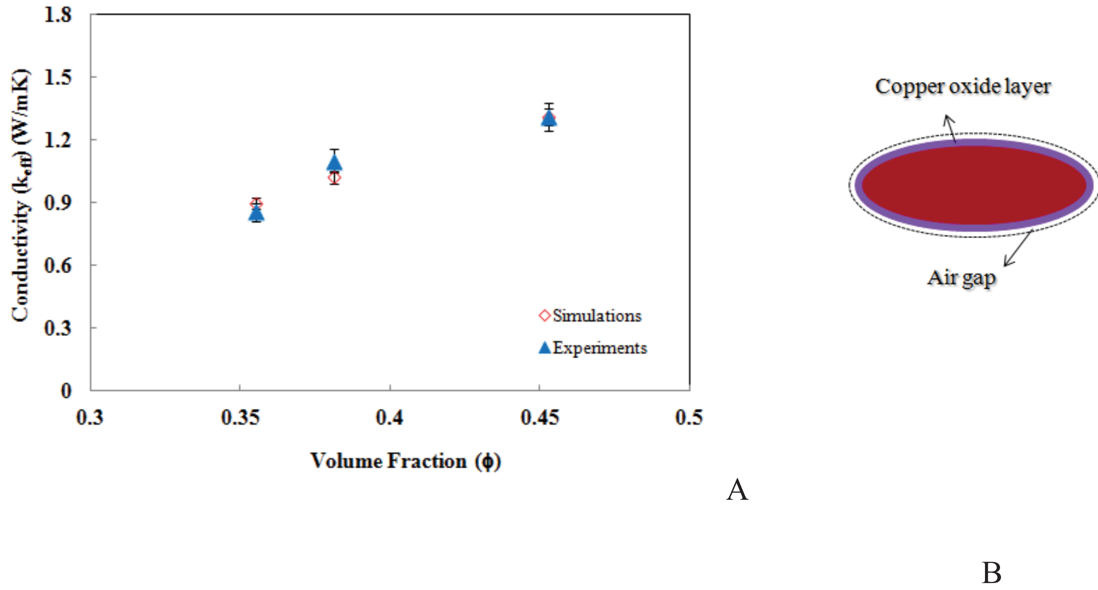


**Figure 5.18 (A) Experimental (blue triangles) and numerical (red diamonds) results for the effective thermal conductivity of Cu flakes and polymeric matrix as a function of the volume fraction of Cu flakes, $\varphi$. (B) Schematic view of the copper oxide layer and the air gaps.**

### 5.7.2 The Effect of Surfactant

A similar approch was used to study the effect of the surfactant on the effective thermal conductivity of the TIM compositions. By comparing the experimental and simulation results for components including amino oligo(ethylene oxide) surfactant, PEO-$NH_2$, we can parameterize the effective thermal conductivity of the Al particles and the Cu flakes as a function of the surfactant concentration using surfactant concentration-dependent thermal conductivities, $k_{\mathrm{eff}}^{\mathrm{Al}}(s)$. To this end, for instance, for the mixture of (polydispersed ) Al particles with matrix and

($s$) percentage of surfactant, we can estimate the effective thermal conductivity of the Al particles for a given volume fraction of Al fillers, such that the simulation and experimental results are close to each other. Then we use this surfactant concentration-dependent thermal conductivity of the Al filler to obtain the effective thermal conductivity of the network for the other volume fractions. We can verify that the parametrized thermal conductivity of Al works for all the volume fractions and only depends on the percentage of surfactant. This process is then repeated for the different percentages of surfactant to determine the surfactant concentration-dependent thermal conductivity of the Al particles, $k_{\mathrm{eff}}^{\mathrm{Al}}(s)$. The experimental and simulation results for the effective thermal conductivity of the composites (polydispersed Al particles with sizes of $1 \times 1 \times 1$ and $3 \times 3 \times 3$, the polymeric matrix, and surfactant) vs. surfactant concentration are presented in Figure 5.19 for filler volume fractions of 48%, 52%, and 55%.

Next, we followed the same procedure for the Cu flakes. The surfactant concentration-dependent effective thermal conductivity of the Cu flakes, $k_{\mathrm{eff}}^{\mathrm{Cu}}(s)$, was estimated by comparing the experimental and the simulation results for different percentages of surfactant. Figure 5.20 presents the experimental and simulation results for the effective thermal conductivity of samples containing Cu flakes as filler, a polymeric matrix, and surfactant vs. surfactant content (for filler volume fraction of 35%, 39%, and 45%).

The resulting surfactant-dependent effective thermal conductivity of polydispersed Al particles and Cu flakes are presented in Figure 5.21 (the results are also listed in Table 5.1). These estimated surfactant-dependent effective thermal conductivities were then used in simulations for mixtures of Cu flakes, Al particles, polymeric matrix, and surfactant to predict the effective thermal conductivity of the composites.

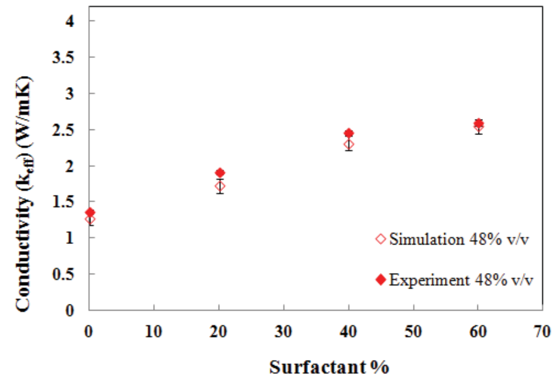


**A**

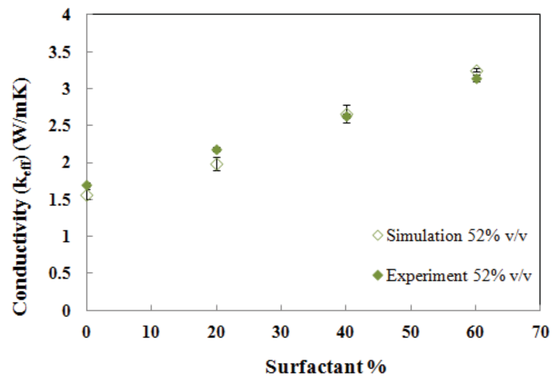


**B**

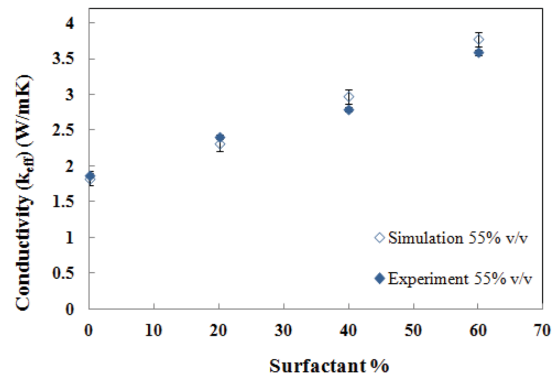


**C**

**Figure 5.19 Experimental (filled diamond) and numerical (unfilled diamond) results for the effective thermal conductivity of composites (polydispersed Al particles, polymeric binder, and surfactant) vs. surfactant content. (A), (B), and (C) are for filler volume fractions of 48%, 52%, and 55%, respectively.**

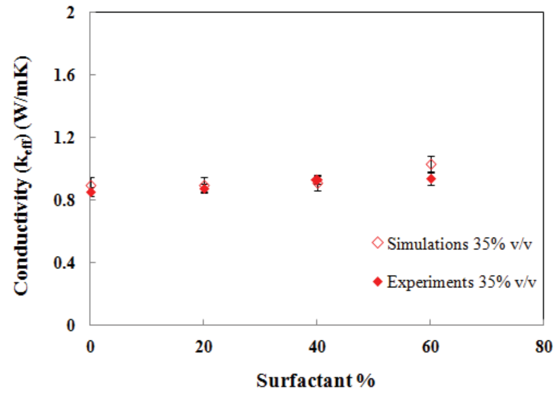

A

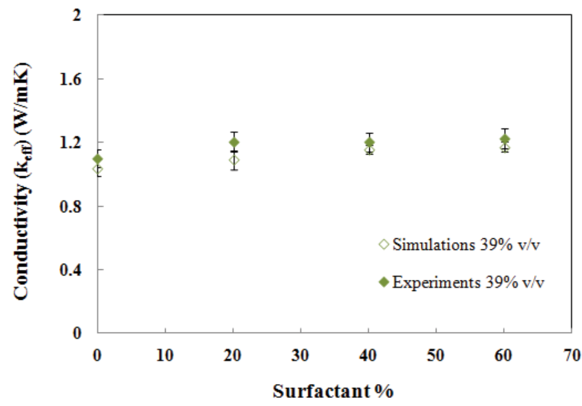

B

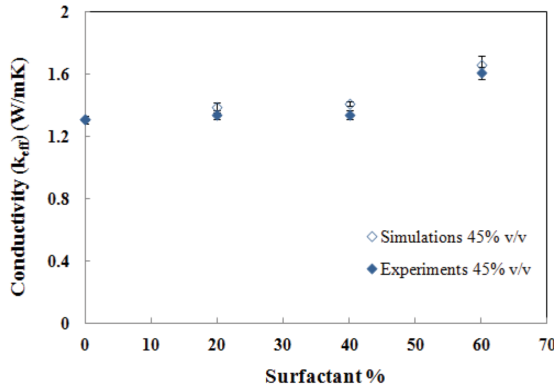

C

**Figure 5.20 Experimental (filled diamonds) and numerical (unfilled diamonds) results for the thermal conductivity of samples containing Cu flakes, polymeric matrix, and surfactant vs. surfactant content. (A), (B), and (C) are for filler volume fractions of 35%, 39%, and 45%, respectively.**

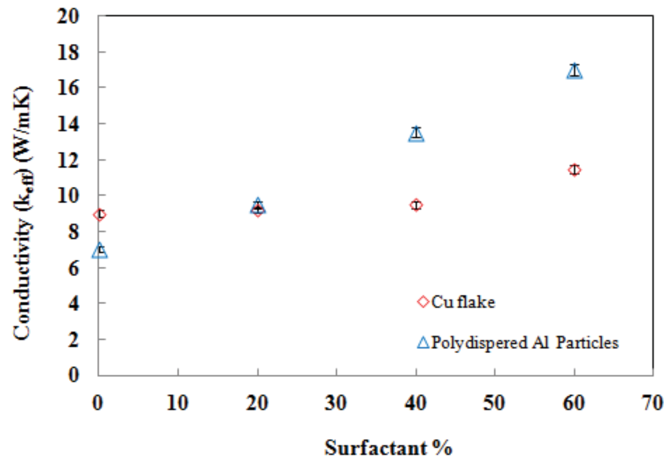


**Figure 5.21 Estimated values of surfactant concentration-dependent effective thermal conductivity for polydispersed Al particles (triangle) and Cu flakes (diamond).**

**Table 5.1 Estimated value of surfactant concentration-dependent effective thermal conductivity of Al particles and Cu flakes.**

| **Surfactant %** | $k_{\text{eff}}^{\text{Al}}$ **(W/mK)** | $k_{\text{eff}}^{\text{Cu}}$ **(W/mK)** |
|---|---|---|
| **0** | 7 | 9 |
| **20** | 9.5 | 9.2 |
| **40** | 13.5 | 9.5 |
| **60** | 17 | 11.5 |

In the absence of surfactant in the TIM compositions, the surfactant concentration-dependent thermal conductivity of Cu flakes is higher than for the Al particles. This may be due to the fact that Al is more reactive than Cu, so that the oxide layer is more porous (i.e. more air is trapped) for the Al particles. By increasing the surfactant content in the TIM composition, the

surfactant concentration-dependent thermal conductivity of both the Al particles and the Cu flakes increase. For the Al particles this increase is almost linear, which could arise from bonding of the surfactant to both the oxide layer and the metal surface (through the pores). However the effective thermal conductivity of the Cu flakes increases significantly only for the highest surfactant concentration (60%; see also Figure 5.20).

In the next step, the estimated surfactant concentration-dependent thermal conductivities $k_{\mathrm{eff}}^{\mathrm{Al}}(s)$ and $k_{\mathrm{eff}}^{\mathrm{Cu}}(s)$ were used to predict the effective thermal conductivity of the TIM composition containing the (polydispersed ) Al particles and Cu flakes, the polymeric matrix, and the surfactant.

The results of the numerical simulations for these composites are compared with the experimental data in Figure 5.22. The volume fractions for the Al particles and the Cu flakes were calculated from the corresponding weight fractions of the fillers (reported in Table 4.6). The trends predicted for the effective thermal conductivity of the TIM compositions are in good agreement with the experimental data for low surfactant contents. However, the simulation results display discrepancies for surfactant contents of 40% and 60%. In fact, the modeling prediction for a surfactant content of 40% is very close to the experimental data for a load 50 PSI (Table 4.13). One should also note that, although the simulation results show some saturation effect for high surfactant contents, this could be due to the fact that the filler volume fraction is lower for the 60% surfactant content. This means that the increase in the effective thermal conductivity of the composite due to the addition of the surfactant is not linear, since they do not have the same volume fractions.

In an attempt to explain the large increase in effective thermal conductivity observed for the TIM composition with 60% surfactant (Figure 5.22), we considered several possible options.

First, we studied the effect of polydispersity of Al particle by considering two cases: (a) two sizes for the Al particles $1 \times 1 \times 1$ and $4 \times 4 \times 4$ (instead of $3 \times 3 \times 3$), and (b) four sizes for the Al particles, namely $1 \times 1 \times 1$, $2 \times 2 \times 2$, $3 \times 3 \times 3$, and $4 \times 4 \times 4$. The first case corresponds to particles with physical lengths of 3 μm and 12 μm, respectively. In the second case, the size of Al particles is 3 μm, 6 μm, 9 μm and 12 μm, respectively. In both cases we again estimated the surfactant concentration-dependent effective thermal conductivity of the Al particles and the Cu flakes, and then used them to predict the effective thermal conductivity of the composites (Al particles, Cu flakes, polymeric matrix, and surfactant). No significant changes were observed (data not shown) when comparing these two cases with composites containing Al particles with sizes of $1 \times 1 \times 1$ and $3 \times 3 \times 3$.

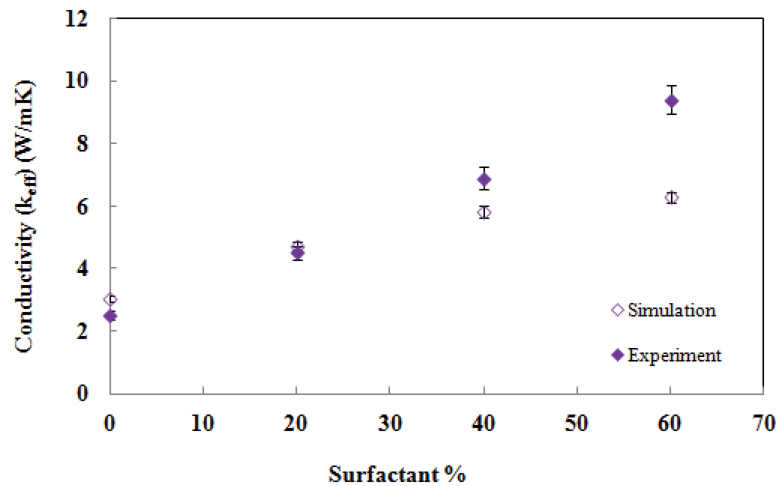


**Figure 5.22 Results of the effective thermal conductivity for composites containing polydispersed Al particles (sizes $1 \times 1 \times 1$ and $3 \times 3 \times 3$), Cu flakes, a polymeric matrix, and surfactant vs. surfactant content for experiments (filled diamonds) and predicted numerical simulations (unfilled diamonds) using estimated surfactant concentration-dependent effective thermal conductivity of fillers.**

As an alternative scenario, we also explored a possibility where the addition of surfactant would not only increase the effective thermal conductivity of the filler particles, but also the thermal conductivity of the matrix. Thus, we also defined a surfactant concentration-dependent effective thermal conductivity, $k_{\mathrm{eff}}^{\mathrm{Matrix}}(s)$ for the matrix component.

First, the surfactant concentration-dependent effective thermal conductivity of the Al particles, the Cu flakes, and the matrix, i.e. $k_{\mathrm{eff}}^{\mathrm{Al}}(s)$, $k_{\mathrm{eff}}^{\mathrm{Cu}}(s)$, and $k_{\mathrm{eff}}^{\mathrm{Matrix}}(s)$, were estimated so that there was good agreement between the experimental and the numerical results (as estimated from a root-mean-squared deviation, RMSD, of less than 0.1) for the effective thermal conductivity of the composites containing a single type of filler particles, polymeric matrix, and surfactant. These estimated values were then imposed on the simulations for composites containing the (polydispersed) Al particles and the Cu flakes, as well as the polymeric matrix and the surfactant, to predict the effective thermal conductivity of the network. Although the numerical simulations again displayed good agreement with the experimental data (data not shown), there was still discrepancy for the 60% surfactant composition.

Finally, we verified that in order to achieve good agreement between the experimental and the simulation results for 60% surfactant, the effective thermal conductivity of the Al particles should be set to the effective thermal conductivity of alumina, i.e. 29 W/mK. In fact, the result of numerical simulations for TIM compositions with polydispersed Al particles ($1 \times 1 \times 1$ and $3 \times 3 \times 3$), Cu flakes, polymer matrix, and surfactant (60%), using $k_{\mathrm{eff}}^{\mathrm{Al}} = 29$ W/mK rather than 17.5 W/mK, as reported in Figure 5.21, $k_{\mathrm{eff}}^{\mathrm{Cu}} = 11.5$ W/mK as shown in Figure 5.21, and $k_{\mathrm{eff}}^{\mathrm{Matrix}} = 0.158$ W/mK, yielded $k_{\mathrm{eff}} \approx 9.2$ W/mK, which is very close to the experimental result 9.4 W/mK. Although this high value for the effective thermal conductivity of the Al particle

leads to good agreement with the experimental data, we also lose the good agreement between the experimental and simulation results for single filler (only Al particle), polymeric matrix, and surfactant systems by this approach.

This discrepancy at the highest surfactant content could be due partly to some type of percolation effect. In the modeling formulation, we assumed that the effective thermal conductivity of the particles depends on the homogeneous distribution of the surfactant. This means that the thermal conductivity of *all* the particles should increase by increasing the surfactant concentration. However this increase may in fact be a heterogeneous effect, meaning that the change in effective thermal conductivity may only happen in some parts of the network (i.e. not for all particles). In this case, when we increase the surfactant concentration beyond some threshold value, percolation occurs and these local regions connect to each other, resulting in an elevation of the effective thermal conductivity of the composites. The addition of Cu flakes could amplify this effect, perhaps due to the different size and geometry of the Al particles and the Cu flakes.

## 5.8 Conclusion

Numerical simulations based on the method of random resistor networks were used to estimate the effective thermal conductivity of TIM formulations. We studied the effective thermal conductivity of composites containing Al particles (mono- and polydispersed in size) and copper flakes, as well as combinations of both, using numerical simulations. We also discussed the effect of surfactants using surfactant concentration-dependent effective thermal conductivities for the filler particles. According to the numerical simulations, the effective thermal conductivity of Al particles increases linearly with the surfactant concentration, while the effective thermal

conductivity of the Cu flakes only increased significantly for highest surfactant content. Using the estimated surfactant concentration-dependent thermal conductivities of the filler particles, the predictions of numerical simulations were in good agreement with the experimental results reported in Chapter 4, except for the highest surfactant content (60%). We also discussed possible scenarios in an attempt to explain the abnormally high effective thermal conductivity experimentally obtained for these samples. Possible improvements and future directions to address this and other issues are discussed in Chapter 6.

## 5.9 Appendix: Simulation Time and Uncertainlies

The initial version of the simulation code ran very slowly and could not be used for resolutions higher than $30\times30\times30$. The code was modified using sparse matrices; the new code runs faster and also can be used for higher resolutions. Table 5.2 shows the time required for simulations for the new versions of the code (on a Windows Desktop, Intel Core i7 2.67 GHz, with 8 GB memory) for different $N$ ($N_1 = N_2 = N_3 = N$).

**Table 5.2: Simulation times for new versions of code.**

| $N$ | Time (R=1) | Time ($R$=100) |
|---|---|---|
| **10** | 2 sec | 6 min |
| **20** | 12 sec | 20 min |
| **30** | 1 min | 1.7 hours |
| **40** | 2.5 min | 4.2 hours |
| **50** | 6.4 min | 10.7 hours |

To illustrate the convergence of the numerical result when the lattice size is increased, the results for the effective thermal conductivity of a composite containing only (monodispersed ) Al particles and matrix in one-dimensional (1D) and three-dimensional (3D) networks for different $N$ ($N_1 = N_2 = N_3 = N$ in 3D, and $N_1 = N_2 = 1$ and $N_3 = N$ in 1D) are listed in Table 5.3. Here, we used $\varphi = 0.5$, $k_{\rm p} = 29$ W/mK and $k_{\rm m} = 0.158$ W/mK, with 500 (1D) and 100 (3D)

realizations, and applied random boundary condition (top and bottom layers randomly selected to be either particle or matrix).

**Table 5.3: Simulated effective thermal conductivities for different $N$.**

| $N$ | $k_{\mathrm{eff}}^{\mathrm{1D}}$ (W/mK) | $k_{\mathrm{eff}}^{\mathrm{3D}}$ (W/mK) |
|---|---|---|
| **10** | 0.37 | 4.02 |
| **20** | 0.33 | 3.74 |
| **30** | 0.33 | 3.69 |
| **40** | 0.32 | 3.66 |
| **50** | 0.32 | 3.65 |

Finally, the uncertainties on the simulations were estimated using three samples. As an example, the results for (monodispersed) Al particles with $N_1 = N_2 = N_3 = 20$ are presented in Table 5.4. We used $k_{\mathrm{p}} = 29$ W/mK and $k_{\mathrm{m}} = 0.158$ W/mK, 100 realizations (random boundary condition).

**Table 5.4: Simulation uncertainties for $N_1 = N_2 = N_3 = 20$.**

| $\varphi$ | $k_{\text{eff}}^{(1)}$ (W/mK) (sample 1) | $k_{\text{eff}}^{(2)}$ (W/mK) (sample 2) | $k_{\text{eff}}^{(3)}$ (W/mK) (sample 3) | $k_{\text{eff}}$ (W/mK) (average) | STD |
|---|---|---|---|---|---|
| **0** | 0.1580 | 0.1580 | 0.1580 | 0.1580 | 0 |
| **0.1** | 0.1948 | 0.1947 | 0.1943 | 0.1946 | 0.0002 |
| **0.3** | 0.5785 | 0.5785 | 0.5662 | 0.5744 | 0.0071 |
| **0.5** | 3.7392 | 3.7390 | 3.7442 | 3.7408 | 0.0029 |
| **0.7** | 11.2529 | 11.2528 | 11.2600 | 11.25523 | 0.0041 |
| **0.9** | 22.2358 | 22.2358 | 22.2935 | 22.25503 | 0.0333 |
| **1** | 29 | 29 | 29 | 29 | 0 |

# Chapter 6

## Concluding Remarks

## 6.1 Summary and Contributions to Knowledge

It was mentioned at the beginning of this dissertation that one of the major challenges in the formulation of TIM is to make them electrically insulating while maintaining a high effective thermal conductivity. While many theoretical and experimental studies have focused on improving the effective thermal conductivity of TIM, less attention has been devoted to the polymer properties and their interactions with the filler particles.

One of the main goals of the present dissertation was to achieve TIM formulations with a high effective thermal conductivity, by studying the influence of several polymers and different filler particles in a systematic fashion. This goal was accomplished by the selection of an appropriate polymer matrix, resulting in the encapsulation of the metallic particles, as well as with an optimal combination of filler particles with spherical (Al) and flake (Cu) geometries.

A novel type of end-reactive (telechelic) polymer, namely amino-functionalized monotelechelic oligomers of ethylene oxide (PEO-$NH_2$), was developed to enhance matrix-filler interactions. The synthesis and the application of these amino-functionalized monotelechelic oligomers of ethylene oxide were studied in Chapter 3. Two methods were developed for the preparation of PEO-$NH_2$, namely the anionic polymerization of ethylene oxide initiated by the potassium salt of 2-ethanolamine, and the chemical modification of a commercial oligo(ethylene glycol) monomethyl ether sample (MPEG modified to MPEG-$NH_2$). $^1$H NMR analysis was used to confirm the structure of the oligomers, including their molecular weight and the presence of a primary amine end group. Analysis by SEC and end group titration were also employed to determine the molecular weight of the oligomers. IR spectroscopy analysis further confirmed the presence of primary amine end groups in the samples.

The influence of the PEO-$NH_2$ oligomers on the properties of metallic surfaces such as copper was investigated by different techniques. These oligomers were used to bind on copper surfaces, with the goal of making them electrically insulating. X-ray photoelectron spectroscopy (XPS) and contact angle measurements provided evidence for interactions (binding) of the amine group with the metallic surfaces and/or their oxide layer. The XPS results indicated the presence of bonds between PEO-$NH_2$ and the copper surfaces. Resistivity measurements showed that copper flakes became essentially electrically insulating after encapsulation with the oligomers, the resistivity being higher for PEO-$NH_2$ oligomer more carefully purified to remove residual salt contaminants. All results gathered confirmed that the PEO-$NH_2$ oligomers can encapsulate the copper surface due to their binding to the surface of copper metal and/or the oxide layer on its surface. These oligomers were used in TIM formulations to optimize the effective thermal conductivity of the TIM and electrically insulate the metallic fillers.

In Chapter 4, we reported on a series of TIM formulations incorporating metallic particles, a polymeric matrix, as well as the PEO-$NH_2$ oligomers as surfactant, and the method used to measure the effective thermal conductivity of the TIM. The thermal resistance was measured according to ASTM standard D 5470, using an instrument designed in the Microelectronics Heat Transfer Laboratory (MHTL), Department of Mechanical and Mechatronics Engineering, University of Waterloo. The influence of various factors including the geometry, the volume fraction of fillers, and surface wetting on the performance of the TIM compositions was explored in a systematic fashion. Optimal results were obtained for TIM compositions incorporating copper flakes dispersed in an oligo(ethylene glycol) – amino oligo(ethylene oxide) surfactant mixture (PEO-$NH_2$), yielding effective thermal conductivities of

up to 9.4 W/mK. In addition, thin layers (down to 0.004 mm) were achieved for the TIM compositions developed as compared to commercial TIM formulations (0.07 mm).

Different theoretical approaches have been suggested to estimate the effective thermal conductivity of composites. In this research, we developed a computational approach based on the random resistor network (RRN) method to study the effects of the size distribution, the geometry of the filler particles, as well as the surfactant on the effective thermal conductivity of the TIM. In particular, we introduced surfactant concentration-dependent effective thermal conductivities for the filler particles and used them to predict the effective thermal conductivity of the TIM composites. Our numerical simulations were in excellent agreement with the experimental data in most cases.

## 6.2 Suggestions for Future Work

The present dissertation involved close interactions between three disciplines, namely chemistry, mechanical engineering, and mathematics. TIM compositions with high effective thermal conductivities were obtained through systematic formulation optimization. However, additional studies are still required to optimize the composition of the filler particles and the polymeric matrix, and to further improve the effective thermal conductivity obtained. The influence of several parameters (e.g. the size of the particles and their geometric characteristics, as well as the thickness of the oxide layer on the metallic surfaces) on the performance of TIM compositions could be further clarified.

It would also be interesting to determine whether the improvement in the effective thermal conductivity of the TIM might be due in part to an increase in the effective thermal conductivity of the matrix as a result of the addition of the surfactant. Numerical simulations

based on the RRN method can also help in designing efficient combinations of particles and polymeric matrix and achieving further increases in the effective thermal conductivity of the TIM compositions.

Although the model predictions display good agreement with the experimental data, there remains potential for further refinement. For instance, as discussed in the modeling chapter, the increase in the effective thermal conductivity of the TIM at high surfactant concentrations could be due to a percolation-type effect. One could include heterogeneous surfactant concentration-dependent thermal conductivities for the particles to validate this prediction. Additional measurements for TIM formulations at high surfactant concentrations are clearly also warranted to refine the model. Moreover, experimental methods to estimate the thickness of the oxide layers on the metallic fillers with or without surfactant could be explored. The experimental data for the effective thermal conductivities could also be used to calculate the thickness of the oxide layers, which in turn can be validated with the experimental studies using surface analysis techniques.

# Appendix

## Matlab Codes

## A.1 Network Description

The main code (see below) is first used to define the random resistor network, in one or three dimensions, for composites containing monodispersed or polydispersed Al particles and matrix cubes, as well as Cu flakes. Various options include:

(1) For one-dimensional (1D) simulations, we set the parameters "NN1" and "NN2" to 1.

(2) The parameter "LargeP" changes the combination. For monodispersed Al particles, we use LargeP=0. If the volume fraction of copper flakes ("phiCu") is set to zero, it then includes the combination of monodispersed Al particles and matrix; however, for a non-zero phiCu, it refers to a mixture of monodispersed Al particles, matrix, and copper flakes.

(3) For polydispersed Al particles with dimensions $1 \times 1 \times 1$ and $3 \times 3 \times 3$, we use LargeP=1. Again, selecting a non-zero or zero value for phiCu runs the simulation with or without Cu flakes, respectively. For polydispersed Al particles with dimensions $1 \times 1 \times 1$, $2 \times 2 \times 2$, $3 \times 3 \times 3$, and $4 \times 4 \times 4$, we use LargeP=2.

One should note that for polydispersed Al particles and Cu flakes, the input volume fraction (phiAl or phiCu) is selected such that the output volume fraction is the same as the experimental volume fraction of the Al particles or the copper flakes. For monodispersed Al particles the input and output volume fractions are equal.

A major challenge in simulations of random resistor networks is to define the problem in a matrix form $AX = B$ (Equation (5.5). The function "randomRNModel", as well as "FindNeighbor" and "Cal_Neighbor_S", obtained from Reference (1) with some minor changes (see next sections), are used to generate the appropriate matrix form:

```
[A B]=randomRNModel(N,km,kp)
```

The Matlab command "\" (matrix left division) is used to find the temperature distribution $X$. Equation (5.4) is then used to determine the effective thermal conductivity.

## A.2 Functions

The functions "randomRNModel", "FindNeighbor" and "Cal_Neighbor_S" were obtained from Reference (1). These functions were modified from their original versions to be used in the calculation of effective thermal conductivity; these changes are highlighted in the codes below. A major improvement to these original functions was the use of sparse matrices. With these new versions the simulation time was significantly decreased, and the code could also be run for higher resolutions. The function ndSparse, written by Matt Jacobson, was used for N-dimensional sparse arrays (downloaded from MATLAB Central File Exchange).[2]

Finally, the functions plot3D and voxel, written by Carlos Martinez-Ortiz, were downloaded from MATLAB Central File Exchange.[3] These functions can be used for three-dimensional visualizations.

## A.3 Main Matlab Code

```
% Main code: © Shahla Aliakbari, 2012
close all;
clear all;
global rr
global kc
%%%%% Choosing the combination
LargeP=0;          % 0 (monodis.), 1 or 2(polydis., two and four types)
phiAl=0.5;         % phiAl_in for Al particles
phiCu=0;           % phiCu_in for Cu flakes
%%%%% Choosing the boundary condition
BC=0;              % 0 or 1 for random or fixed boundary conditions
 %%%%% The size of the network
NN1=50;            % Number of resistors in the x-direction
NN2=50;            % Number of resistors in the y-direction
```

```
NN3=50;              % Number of resistors in the z-direction
%%%%% Parameters
km=0.158             % Effective thermal conductivity of matrix (W/mK)
kp=29;               % Effective thermal conductivity of Al (W/mK)
kc=20;                % Effective thermal conductivity of Cu (W/mK)
kpm=2*(km*kp/(kp+km)); % Al particle-matrix conductivity
kpc=2*(kc*kp/(kp+kc));     % Al Particle-Cu flakes conductivity
kmc=2*(kc*km/(km+kc));  % Cu flakes-matrix conductivity
hTIM=150e-6;                 % TIM thickness
rr=hTIM/(NN3-1);            % Size of each cube (lattice space)
AA=(rr)^2*NN1*NN2;      % TIM area
Tt=0;                            % Temperature  at the top and bottom layers
Tb=50;                           % Only temperature difference is important

NumReal=100;                 % Number of realizations

Qtot=0;                          % To calculate Qtot
VolFAl=0;                      % To calculate phiAl_out
VolFCu=0;                      % To calculate phiCu_out
tic                                % To estimate the simulation time

%%%%% Main loop (over realizations)
for NREAL=1:NumReal

N=ones(NN1,NN2,NN3);    % 2 for particle and 1 for matrix
BB=rand(NN1,NN2,NN3);  % Generating a random matrix to assign particles
N(BB<phiAl)=2;                 % Adding particles based on the fraction phiAl

%%%%% To randomly choose some of the particles to be large
%%%%% (i) Selection (0.1 is the fraction of large particles)
NLAl=zeros(NN1,NN2,NN3);
for i=2:NN1-1;
   for j=2:NN2-1;
      for k=2:NN3-1;
         if (N(i,j,k)==2 && rand()<0.1)
            NLAl(i,j,k)=N(i,j,k);
         end
      end
   end
end
%%%%% (ii) Neighbours (1+26) of the selected particles become 2
if (LargeP==1 || LargeP==2)        % For the polydispersed  case: 1*1*1 and 3*3*3
for i=2:NN1-1;
   for j=2:NN2-1;
      for k=2:NN3-1;
         if (NLAl(i,j,k)==2)
```

```
            N(i,j,k)=2;
            N(i,j+1,k)=2;
            N(i,j-1,k)=2;
            N(i,j,k+1)=2;
            N(i,j,k-1)=2;
            N(i,j+1,k+1)=2;
            N(i,j+1,k-1)=2;
            N(i,j-1,k+1)=2;
            N(i,j-1,k-1)=2;
%
            N(i+1,j,k)=2;
            N(i+1,j+1,k)=2;
            N(i+1,j-1,k)=2;
            N(i+1,j,k+1)=2;
            N(i+1,j,k-1)=2;
            N(i+1,j+1,k+1)=2;
            N(i+1,j+1,k-1)=2;
            N(i+1,j-1,k+1)=2;
            N(i+1,j-1,k-1)=2;
%
            N(i-1,j,k)=2;
            N(i-1,j+1,k)=2;
            N(i-1,j-1,k)=2;
            N(i-1,j,k+1)=2;
            N(i-1,j,k-1)=2;
            N(i-1,j+1,k+1)=2;
            N(i-1,j+1,k-1)=2;
            N(i-1,j-1,k+1)=2;
            N(i-1,j-1,k-1)=2;
         end
      end
   end
end
end
%%%%% (iii) Neighbours (1+7) of the selected particles become 2 for a large
%%%%% cube  (2*2*2) constructed from 8 small cube.

NLAl2=zeros(NN1,NN2,NN3);
for i=2:NN1-1;
   for j=2:NN2-1;
      for k=2:NN3-1;
         if (N(i,j,k)==2 && rand()<0.1)
            NLAl2(i,j,k)=N(i,j,k);
         end
      end
   end
```

```
end
if (LargeP==2)
for i=2:NN1-1;
    for j=2:NN2-1;
        for k=2:NN3-1;
            if (NLAl2(i,j,k)==2)
                N(i,j,k)=2;
                N(i+1,j,k)=2;
                N(i,j+1,k)=2;
                N(i,j,k+1)=2;
%
                N(i+1,j,k)=2;
                N(i+1,j+1,k)=2;
                N(i+1,j,k+1)=2;
                N(i+1,j+1,k+1)=2;
            end
        end
    end
end
end

%%%%% (iii) Neighbours (1+63) of a selected particle become 2 for a large
%%%%% cube  (4*4*4) constructed from 64 small cube.

NLA3=zeros(NN1,NN2,NN3);
for i=2:NN1-1;
    for j=2:NN2-1;
        for k=2:NN3-1;
            if (N(i,j,k)==2 && rand()<0.1)
                NLA3(i,j,k)=N(i,j,k);
            end
        end
    end
end
if (LargeP==2)
for i=2:NN1-2;
    for j=2:NN2-2;
        for k=2:NN3-2;
            if (NLA3(i,j,k)==2)
                N(i,j,k)=2;
                N(i,j+1,k)=2;
                N(i,j+2,k)=2;
                N(i,j-1,k)=2;
                N(i,j,k+1)=2;
                N(i,j,k+2)=2;
                N(i,j,k-1)=2;
```

```
        N(i,j+1,k+1)=2;
        N(i,j+1,k+2)=2;
        N(i,j+1,k-1)=2;
        N(i,j+2,k-1)=2;
        N(i,j+2,k+2)=2;
        N(i,j+2,k+1)=2;
        N(i,j-1,k+1)=2;
        N(i,j-1,k+2)=2;
        N(i,j-1,k-1)=2;
%
        N(i+1,j,k)=2;
        N(i+1,j+1,k)=2;
        N(i+1,j-1,k)=2;
        N(i+1,j+2,k)=2;
        N(i+1,j,k+1)=2;
        N(i+1,j,k-1)=2;
        N(i+1,j,k+2)=2;
        N(i+1,j+1,k+1)=2;
        N(i+1,j+1,k-1)=2;
        N(i+1,j+1,k+2)=2;
        N(i+1,j-1,k+1)=2;
        N(i+1,j-1,k-1)=2;
        N(i+1,j-1,k+2)=2;
        N(i+1,j+2,k+2)=2;
        N(i+1,j+2,k+1)=2;
        N(i+1,j+2,k-1)=2;
%
        N(i-1,j,k)=2;
        N(i-1,j+1,k)=2;
        N(i-1,j-1,k)=2;
        N(i-1,j+2,k)=2;
        N(i-1,j,k+1)=2;
        N(i-1,j,k-1)=2;
        N(i-1,j,k+2)=2;
        N(i-1,j+1,k+1)=2;
        N(i-1,j+1,k-1)=2;
        N(i-1,j+1,k+2)=2;
        N(i-1,j-1,k+1)=2;
        N(i-1,j-1,k-1)=2;
        N(i-1,j-1,k+2)=2;
        N(i-1,j+2,k+1)=2;
        N(i-1,j+2,k-1)=2;
        N(i-1,j+2,k+2)=2;
%
        N(i+2,j,k)=2;
        N(i+2,j+1,k)=2;
```

```
            N(i+2,j-1,k)=2;
            N(i+2,j+2,k)=2;
            N(i+2,j,k+1)=2;
            N(i+2,j,k-1)=2;
            N(i+2,j,k+2)=2;
            N(i+2,j+1,k+1)=2;
            N(i+2,j+1,k-1)=2;
            N(i+2,j+1,k+2)=2;
            N(i+2,j-1,k+1)=2;
            N(i+2,j-1,k-1)=2;
            N(i+2,j-1,k+2)=2;
            N(i+2,j+2,k+2)=2;
            N(i+2,j+2,k+1)=2;
            N(i+2,j+2,k-1)=2;
         end
      end
   end
end
end

%%%%% For Cu flakes (this part will be considered if phiCu is non-zero)
%%%%% 0 indicates Cu cubic
C=rand(NN1,NN2,NN3);
N(C<phiCu)=0;

%%%%% (i) Selection
NLCu=ones(NN1,NN2,NN3);
for i=2:NN1-1;
   for j=2:NN2-1;
      for k=2:NN3-1;
         if (N(i,j,k)==0)
            NLCu(i,j,k)=N(i,j,k);
         end
      end
   end
end
%%%%% (ii) Defining random planes
if (phiCu~=0)
for i=2:NN1-1;
   for j=2:NN2-1;
      for k=3:NN3-2;
         if (NLCu(i,j,k)==0)
            flake=rand();
            if(flake<1/12.)                  % For the x-plane
               N(i,j,k)=0;
               N(i,j+1,k)=0;
```

```
    N(i,j-1,k)=0;
    N(i,j,k+1)=0;
    N(i,j+1,k+1)=0;
    N(i,j-1,k+1)=0;
elseif(flake>1/12. && flake<2/12.)
    N(i,j,k)=0;
    N(i,j+1,k)=0;
    N(i,j-1,k)=0;
    N(i,j,k-1)=0;
    N(i,j+1,k-1)=0;
    N(i,j-1,k-1)=0;
elseif(flake>2/12. && flake<3/12.)
    N(i,j,k)=0;
    N(i,j,k+1)=0;
    N(i,j,k-1)=0;
    N(i,j+1,k)=0;
    N(i,j+1,k+1)=0;
    N(i,j+1,k-1)=0;
elseif(flake>3/12. && flake<4/12.)
    N(i,j,k)=0;
    N(i,j,k+1)=0;
    N(i,j,k-1)=0;
    N(i,j-1,k)=0;
    N(i,j-1,k+1)=0;
    N(i,j-1,k-1)=0;
elseif(flake>4/12. && flake<5/12.) % For the y-plane
    N(i,j,k)=0;
    N(i+1,j,k)=0;
    N(i-1,j,k)=0;
    N(i,j,k+1)=0;
    N(i+1,j,k+1)=0;
    N(i-1,j,k+1)=0;
elseif(flake>5/12. && flake<6/12.)
    N(i,j,k)=0;
    N(i+1,j,k)=0;
    N(i-1,j,k)=0;
    N(i,j,k-1)=0;
    N(i+1,j,k-1)=0;
    N(i-1,j,k-1)=0;
elseif(flake>6/12. && flake<7/12.)
    N(i,j,k)=0;
    N(i,j,k+1)=0;
    N(i,j,k-1)=0;
    N(i+1,j,k)=0;
    N(i+1,j,k+1)=0;
    N(i+1,j,k-1)=0;
```

```
            elseif(flake>7/12. && flake<8/12.)
                N(i,j,k)=0;
                N(i,j,k+1)=0;
                N(i,j,k-1)=0;
                N(i-1,j,k)=0;
                N(i-1,j,k+1)=0;
                N(i-1,j,k-1)=0;
            elseif(flake>8/12. && flake<9/12.) % For the z-plane
                N(i,j,k)=0;
                N(i,j+1,k)=0;
                N(i,j-1,k)=0;
                N(i+1,j,k)=0;
                N(i+1,j+1,k)=0;
                N(i+1,j-1,k)=0;
            elseif(flake>9/12. && flake<10/12.)
                N(i,j,k)=0;
                N(i,j+1,k)=0;
                N(i,j-1,k)=0;
                N(i-1,j,k)=0;
                N(i-1,j+1,k)=0;
                N(i-1,j-1,k)=0;
            elseif(flake>10/12. && flake<11/12.)
                N(i,j,k)=0;
                N(i+1,j,k)=0;
                N(i-1,j,k)=0;
                N(i,j+1,k)=0;
                N(i+1,j+1,k)=0;
                N(i-1,j+1,k)=0;
            elseif(flake>11/12. && flake<12/12.)
                N(i,j,k)=0;
                N(i+1,j,k)=0;
                N(i-1,j,k)=0;
                N(i,j-1,k)=0;
                N(i+1,j-1,k)=0;
                N(i-1,j-1,k)=0;
            end
        end
    end
  end
end
end

%%%%% boundary condition (BC)
if (BC==1)
if phiAl>0
  N(:,:,1)=2;          % The bottom boundary
```

```
   N(:,:,NN3)=2;      % The top boundary
else
   N(:,:,1)=1;            % For phiAl=0 (all matrix)
   N(:,:,NN3)=1;
end
end

%%%%% Calculating the volume fractions
for i=1:NN1;
   for j=1:NN2;
      for k=1:NN3;   % Exclude boundaries for fixed BCs
         if (N(i,j,k)==2)
            VolFAl=VolFAl+1;
         end
         if (N(i,j,k)==0)
            VolFCu=VolFCu+1;
         end
      end
   end
end

%%%%% Uncomment the following part (between stars) to visualize the network
%%*******************************************************************
% figure
%  plot3D(double(N==2),1,'b','pasive')
%  hold on;
%  plot3D(double(N==1),1,'r','pasive')
%  plot3D(double(N==0),1,'g','pasive')
%  xlabel('N_{1}')
%  ylabel('N_{2}')
%  zlabel('N_{3}')
%  camlight right;
%  lighting phong;
%%*******************************************************************

%%%%% Finding the temperature distribution
[A B]=randomRNModel(N,km,kp);
x=A\B;
X=ndSparse(x,[NN1,NN2,NN3-2]);

%%%%% Calculating the condactance at the boundary
for i=1:NN1
   for j=1:NN2
      if N(i,j,NN3-1)==2 && N(i,j,NN3)==2
         kQ(i,j,NN3-1)=kp*rr;
      elseif N(i,j,NN3-1)==1 && N(i,j,NN3)==1
```

```
            kQ(i,j,NN3-1)=km*rr;
        elseif N(i,j,NN3-1)==2 && N(i,j,NN3)==1
            kQ(i,j,NN3-1)=kpm*rr;
        elseif N(i,j,NN3-1)==1 && N(i,j,NN3)==2
            kQ(i,j,NN3-1)=kpm*rr;
        elseif N(i,j,NN3-1)==0 && N(i,j,NN3)==2
            kQ(i,j,NN3-1)=kpc*rr;
        elseif N(i,j,NN3-1)==2 && N(i,j,NN3)==0
            kQ(i,j,NN3-1)=kpc*rr;
        elseif N(i,j,NN3-1)==0 && N(i,j,NN3)==0
            kQ(i,j,NN3-1)=kc*rr;
        elseif N(i,j,NN3-1)==0 && N(i,j,NN3)==1
            kQ(i,j,NN3-1)=kmc*rr;
        elseif N(i,j,NN3-1)==1 && N(i,j,NN3)==0
            kQ(i,j,NN3-1)=kmc*rr;
        end
    end
end

for i=1:NN1
    for j=1:NN2
        Qtot=Qtot+kQ(i,j,NN3-1)*(X(i,j,NN3-2)-0);
    end
end

end
toc                 % To estimate the simulation time
Qave=Qtot/NREAL;
KK=Qave*hTIM/(AA*(Tb-Tt))
AveVolFAl=VolFAl/(NumReal*NN1*NN2*(NN3-0))  % Including boundaries
AveVolFCu=VolFCu/(NumReal*NN1*NN2*(NN3-0)) % Including boundaries
```

## A.4 Functions for Finding Neighbors

Functions randomRNModel, FindNeighbor, and Cal_Neighbor_S, obtained from Reference (1):

```
% These functions were originally written by H. Zhang (Res. Comp. Sim. 2010, 1, 86-89).
% The changes (made by Shahla Aliakbari) are highlighted.
function [A B]=randomRNModel(N,km,kp)    %%%%% Changed k2 to km
F_top=0;
%F_bot=1; %%%%% Changed F_bot to 50
F_bot=50;

[N1 N2 N3]=size(N);
AN=N1*N2*(N3-2);
```

```
%A=zeros(AN,AN);B=zeros(AN,1); %%%%% Used spalloc, instead of zeros (see next line)
A=spalloc(AN,AN,0);B=spalloc(AN,1,0);
for I=1:AN
k=fix((I-1)/(N1*N2))+2;j=fix((I-1-(k-2)*N1*N2)/N1)+1;
i=I-(k-2)*N1*N2-(j-1)*N1;
[N_index S L] = FindNeighbor(i,j,k,N,km,kp);
%if N(i,j,k)==0
%A(I,I)=1;
%else
A(I,I)=A(I,I)+sum(S);
J=N_index(:,1)+(N_index(:,3)-2)*N1*N2+(N_index(:,2)-1)*N1;
for ii=1:6
switch L(ii)
   case 1
B(I)=B(I)+S(ii)*F_top;
case -1
B(I)=B(I)+S(ii)*F_bot;
case 0
A(I,J(ii))=A(I,J(ii))-S(ii);
end
end
end
end

function [N_index S L] = FindNeighbor(i,j,k,N,km,kp) %%%%% Changed k2 to km
[N1 N2 N3]=size(N);
S=zeros(6,1);L= zeros(6,1);
classf0 = N(i,j,k);
%%%%%%%%%%%%%%%%%%%%%%%%%%%%%%%%%%%%%%%%%%%%%%
if (k+1)==N3
L(1)=1;
else
L(1)=0;
end
if k==2
   L(2)=-1;
else
L(2)=0;
end
%%%%%%%%%%%%%%%%%%%%%%%%%%%%%%%%%%%%%%%%%%%%
N_top=[i,j,k+1];
N_bot=[i,j,k-1];
if (j+1)>N2
N_lef=[i,1,k];
else
N_lef=[i,j+1,k];
```

```
end
if j==1
N_rig=[i,N2,k];
else
N_rig=[i,j-1,k];
end
if i==N1
N_fro=[1,j,k];
else
N_fro=[i+1,j,k];
end
if i==1
N_bac=[N1,j,k];
else
N_bac=[i-1,j,k];
end
N_index=[N_top;N_bot;N_lef;N_rig;N_fro;N_bac];
%%%%%%%%%%%%%%%%%%%%%%%%%%%%%%%%%%%%%%%%%%%%%%
classf1 = N(i,j,k+1);
S(1)=Cal_Neighbor_S([classf0 classf1],km,kp,k+1,k);;
classf1 = N(i,j,k-1);
S(2)=Cal_Neighbor_S([classf0 classf1],km,kp,k-1,k);
classf1 = N(N_lef(1),N_lef(2),N_lef(3));
S(3)=Cal_Neighbor_S([classf0 classf1],km,kp,N_lef(3),k);
classf1 = N(N_rig(1),N_rig(2),N_rig(3));
S(4)=Cal_Neighbor_S([classf0 classf1],km,kp,N_rig(3),k);
classf1 = N(N_fro(1),N_fro(2),N_fro(3));
S(5)=Cal_Neighbor_S([classf0 classf1],km,kp,N_fro(3),k);
classf1 = N(N_bac(1),N_bac(2),N_bac(3));
S(6)=Cal_Neighbor_S([classf0 classf1],km,kp,N_bac(3),k);

function S=Cal_Neighbor_S(ind,km,kp,N_ind,k)
global rr
global kc

K_p=10;
%%%%% The following part (between stars) is different than the original version.
%%*************************************************
kmc=2*(kc*km)/(kc+km);
kpc=2*(kp*kc)/(kp+kc);
kpm=2*(kp*km)/(kp+km);

s00=rr*kc;
s01=rr*kmc;
s02=rr*kpc;
```

```
s22=rr*kp;
s11=rr*km;

s12=rr*kpm;
s22_0=s22;
s22_1=s22;
%%***********************************************
ind=num2str(ind);
switch lower(ind)
   case '0  0'
      S=s00;
   case '0  1'
      S=s01;
   case '0  2'
      S=s02;
   case '1  0'
      S=s01;
   case '1  1'
      S=s11;
   case '1  2'
      S=s12;
   case '2  0'
      S=s02;
   case '2  1'
      S=s12;
   case '2  2'
      if (N_ind<=K_p)&&(k<=K_p)
         S=s22_1;
      else
         S=s22_0;
      end
   otherwise
      disp('Something is wrong')
      return
end
```

# References

## Chapter 2


1. Szwarc, M.; Levy, M.; Milkovich, R. *J. Am. Chem. Soc.* **1956**, *78*, 2656-2657.
2. Mosquet, M.; Chevalier, Y.; Le Perchec, P.; Guicquero, J. P. *Macromol. Chem. Phys.* **1997,** *19*, 2457-2474.
3. Odian G. *Principles of Polymerization, 4th ed.*; Wiley: New York, 2004.
4. Mori, S.; Barth, H. G. *Size Exclusion Chromatography*; Springer: Berlin, 1999, Chapter 2.
5. Anderson, R. J.; Bendell, D. J.; Groundwater, P. W. *Nuclear Magnetic Resonance Spectroscopy*; Royal Society of Chemistry: Cambridge, UK, 2004, Chapters 2-4.
6. Friebolin, H. *Basic One- and Two-Dimensional NMR Spectroscopy*; Wiley: Weinheim, 2005, Chapter 1.
7. Beamson, G.; Briggs, D. *High resolution XPS of organic polymers*; Wiley: Chichester, 1992.
8. Van der Heide, P. *X-ray Photoelectron Spectroscopy: An introduction to Principles and Practices*; Wiley: New Jersey, 2011.
9. Van Oss, C. J.; Good, R. J.; Chaudhury, M. K. *Langmuir* **1988**, *4*, 884-891.
10. Gwinn, J. P.; Webb, R. L. *Microelectronics J.* **2003**, *34*, 215-222.
11. Chen, H.; Li, L.; Jones, P. M.; Hsia, Y. T.; Jhon, M. S. *IEEE Trans. Magnetics* **2007**, *43*, 2226-2228.
12. Xiaoa, S.; Huang, R. Y. M.; Fenga, X. *Polymer* **2007**, *48*, 5355-5368.
13. Prasher, R. *Proc. IEEE* **2006**, *94*, 1571-1586.

14. Fletcher, L. S.; Miller, R. G. *11th Aerospace Sci. Meeting, AIAA* **1973**, 73-119.

15. Fletcher, L. S. *J. Spacecraft Rockets* **1972**, *12*, 849–850.

16. Fletcher, L. S.; Cerza, M. R.; Boysen, R. L. *13th Aerospace Sci. Meeting, AIAA* **1975,** 75-187

17. Ochterbeck, J. M.; Fletcher, L. S.; Peterson, G. P. *Proc. 9th Int. Heat Transfer Conf.* **1990,** 445-450.

18. Parihar, K.; Wright, N.T. *Int. Commun. Heat Mass Transfer* **1997**, *24*, 1083-1092.

19. Mirmira, S. R.; Marotta, E. E.; Fletcher, L.S. *25th Aerospace Sci. Meeting, AIAA*, **1997**, 97-139.

20. Marotta, E. E.; Han, B. *MRS Symp. Proc. Ser.* **1998**, 515.

21. Kim, I. C.; Marotta, E. E.; Fletcher, L. S. *J. Thermophys. Heat Transfer* **2006**, *20*, 398-407.

22. Yovanovich, M. M. *Trans. Comp. Pack. Tech. IEEE* **2005**, *28*, 182-206.

23. Book of Standards: *Electrical Insulation (II)*, Volume 10.02.

24. Culham, J.R.; Teertstra, P.; Savija, I.; Yovanovich, M.M. *Int. Soc. Conf. Thermal Phenom. IEEE* **2002**, 128-135.

25. Bunyan, M. H.; de Sorgo, M. *19th IEEE SEMI-THERM Symposium* **2003**, 119-122.

26. Culham, J. R.; Teertstra, P.; Savija, I.; Yovanovich, M. M. *ITHERM Conf.* **2002**, 128-135.

27. Tzeng, J. J. W.; Weber, T. W.; Krassowski, D. W. *Sixteenth IEEE SEMI-THERM Symposium* **2000**, 174-181.

28. Bahrami, M.; Yovanovich, M. M.; Culham, J. R. *J. Thermophys. Heat Transfer* **2007**, *21*, 153-157.

29. Egerton, R. F. *Physical Principles of Electron Microscopy: An Introduction to TEM, SEM, and AEM,* Springer: New York, 2005, Chapter 5.

30. Devpura, A.; Phelan, P. E.; Prasher, R. S. *Microscale Thermophys. Eng.* **2001**, *5*, 177-189.

31. Anderson, J. L.; Quinn, J. A. *Rev. Sci. Instrum.* **1971,** *42*, 1257-1258.

32. Hassleman, D. P. H.; Johnson, L. F. *J. Composite Mater.***1987**, *21*, 508-515.

33. Davis, L. C.; Artz, B. E. *J. Appl. Phys.* **1995**, *77*, 4954-4960.

34. Nan, C. W.; Birringer, R.; Clarke, D. R.; Gleiter, H. *J. Appl. Phys.***1997**, *81*, 6692- 6699.

35. Felske, J. D. *Int. J. Heat Mass Transfer* **2004**, *47*, 3453-3461.

36. Davis, H. T.; Valencourt, L. R.; Johnson C. E. *J. Am. Ceramic Soc.* **1975**, *58*, 446-452.

37. Phelan, P. E.; Niemann, R. C. *J. Heat Transf.* **1998**, *120*, 971-976.

38. Ganapathy, D.; Singh, K.; Phelan, P. E.; Prasher, R. *J. Heat Transfer* **2005**, *127*, 553-559.

39. Sahimi, M. *Heterogeneous Materials: Linear Transport and Optical Propertie*; Springer: New York, 2003.

40. Maxwell, J. C. *A Treatise on Electricity and Magnetism, 3rd ed.*; Dover Publications: New York, 1954.

41. Bruggeman, D. A. G. *Ann. Phys.* **1935**, *24*, 636-679.

42. Wang, J. J.; Yi, X. S. *J. Appl. Polym. Sci.* **2004**, *89*, 3913-3917.

43. Nielsen, L. E. *Ind. Eng. Chem. Fundam.***1974**, *13*, 17-20.

44. Devpura, A.; Phelan, P. E.; Prasher, R. S. *Inter. Soc. Conf. Thermal Phenomena* **2000**, 21-28.

45. Yue, C.; Zhang, Y.; Hu, Z.; Liu, J.; Cheng, Z. *Microsyst. Technol.* **2010**, *16*, 633-639.

46. Karayacoubian, P. *M. Eng. Thesis*, University of Waterloo, 2006.

47. Kirkpatrick, S. *Rev. Modern Phys.* **1973**, *45*, 574-588.

## Chapter 3

1. Odian G. *Principles of Polymerization, 4th ed.*; Wiley: New York, 2004.
2. Morton, M. *Anionic Polymerization: Principles and Practice*; Academic Press: New York, 1983.
3. Jagur-Grodzinski, J. *Living and Controlled Polymerization: Synthesis, Characterization and Properties of the Respective Polymers and Copolymer*; Nova Science Publisher: New York, 2005.
4. Mosquet, M.; Chevalier, Y.; Le Perchec, P.; Guicquero, J. P. *Macromol. Chem. Phys.* **1997,** *19*, 2457-2474.
5. Otsuka, H.; Nagasaki, Y.; Kataoka, K. *Curr. Opin. Colloid Interface Sci.* **2001**, *6*, 3-10.
6. Jagur-Grodzinski, J. *React. Func. Polym.* **2001**, *49*, 1-54.
7. Quirk, R. P. *Applications of Anionic Polymerization Research.* Oxford University Press: London, 1998.
8. Powell, C. J.; Jablonski, A.; Werner, W. S. M.; Smekal, W. *Appl. Surf. Sci.* **2005**, *239*, 470-480.
9. Anderson, R. J.; Bendell, D. J.; Groundwater, P. W. *Nuclear Magnetic Resonance Spectroscopy*; Royal Society of Chemistry: Cambridge, UK, 2004, Chapter 2, 3 and 4.
10. van Oss, C. J.; Good, R. J.; Chaudhury, M. K. *Langmuir* **1988**, *4*, 884-891.
11. Sun, G. *MSc. Thesis*, University of Waterloo,1997.
12. Zalipsky, S.; Gilon, C.; Zilkha, A. *Europ. Polym. J.* **1983**, *19*, 1177-1183.

13. Smith, B. C. *Infrared Spectral Interpretation: A Systematic Approach*; Boca Raton CRC Press: London, 1999, page 136.

14. Spectral Database for Organic Compounds. *SDBS.* http://riodb01.ibase.aist.go.jp/sdbs/cgi-bin/cre_index.cgi?lang=eng.

15. Beamson, G.; Briggs, D. *High resolution XPS of organic polymers*; Wiley: Chichester, 1992.

16. NIST XPS Database. http://srdata.nist.gov/xps/selEnergyType.aspx.

17. Mosser, C. *Clays Clay Miner.* **1992**, *40 (5)*, 593-599.

18. Jolley, J. G.; Geesey, G. G.; Haukins, M. R.; Write, R. B.; Wichlacz, P. L. *Appl. Surf. Sci.* **1989**, *37*, 469-480.

19. Shard, A.G.; Whittle, J. D.; Beck, A. J.; Brookes, P. N.; Bullett, N. A.; Talib, R. A.; Mistry, A.; Barton, D.; McArthur, S. L. *J. Phys. Chem. B* **2004**, *108*, 12472-12480.

20. McGovern, W. R. *Ph.D. Thesis*, The Ohio State University, 2005.

21. Prpich, A. M. *M. Eng. Thesis*, University of Waterloo, 2007.

22. van Oss, C. J. *J. Mol. Recognit.* **2003**, *16*, 177-190.

23. Goj, L. A.; Blue, E. D.; Delp, S. A.; Gunnoe, T. B.; Cundari, T. R.; Pierpont, A. W.; Petersen, J. L.; Boyle, P. D. *Inorganic Chem*. **2006**, *45 (22)*, 9032-9045 .

24. Kapur, P; McVittie, J. P.; Saraswat, K. C. *IEEE Trans. Elect. Dev.* **2002**, *49 (4)*, 590-597.

## Chapter 4

1. Chen, H.; Li, L.; Jones, P. M.; Hsia, Y. T.; Jhon, M. S. *IEEE Transactions on Magnetics* **2007**, *43*, 2226-2228.

2. Xiaoa, S.; Huang, R. Y. M.; Fenga, X. *Polymer* **2007**, *48*, 5355-5368.

3. Incropera, F. P.; DeWitt, D. P. *Fundamentals of Heat and Mass Transfer (3rd ed.)*, Wiley: New York, 1990.

4. Savija, I.; Culham, J.R.; Yovanovich, M.M.; Marotta, E.E. *J. Thermophys. Heat Transfer* **2003**, *17* (1), 43-52.

5. Karimi, G.; Li, X.; Teertstra, P. *Electrochimica Acta* **2010**, *55*, 1619–1625.

6. Moffat, R. J. *Exp. Therm. Fluid Sci.***1988**, *1*, 3-17.

7. Savija, I.; Culham, J.R.; Yovanovich, M.M. *Proc. Inter. Elect. Pack. Tech. Conf. Exhib.* **2003**, 1-7.

8. Kasap, S. O.; Capper, P. *Springer Handbook of Electronic and Photonic Materials*, Springer: New York, **2006**.

## Chapter 5

1. Maxwell, J. C. *A Treatise on Electricity and Magnetism, 3rd ed.*; Dover Publications: New York, 1954.

2. Bruggeman, D. A. G. *Ann. Phys.* **1935**, *24*, 636-679.

3. Davis, L. C.; Artz, B. E. *J. Appl. Phys.* **1995**, *77*, 4954-4960.

4. Wang, J. J.; Yi, X. S. *J. Appl. Polym. Sci.* **2004**, *89*, 3913-3917.

5. Nielsen, L. E. *Ind. Eng. Chem. Fundam.***1974**, *13*, 17-20.

6. Devpura, A.; Phelan, P. E.; Prasher, R. S. *Inter. Soc. Conf. Thermal Phenomena* **2000**, 21-28.

7. Sahimi, M. *Heterogeneous Materials: Linear Transport and Optical Propertie*; Springer: New York, 2003.

8. Yue, C.; Zhang, Y.; Hu, Z.; Liu, J.; Cheng, Z. *Microsyst. Technol.* **2010**, *16*, 633-639.

9. Zhang, H. *Res. Comp. Sim.* **2010**, *1*, 86-89.

## Appendix

1. Zhang, H. *Res. Comp. Sim.* **2010**, *1*, 86-89.

2. Matt, J. N-dimensional sparse arrays, *MATLAB Central File Exchange* **2010**.
www.mathworks.com/matlabcentral/fileexchange/29832-n-dimensional-sparse-arrays

3. Martinez-Ortiz, C. Plot3D (from 3D voxelizer), *MATLAB Central File Exchange* **2008**.
www.mathworks.com/matlabcentral/fileexchange/21044-3d-voxelizer